Title

Improving Glioblastoma Multiforme (GBM) Radiotherapy Outcome through Personalized Biological Modeling and Optimization

Author

Yu, Victoria YuiWen

Publication Date

2017

Peer reviewed|Thesis/dissertation

UNIVERSITY OF CALIFORNIA

Los Angeles

Improving Glioblastoma Multiforme (GBM) Radiotherapy Outcome through Personalized Biological Modeling and Optimization

A dissertation submitted in partial satisfaction of the

requirements for the degree Doctor of Philosophy

in Biomedical Physics

by

Victoria YuiWen Yu

2017

ABSTRACT OF THE DISSERTATION

Improving Glioblastoma Multiforme (GBM) Radiotherapy Outcome through Personalized Biological Modeling and Optimization

by

Victoria YuiWen Yu

Doctor of Philosophy in Biomedical Physics

University of California, Los Angeles, 2017

Professor Ke Sheng, Chair

Purpose

To investigate the potential in substantially improving Glioblastoma Multiforme (GBM) radiotherapy outcome through personalized spatial dose distributions with 4π radiotherapy and temporal dose fractionation schedule optimization with patient-specific biological models.

Methods

An ordinary differential equation (ODE) model with consideration of cancer stem cell (CSC) dynamics that incorporates the distinct radiosensitivity between CSC and its non-stem counterpart, differentiated cancer cells (DCC) has been developed and shown to be

capable of reflecting the definitive treatment failure of GBM was developed. Seven patient-specific models were fitted to match the known times to GBM recurrence of these patients. Recurrence volume of each patient was transferred to generate hypothetical subvolumes with higher tumor aggressiveness on the original clinical plan to receive simultaneous integrated boost (SIB) to study the compound effect in outcome improvement arising from spatial and temporal dose optimization. For each patient, the boost dose is maximized subject to the constraints maintaining acceptable dose to surrounding OARs and coverage to the original planning target volume. With the patient-specific biological models and boost dose, a dose fractionation schedule optimization (FSO) problem with the time interval between fractions and the dose to both the non-boost and boost volumes as variables was formulated and solved with a paired simulated annealing algorithm for boost volumes with a wide range of CSC concentrations.

Results

Simultaneous integrated boost (SIB) dosage of up to 245 Gy within a 60 Gy PTV was shown to be feasible with the 4π SIB optimization formulation. Statistically significant OAR sparing was still achieved with 4π SIB compared with the originally delivered clinical plan with no boost. FSO resulted in high dose fractions in the beginning of the treatment course, followed by relatively constant dose fractions. Scenarios with lower CSC concentration within the boost volume resulted in fractionation schedules with dense once per day fractions in the beginning followed by a long time interval in the end with no treatment. With boost volume CSC concentration increased by 100 fold, maximum recurrence delay of up to 392 days was observed for a patient with the slowest growing disease.

Conclusions

By combining the spatial dose sparing power of 4π radiotherapy and temporal dose fractionation optimization with a CSC dynamics biological model in a personalized manner, significant potential in GBM disease recurrence delay was demonstrated across a cohort with differing disease characteristics. Further investigation is needed to validate the proposed model and resultant dose fractionation schedules to fully realize and translate these substantial clinical benefits.

The dissertation of Victoria YuiWen Yu is approved.

Dan Ruan

Robert Chin

Peng Hu

John Lowengrub

Ke Sheng, Committee Chair

University of California, Los Angeles

2017

To Mark, Elaine, and Mom

TABLE OF CONTENTS

List of Tables x
List of Figures xiii
List of Equations xvii
List of Appendices xix
Acknowledgements xx
Vita xxii
1 INTRODUCTION 1
1.1 Cancer Stem Cells and Radiation Dose Fractionation Schedule Optimization (FSO) 2
1.2 4π Radiotherapy 4
1.3 Advancing recurrence detection: Radiomics and machine learning 4
1.4 Overview 5
2 BIOLOGICAL MODELING AND FRACTIONATION SCHEDULE OPTIMIZATION (FSO) WITH CONSIDERATION OF CANCER STEM CELL DYNAMICS 8
2.1 Incorporation of cancer stem cell dynamics in radiation therapy treatment response modeling and the implication in GBM treatment resistance[43] 8
2.1.1 Introduction 8
2.1.2 Methods 10
2.1.3 Results 14
2.1.4 Discussion 20
2.1.5 Conclusion 24
2.2 Treating Glioblastoma Multiforme (GBM) with Super Hyperfractionated Radiation Therapy: Implication of Temporal Dose Fractionation Optimization Including Cancer Stem Cell Dynamics 25
2.2.1 Introduction 25
2.2.2 Methods 27
2.2.3 Results 36
2.2.4 Discussion 43
2.2.5 Conclusion 45
3 4Π RADIOTHERAPY 46
3.1 Prospective clinical trial on recurrent brain glioma patients 46

3.1.1 Introduction *46*
3.1.2 Methods *47*
3.1.3 Results *52*
3.1.4 Discussion *56*
3.1.5 Conclusion *58*
3.2 THE DEVELOPMENT AND VERIFICATION OF A HIGHLY ACCURATE COLLISION PREDICTION MODEL FOR AUTOMATED NON-COPLANAR PLAN DELIVERY[62] 58
3.2.1 Introduction *58*
3.2.2 Methods *60*
3.2.3 Results *68*
3.2.4 Discussion *77*
3.2.5 Conclusion *80*
3.3 SPINE STEREOTACTIC BODY RADIATION THERAPY (SBRT) WITH 4Π RADIOTHERAPY 81
3.3.1 Introduction *81*
3.3.2 Methods and Materials *82*
3.3.3 Results *86*
3.3.4 Discussion *93*
3.3.5 Conclusion *95*
4 ADVANCING GBM RECURRENCE DETECTION AND TIME PREDICTION WITH RADIOMICS 96
4.1 ADVANCING GBM RECURRENCE VOLUME DETECTION WITH LONGITUDINAL RADIOMICS CLASSIFICATION 96
4.1.1 Introduction *96*
4.1.2 Methods *97*
4.1.3 Results *104*
4.1.4 Discussion *108*
4.1.5 Conclusion *109*
4.2 PREDICTING TIME TO GLIOBLASTOMA MULTIFORME (GBM) RECURRENCE WITH MR IMAGE TEXTURE ANALYSIS 109
4.2.1 Introduction *109*
4.2.2 Methods *109*

4.2.3 Results *111*
4.2.4 Discussion and Conclusion *113*
5 PERSONALIZED 4Π RADIOTHERAPY, BIOLOGICAL MODELING, AND FRACTIONATION SCHEDULE OPTIMIZATION **114**
5.1 INTRODUCTION 114
5.2 METHODS 115
5.2.1 Patient characteristics and boost volume generation *115*
5.2.2 4π radiotherapy plan generation *116*
5.2.3 Simultaneous integrated boost (SIB) optimization formulation *117*
5.2.4 Patient-specific biological modeling *119*
5.2.5 Dose fractionation optimization with SIB *122*
5.3 RESULTS 126
5.3.1 4π radiotherapy plan generation with fixed boost dose *126*
5.3.2 Simultaneous integrated boost (SIB) optimization *126*
5.3.3 Patient-specific biological modeling and optimization *129*
5.3.4 Discussion *133*
5.3.5 Conclusion *135*
6 APPENDIX **136**
THE CHAMBOLLE-POCK ALGORITHM **136**
6.1 OPTIMIZATION PROBLEM FORMULATION 136
6.2 THE ALGORITHM 137
6.3 LINESEARCH PROCEDURE 139
7 REFERENCES **140**

LIST OF TABLES

Table 2-1: DLQ, SLQ, and USC model clonogenic survival fit parameters F is the fraction of CSCs within the tumor. (α1, β1) and (α2, β2) are the radiobiological parameters of the CSC and DCC compartment, respectively. Single LQ fit indicates the parameters obtained from a classical LQ model fit. The last three columns show the fit parameters of the USC model, D_q, D_0, and α_{USC}. 15

Table 2-2: AIC, BIC, and SSE comparison. The Akaike Information Criteria (AIC), Bayesian Information Criteria (BIC) and sum of square error (SSE) values in log10 scale for all three models on all clonogenic survival datasets. 15

Table 2-3: Number of fractions needed for each dose fractionation scheme for DLQ and SLQ. Dual-compartment result is shown in the shaded columns and the neighboring unshaded column represents the single-compartment simulation result. 17

Table 2-4: Biological effective dose (BED) to surrounding normal tissue required to achieve tumor control for DLQ and SLQ simulations. DLQ result is shown in the shaded columns and the neighboring unshaded column represents the single-compartment result. The boxes highlight the lowest possible BED value achieved in various fractionation schemes for each cell line, with DLQ and SLQ represented in solid and dashed boxes, respectively. 17

Table 2-5: ODE simulation and optimization parameters. *exception in b.i.d schedules 34

Table 2-6: Conventional fractionation optimization results 36

Table 2-7: Super hyperfractionated year-long optimization results 38

Table 2-8: Super hyperfractionated year-long optimization with dose escalation 38

Table 3-1: Patient and treatment plan characteristics. SIB = simultaneous integrated boost. EPD = Ependymoma. 48

Table 3-2: Average OAR dose statistics comparison (n = 11). *$p<0.05$ from Wilcoxon signed-rank test (a) Comparison of 4π and VMAT plans generated during the clinical trial (b) Comparison of cumulative dose of previous plan (PreRT) and trial plans. 53

Table 3-3: Summary of patient questionnaire. 56

Table 3-4: Gantry to couch and gantry to phantom measurement statistics. 70

Table 3-5: Treatment-site-specific safety buffer distance estimations with different collision probabilities 70

Table 3-6: Beam angle distribution in standard STD, extended STD, and undeliverable categories for treatments to the head, lung, abdomen, and prostate..... 74

Table 3-7: Patient and plan information..... 83

Table 3-8: Number of candidate beams for each spinal section based on collision modeling 85

Table 3-9: OAR percent dose reduction from clinical plan relative to the prescription dose of each plan. *statistically significant reduction ($p<0.05$), obtained from one-sided Wilcoxon signed rank test..... 88

Table 3-10: Average dose reduction OAR statistics of isocentric 4π plans with spinal section breakdown. *$p<0.05$, statistically significant difference between isocentric 4π and corresponding clinical plans. 90

Table 4-1: List of utilized GLCM textures. Texture definition obtained from references[55,163-165]. 99

Table 4-2: Data size of training and validation cohorts. Breakdown of recurrence and non-recurrence data size and classification results. 105

Table 5-1: Patient characteristics, original clinical plan information, and size of generated boost volume, and whether the generated SIB volume partially or completely overlaps with the original PTV volume. 116

Table 5-2: Volume definitions.....118

Table 5-3: Universal parameters for biological modeling.....121

Table 5-4: Optimization parameters 125

Table 5-5: Average OAR dose statistics for the 4π SIB with fixed boost of 110 Gy, patient-specific optimized boost, and original clinical plan. *Statistically significant dose reduction compared with clinical plan, with $p<0.05$ from one-sided Wilcoxon signed rank test. 126

Table 5-6: Case-specific optimization parameters and resultant dose statistics. PreD = prescription dose. Margin M = isotropic expansion radius around PTV_U that was used to generate volume BrnM utilized as part of the optimization constraint. All maximum dose values are defined as $D_{2\%}$. Patients with SIB only partially overlapping with the original PTV are marked with *.....127

Table 5-7: Patient-specific model and optimization parameters. N_V = number of viable tumor cells at beginning of simulation. T_{pot} = potential doubling time in days. $SIB/PTVU$ = percentage of boost volume out of the entire treated volume. BED_{SIB} = total dose

applied to boost volume. r = utilized ratio constraint between boost and non-boost volumes. 130

Table 5-8: Forward simulation with equal dose fractions and dose fractionation optimization recurrence time results across various CSC concentrations within boost volume. m = CSC concentration multiplier. TR = time to recurrence. Forward simulation results are labeled as “Equal”, optimization results are indicated by “Opt”..... 130

LIST OF FIGURES

Figure 2-1: DLQ, USC and LQ model fit comparison (a) Prostate carcinoma cell line CP3 (b) Cervial cancer cell line HeLa. (c) Breast cancer cell line MDA-MB-231. (d) GBM cell line U373MG. The DLQ, USC and LQ fit results are represented by the solid, dashed and dotted lines, respectively. 16

Figure 2-2: (a) GBM (black) and NSCLC (red) 2 Gy× 30 SLQ (dashed) and DLQ (solid) comparison. (b) GBM and NSCLC comparison between conventional 2 Gy×30 and hypofractionation 5 Gy× 10. (c) GBM CSC and DDC compartment interaction with fractionation schedules of 2 Gy×30 (black), 5 Gy×10 (red), and 10 Gy×3 (blue). CSC: dashed, DCC: solid (d) Current and previous treatment schedules for GBM. (e-f) sensitivity analysis of the stem cell conversion factor P for GBM and NSCLC cell lines. 18

Figure 2-3: Percentage of radiation-induced DCC reprogramming to CSC with respect to received dose. Determination of reprogramming coefficient c with linear regression 30

Figure 2-4: Tumor Growth ODE and radiation therapy simulation schematic 31

Figure 2-5: Schematic of optimization variables with respect to treatment time 32

Figure 2-6: Optimization result, total duration L = 364 days, number of fractions n = 53 (weekly equivalent). (a) D_U (red circles) and D_V (blue diamonds) (b) Time interval T (c) Total tumor cells vs. time. Recurrence time with this plan was predicted to be 430.5 days. 39

Figure 2-7: Optimization result, total duration L = 364 days, number of fractions n = 27 (bi-weekly equivalent). (a) D_U (red circles) and D_V (blue diamonds) (b) time interval T (c) Total tumor cells vs. time. Recurrence time with this plan was predicted to be 423.9 days. 40

Figure 2-8: Optimization result, total duration L = 360 days, number of fractions n = 13 (monthly equivalent). (a) D_U (red circles) and D_V (blue diamonds) (b) time interval T (c) Total tumor cells vs. time. Recurrence time with this plan was predicted to be 413.3 days. 41

Figure 2-9: Dose escalation (BED_{normal} = 150 Gy) optimization result, total duration L = 364 days, number of fractions n = 53 (weekly equivalent). (a) D_U (red circles) and D_V (blue diamonds) (b) time interval T (c) Total tumor cells vs. time. Recurrence time with this plan was predicted to be 452 days. 42

Figure 3-1: (a) Beam solution space with deliverable with isocentric setup with more than 5 cm clearance (blue hollow circles). Angles requiring extended source to target distance (STD) to avoid collision (black filled squares). Infeasible beams regardless of STD

extensions (red crosses). (b) Example of Selected 4π beam orientations (c) Schematic of treatment delivery workflow. (d) Intrafractional kV imaging results acquired with the TrueBeam on-board imager. 51

Figure 3-2: (a) 50% prescription isodose distribution. Distance from PTV to isodose edge in the brainstem direction: 0.29 cm (4π), 1.67 cm (VMAT) (b) DVH illustrating the sparing power of 4π. Global OAR sparing, particularly for the brainstem and chiasm, in addition to lower PTV maximum dose and increased homogeneity, can be visually observed. . 54

Figure 3-3: 4π vs. VMAT dosimetric comparison, dose relative to prescription dose of each plan. (a) Maximum dose, 4π (blue), VMAT (red). (b) Mean dose. 4π (green), VMAT (mustard) 55

Figure 3-4: 3D scanner verification with the MIMI phantom. (a) MIMI phantom (b) resultant 3D scan (c) resultant 3D scan with 6 measurements in millimeters 61

Figure 3-5: Minimum distance measurement demonstration in CAD (a) full CAD model within Autodesk Inventor with phantom on couch (b) example 5 cm closest distance measurement for treatment to the head. (c) 5 cm closest distance measurement to lung (d) closest distance measurement to prostate. 63

Figure 3-6: IEC convention and couch translations 66

Figure 3-7: Machine measurement setup. 66

Figure 3-8: Distance discrepancy histograms for gantry to couch measurements. 71

Figure 3-9: Distance discrepancy histrograms for gantry to phantom measurements 71

Figure 3-10: Automated brain treatment with room-view and patient-eye view (Multimedia View URL: http://dx.doi.org/10.1118/1.4932631.1) 72

Figure 3-11: Automated lung treatment with room view (Multimedia View URL: http://dx.doi.org/10.1118/1.4932631.2). 73

Figure 3-12: Automated prostate treatment with room view (Multimedia View URL: http://dx.doi.org/10.1118/1.4932631.3). 73

Figure 3-13: Exhaustive search model with healthy volunteer model on couch 74

Figure 3-14: Treatment-site-specific beam solution space for standard and extended STD setups. (a) head (b) left lung (c) abdomen (d) prostate 75

Figure 3-15: Gantry vs. couch angle plots for treatment to the head, lung, abdomen and prostate. The infeasible, standard STD beams are represented as red crosses and blue hollow circles, respectively. Extended STD beams are shown in black, separated into

four categories: 100 < STD ≤ 110, 110 < STD ≤ 120, 120 < STD ≤ 130 and STD > 130, represented as squares, triangles, diamonds, and plus signs. 76

Figure 3-16: Gantry vs. couch angle plots for all four spinal sections. Isocentric 4π includes only the angles deliverable with source to target distances (STD) of 100 cm (blue hollow circles). Standard 4π encompasses all beam angles that do not result in collision (blue hollow circles + black solid squares). 86

Figure 3-17: DVH comparing clinical, isocentric 4π, and standard 4π for treatment to T6 . 88

Figure 3-18: OAR dose and volume reduction box plots from the original clinical plans (a) Maximum dose reduction. Standard 4π (blue) and Isocentric 4π (red). (b) Mean dose reduction. Standard 4π (green) and Isocentric 4π (yellow) (c) Percent volume reduction in spinal cord receiving more than 50% of prescription dose ($V_{50\%}$)..... 89

Figure 3-19: Dose comparison of a case with 16 Gy delivered to T11 and 18 Gy simultaneous boost to T12. (a) Dose wash comparing dose distributions above 6 Gy between the 4 Arc VMAT clinical plan and isocentric 4π plan. (b) DVH of the clinical, isocentric 4π, and standard 4π plans..... 91

Figure 3-20: Beam orientation visualization from various spinal target locations (a) C1 (b) T11 and SIB T12 (c) L1 (d) T6..... 92

Figure 3-21: Beam angle distribution of all isocentric 4π cases, with angles colored based on PTV location..... 92

Figure 4-1: Image intensity normalization scheme. Two separate linear mappings from $(S1i, \mu i)$ to $(LIR\ , \mu s)$ and $(\mu i, S2i)$ to $(\mu s, HIR)$. 98

Figure 4-2: Inter-patient general model training workflow 103

Figure 4-3: Patient specific recurrence classification and validation workflow.....104

Figure 4-4: ROC curve of classification on the validation cohort. 105

Figure 4-5: Classified recurrence volume within search region over time for all patients. Volumes normalized relative to the volume detected at the recurrence time point. ..106

Figure 4-6: Classification results (top) from all six time points with corresponding T1 post-gadolinium contrast (center) and Flair (bottom) images, labeled with days from recurrence. White arrows indicate the region that is consistently classified as recurrence for all time points.....107

Figure 4-7: Recurrence progression of the utilized patient cohort (n = 18).....110

Figure 4-8: Mutually selected features by all except on LOO-LASSO regression. Arrow indicates region at which the average texture values are taken. 112

Figure 4-9: Commonly selected features and their individual correlation with time to recurrence. 112

Figure 4-10: Distinct set of features selected when the slowest recurring patient is left out. $R^2 = 0.539$ 113

Figure 5-1: Tumor growth ODE and radiation therapy simulation schematic with consideration of boost and non-boost volumes 122

Figure 5-2: Schematic of optimization variables with respect to treatment time 123

Figure 5-3: Simulated annealing algorithm schematic 125

Figure 5-4: SIB example dose wash (a) Case with partial overlap boost (patient 1) (b) Case with complete overlap between boost and original PTV (patient 3) 128

Figure 5-5: DVH comparison between original clinical plan and 4π SIB plans. To better demonstrate the curves for both OARs and the boost volume, two separate scales in dose were utilized for each DVH, and the scale change transition point is indicated by the black dashed line. (a) Partial boost overlap (patient 1) (b) Complete boost overlap (patient 3) 129

Figure 5-6: Dose fractionation result and corresponding tumor growth vs. time for patient 2 with CSC concentration multiplier m = 5. (a) The breakdown of CSC and DCC, along with the total viable tumor volume. (b) Resultant dose delivered to both the non-boost (blue) and SIB (red) regions at the corresponding time points. 131

Figure 5-7: Dose fractionation result and corresponding tumor growth vs. time for patient 4 with CSC concentration multiplier m = 50. (a) The breakdown of CSC and DCC, along with the total viable tumor volume. (b) Resultant dose delivered to both the non-boost (blue) and SIB (red) regions at the corresponding time points. 132

LIST OF EQUATIONS

Equation 2-1 10
Equation 2-2 11
Equation 2-3 12
Equation 2-4 13
Equation 2-5 14
Equation 2-6 28
Equation 2-7 29
Equation 2-8 29
Equation 2-9 31
Equation 2-10 33
Equation 2-11 34
Equation 3-1 64
Equation 3-2 87
Equation 4-1 99
Equation 4-2 101
Equation 4-3 101
Equation 4-4 102
Equation 4-5 102
Equation 4-6 110
Equation 5-1 117
Equation 5-2 119
Equation 5-3 120
Equation 5-4 121
Equation 5-5 123

Equation 5-6.....124
Equation 5-7.....125
Equation 6-1.....136
Equation 6-2.....137
Equation 6-3.....137
Equation 6-4.....137
Equation 6-5.....137
Equation 6-6.....138

LIST OF APPENDICES

The Chambolle-Pock Algorithm 136

ACKNOWLEDGEMENTS

I would first like to express sincere gratitude to my advisor, Dr. Ke Sheng. I truly could not have asked for a better advisor. This journey in research and discovery, along with all that I have learned and accomplished in the process, would not have been possible without his guidance, wisdom, inspiration, and countless encouragements through both good and difficult times. It has been a true honor to be trained by such a knowledgeable, passionate, creative, and compassionate person. I look forward to our continued collaboration as I continue my residency training here at UCLA.

I would also like to thank Dr. Dan Ruan, whom I first started my research with as a first year graduate student. Thank you for believing in me so much more than I did and for your continued help and support throughout my graduate career. I would also like to thank Dr. Robert Chin, Dr. John Lowengrub, and Dr. Peng Hu for the valuable insight they have provided me with as my dissertation committee.

Big thank you also to my wonderful lab mates Dan, Angelia, Kaley, Wenbo, Qihui, Ryan, and Elizabeth. The intellectual stimulation, collaboration, and most importantly, friendship and companionship that you all have provided meant so very much to me. Thanks also to Daniel, Shuiping, Ningning, for your help, friendship, and the many fun conversations during my graduate career as postdocs in the lab. You all have made my time as a graduate student a lot more enjoyable and fun.

Thank you also to Zohaib, Dan, Jenny, Da, and Tess for not only being fantastic classmates, but also friends that are always willing to hear me out and support me through

the good and bad times. I will miss the hikes, buffets, times at the karaoke and all the other fun memories with you.

Thank you also to Dr. Michael McNitt-Gray, for being a passionate, kind, and supportive program director that keeps our graduate program great. Big thank you also to Reth, for not only providing administrative help and support that made my graduate life all the better, but also for always being there as a great friend to talk to.

Without the love, support, and guidance throughout my life from my mother Meiling, none of this would have been possible. Thank you for always putting me first despite hardships and worked so hard to make sure I am happy and successful. I will also be eternally grateful to you for giving me my twin sister and best friend Elaine, with whom I can share absolutely anything.

Thank you to my stepfather Chee-Wai for inspiring and encouraging me to pursue a career Medical Physics and also for all the support during the past ten years. Thank you to my brother-in-law Malav, and my stepsisters Lillian, Linda, and Nikki for your support as well as your warm company during our family gatherings and trips that helped keep my life during graduate school diversified and enjoyable.

Finally, I would like to thank my boyfriend Mark for his unwavering support, love, and understanding for the past five years and more. Thank you for always telling me I could when I thought I couldn't. Having you by my side during this journey is truly the best thing that has happened to me. I love you so much!

VITA

EDUCATION

M.S.	University of California—Los Angeles, Biomedical Physics	2015
B.S.	Rutgers University, Physics and Statistics, Minor in Mathematics	2012

AWARDS

Moses A. Greenfield Award	2016
Norm Baily Award (AAPM Southern California Chapter)	2014
UCLA Biomedical Physics Research Colloquium, Best Poster Presentation	2014
National Science Foundation Graduate Research Fellowship	2014-2016

PEER-REVIEWED PUBLICATIONS

1. Fahimian B, **Yu V**, Horst K, Xing L, Hristov D, Trajectory modulated prone breast irradiation: a LINAC-based technique combining intensity modulated delivery with motion of the couch. Radiother Oncol, 109(3), 475-81.
2. **Yu V**, Kishan A, Cao M, Low D, Lee P, Ruan D, Dose Impact in Radiographic Lung Injury Following Lung SBRT: statistical analysis and geometric interpretation. Med Phys 41 (3) 031701, 2014
3. Dong P, **Yu V**, Nguyen D, DeMarco J, Woods K, Boucher S, Low D, Sheng K, Feasibility of Using Intermediate X-ray Energies for Highly Conformal Extracranial Radiotherapy. Med Phys 41:041709, 2014
4. **Yu V**, Fahimian B, Xing L, Hristov D, Quality control procedures for dynamic treatment delivery techniques involving couch motion. Med Phys 41 (8) 081712, 2014
5. Neylon J, Sheng K, **Yu V**, Chen Q, Low D, Kupelian P, Santhanam A, A non-voxel-based convolution/superposition algorithm optimized for scalable GPU architectures. Med Phys 41:101711, 2014
6. Kishan A, Wang PC, Sheng K, **Yu V**, Ruan D, Cao M, Tenn S, Low D, Lee P, Correlation of Clinical and Dosimetric Parameters with Radiographic Lung Injury Following Stereotactic Body Radiotherapy. Tech. Cancer Research & treatment, 1533034614551476, 2014.
7. Nguyen D, Rwigema JC, **Yu V**, Kaprealian T, Kupelian P, Selch M, Lee P, Low D, Sheng K, Feasibility of extreme dose escalation for Glioblastoma Multiforme using 4π radiotherapy. Radiation Oncology, 9(1), 239, 2014
8. **Yu VY**, Nguyen D, Kupellian P, Kaprealian T, Selch M, Low D, Pajonk F, Sheng K, Incorporating cancer stem cells in radiation therapy treatment response modeling and the implication in Glioblastoma Multiforme treatment resistance. International Journal of Radiation Oncology * Biology * Physics 91(4), 866-875, 2015.
9. Nguyen D, O'Connor D, **Yu VY**, Ruan D, Cao M, Low DA, Sheng K, Dose domain regularization of MLC leaf patterns for highly complex IMRT plans. Med Phys 42 (4), 1858-1870, 2015
10. **Yu VY**, Tran A, Nguyen D, Cao M, Ruan D, Low DA, Sheng K, The development and verification of a highly accurate collision prediction model for automated noncoplanar plan delivery. Med Phys 42 (11), 6457-6467, 2015.

11. Woods K, Nguyen D, Tran A, **Yu VY**, Cao M, Niu T, Lee P, Sheng K, Viability of Non-Coplanar VMAT for Liver SBRT as Compared to Coplanar VMAT and Beam Orientation Optimized 4π IMRT. Advances in Radiation Oncology 1(1), 67-75.
12. Tran A, Zhang J, Woods K, **Yu VY**, Nguyen D, Gustafson G, Rosen L, Sheng K, Treatment planning comparison of IMPT, VMAT and 4π radiotherapy for prostate cases. Radiation Oncology 12(1), 10, 2017.
13. Tran A, Woods K, Nguyen D, **Yu VY**, Niu T, Cao M, Lee P, Sheng K, Predicting liver SBRT eligibility and plan quality for VMAT and 4π plans. Radiation Oncology 12(1), 70, 2017

SELECTED CONFERENCE PRESENTATIONS

1. **Yu V**, Kishan A, Lee P, Low D, Ruan D, Dose Impact in Lung Fibrosis Following Lung SBRT: Statistical Analysis and Geometric Interpretation, Oral presentation at AAPM Annual Meeting, Aug. 2013
2. **Yu V**, Nguyen D, Kupellian P, Kaprealian T, Selch M, Low D, Pajonk F, Sheng K, Dual Compartment Mathematical Modeling of Glioblastoma Multiforme (GBM), AAPM Annual Meeting, Jul. 2014
3. **Yu V**, Nguyen D, Pajonk F, Sheng K, A Dual Compartment Linear-Quadratic Model of Cell Survival. ASTRO's Annual Meeting, Sep. 2014
4. **Yu V**, Nguyen D, Pajonk F, Kaprealian T, Kupelian P, Steinberg M, Low D, Sheng K, Treating Glioblastoma Multiforme (GBM) as a Chronic Disease: Implication of Temporal-Spatial Dose Fractionation Optimization Including Stem Cell Dynamics, AAPM Annual Meeting, Jul. 2015
5. **Yu V**, Nguyen D, Tran A, Ruan D, Cao M, Kaprealian T, Kupelian P, Low D, Sheng K, 4π Non-Coplanar Radiotherapy: From Mathematical Modeling to Clinical Implementation, AAPM Annual Meeting, Jul. 2015
6. **Yu V**, Nguyen D, Pajonk F, Kaprealian T, Kupelian P, Steinberg M, Low D, Sheng K, Treating Glioblastoma Multiforme as a Chronic Disease: Mathematical Dose Fractionation Schedule Optimization and Modeling with Stem Cell Dynamics, ASTRO's Annual Meeting, Oct. 2015
7. **Yu V**, Tran A, Nguyen D, Woods K, Kaprealian T, Chin R, Low D, Sheng K, Significant cord and esophagus dose reduction by 4π non-coplanar spine stereotactic body radiation therapy and stereotactic radiosurgery, ASTRO's Annual Meeting, Sept. 2016
8. **Yu V**, Landers A, Woods K, Nguyen D, Cao M, Chin R, Kaprealian T, Sheng K, A Prospective 4π Radiotherapy Clinical Trial in Recurrent Glioblastoma Multiforme (GBM) patients, AAPM Annual meeting, Jul. 2017
9. **Yu V**, O'Connor D, Nguyen D, Gu W, Ruan D, Sheng K, Predicting Time to Glioblastoma Multiforme (GBM) Recurrence with MR Texture Analysis, AAPM Annual meeting, Jul. 2017

INVITED TALKS

1. Dual-compartment mathematical modeling of cell survival after radiotherapy and its implication in GBM treatment resistance. AAPM-SCC Norm Baily Award Meeting 1st place prize, May. 2014
2. Research Opportunities with Digital Linear Accelerators: Quality Assurance for Advanced Digital Linac Implementations. AAPM Annual Meeting SAM therapy scientific symposium. Aug. 2016

1 INTRODUCTION

Glioblastoma Multiforme (GBM) is the most aggressive primary brain cancer with nearly 100% mortality. Approximately 12,000 people are newly diagnosed with the disease each year in the United States alone [1-3]. Despite the survival benefit of surgical resection followed by adjuvant chemoradiation, predominantly local recurrence within the initial high dose radiation field remains inevitable and the overall median survival is still only 15 months, with a 5-year overall survival rate of less than 10%[2,4-6]. In attempts to improve treatment outcome, numerous dose fractionation and escalation schemes were attempted with no significant benefit in overall survival or durable local control [7-20]. Re-irradiation on the recurrent disease has been shown to allow for a 6-month progression-free survival for 28-39% of patients, or up to 10-month median survival with a single fraction approach[21,22]. However, the allowable re-irradiation dosage is often greatly limited by the potential risk of radiation necrosis due to the re-treatment location being within or in close proximity of the initially irradiated tumor bed[23]. Highly conformal radiotherapy that maximally spares surrounding normal tissue and organs at risk (OAR) while maintaining or possibly escalating

planning target volume (PTV) coverage is necessary to ensure safe and effective radiation therapy on GBM recurrences. The purpose of this dissertation is to assess the potential in significantly delaying GBM disease recurrence by combining improvements in three key aspects in the management of GBM with radiation therapy, namely, the dose fractionation scheme, delivered spatial dose distribution, and recurrence detection. The background of these three aspects, along with the potential of extending patient survival when combining them, will be discussed.

1.1 Cancer Stem Cells and Radiation Dose Fractionation Schedule Optimization (FSO)

Fractionation schedule optimization (FSO), the method of systematically deriving the most effective fractionation schedule that maximizes biological effective dose (BED) to the tumor while maintaining acceptable toxicity to surrounding normal tissue, has been actively investigated. Multiple studies have demonstrated that significant increase in tumor control probability can be achieved by allowing varying dose fraction sizes throughout the treatment course[24-27]. These studies utilized mathematical models relating to the classical radiobiology that took into consideration disease site specific accelerated tumor repopulation, heterogeneous spatial and temporal oxygenation, and intra-fraction repair, which are insufficient in describing the peculiar biological properties of GBM tumors. For example, despite the extreme radioresistance demonstrated in patients, GBM cell lines do not appear to be particularly radioresistant *in vitro*. Instead, a wide range of radiosensitivies

overlapping with that of tumors curable with radiotherapy was observed [28,29]. The unexpected inconsistency between its *in vivo* and *in vitro* radio-resistance suggests that further incorporation of factors such as tumor intrinsic subpopulation heterogeneity could potentially provide further insight in this discrepancy.

One of the most prevalent tumor intrinsic heterogeneity lies in the finding of a small population of cancer stem cells (CSC) within solid tumors that hierarchically govern cancer progression[30]. The subpopulation of CSCs are observed to have characteristics of self-renewal, differentiation to non-stem progenies, and unlimited proliferative capacity[31]. In addition, experiments performed on tissue samples from multiple disease sites have suggested that CSCs are more radio-resistant than its non-stem counterpart—the differentiated cancer cells (DCC) [32-38]. Modeling studies with consideration of the dynamic interaction between CSC and DCC had been previously performed to simulate the efficacy of combining radiotherapy, differentiation therapy, vascular endothelial cell targeting [39-41], and pre-clinical optimization of radiation dosing schedules [42]. Our recently proposed ordinary differential equation (ODE) model incorporating the distinct radiosensitivity between CSC and DCC with a dual compartment linear-quadratic (DLQ) model approach, in addition to the dynamic interaction between the two compartments, was shown capable of reflecting the definitive treatment failure of GBM[43]. With a biological model that adequately reflects the radioresistance of GBM, we aim to develop a systematic temporal dose fractionation inverse optimization framework in an effort to discover dosing schemes with the potential to significantly delay GBM recurrence.

1.2 4π Radiotherapy

4π radiotherapy is an inverse optimization platform that maximally utilizes non-coplanar intensity modulated radiotherapy (IMRT) beams to significantly improve critical organ sparing [44,45]. Substantial organs-at-risk (OAR) sparing with 4π had been demonstrated for brain, head and neck, liver, lung, prostate, and spine[46-50] treatments compared with conventionally utilized volumetric arc therapy (VMAT) or intensity modulated radiation therapy (IMRT) with manually selected beams. The pattern of local disease recurrence in GBM further warrants the need for optimal delivery dose distributions due to the high likelihood of overlap between the initial irradiation and the re-irradiation locations. Feasibility of extreme dose escalation from the conventional 60 Gy to 100 Gy for GBM while maintaining normal tissue tolerance was previously demonstrated with 30 beam 4π radiotherapy plans[46]. With earlier recurrence detection or identification of more aggressive tumor subvolumes, re-irradiation or simultaneous dose boost can be performed on a smaller tumor volume, allowing for even more substantial dose escalation.

1.3 Advancing recurrence detection: Radiomics and machine learning

Radiomics, the extraction and analysis of large amounts of advanced quantitative imaging features from medical imaging, has recently garnered substantial interest as the image quality and technology in data-mining continues to improve [51-53]. Through machine learning techniques, extracted features have been combined with patient specific characteristics to create bioinformatic models for the purpose of improving the diagnostic, prognostic, and predictive accuracy of various diseases. Studies have shown the

discriminating capabilities of radiomic features for the stratification of tumor histology, tumor grades, and overall survival [54-56]. A multitude of Radiomics studies have been performed specifically for GBM. These studies emphasized on MRI-derived image features on the discovered tumor volumes, and indicated imaging predictors for stratifying anti-angiogenic treatment response[57,58], histology and tumor extent[59], and overall survival[60]. In addition, image feature analysis was shown capable of discriminating treatment induced necrosis from recurrent cancer[61]. With patient follow-up imaging performed every 2-3 months prior to recurrence as a disease-monitoring standard, we propose the extension of radiomic feature analysis onto the already available follow-up imaging could allow us to detect the disease earlier than conventional methods.

1.4 Overview

Prior to combining the potential improvements from all three methods discussed above, separate investigations performed related to all three aspects in radiotherapy management of GBM will first be discussed.

Chapter 2 describes the work related to biological modeling of GBM based on cancer stem cell dynamics, the development and discovery of a dual compartment linear quadratic model that successfully reflects the definitive treatment failure of the disease, and the use of the constructed mathematical model for the purpose of fractionation schedule optimization. The first section of Chapter 2 is a version of a manuscript titled “Incorporating cancer stem cells in radiation therapy treatment response modeling and the implication in Glioblastoma Multiform treatment resistance” published in the International Journal of Radiation Oncology Biology Physics[43]. Section 2 is the extension of the model into a FSO framework,

and is a version of a paper titled “Treating Glioblastoma Multiforme (GBM) with super hyperfractionation: Implication of temporal dose fractionation optimization including cancer stem cell dynamics” that is currently in revision.

In Chapter 3, work related to 4π radiotherapy will be discussed. First is the clinical translation of the technique with a prospective clinical trial for patients with recurrent brain glioma. This study is being prepared for submission to the International Journal of Radiation Biology Physics. The second section includes a version of a paper titled “The development and verification of a highly accurate collision prediction model for automated noncoplanar plan delivery”, published in Medical physics[62], where 4π radiotherapy was fully automated within the research modality of a linear accelerator through the development and use of a detailed and verified collision prediction computer-aided design model. The third section describes a retrospective study that assesses the dosimetric improvement on spine stereotactic body radiation therapy (SBRT) patients achievable with 4π radiotherapy. This section is also being prepared for submission to the International Journal of Radiation Biology Physics.

Chapter 4 details an experiment utilizing MRI image texture analysis and machine learning in hopes of achieving advanced tumor detection, and an additional associated preliminary study investigating the predictive power of GBM time to recurrence with MRI image texture features.

Chapter 5 combines personalized maximum achievable boost dose obtained from a novel 4π simultaneous integrated boost (SIB) optimization formulation along with a

modified dose fractionation optimization to the boost and non-boost volumes to determine the combined benefit when using all proposed methods together.

2 BIOLOGICAL MODELING AND FRACTIONATION SCHEDULE OPTIMIZATION (FSO) WITH CONSIDERATION OF CANCER STEM CELL DYNAMICS

2.1 Incorporation of cancer stem cell dynamics in radiation therapy treatment response modeling and the implication in GBM treatment resistance[43]

2.1.1 Introduction

Increasing evidence has suggested that solid tumors are hierarchically organized and contain a small population of cancer stem cells (CSC)[30,63]. The subpopulation of CSCs are observed to have characteristics of self-renewal, differentiation to non-stem progenies, and unlimited proliferative capacity[31]. In *in vitro* and animal experiments, CSC are also observed to be more radioresistant than its non-stem counterpart—the differentiated cancer cells (DCC)[32-34,64-68]. Therefore, many believe that CSCs are the driving force of cancer progression and successful therapy must eradicate CSCs. Mathematical models have suggested that perhaps the dynamic equilibrium between the DCC and CSC compartments within a tumor is essential to the treatment outcome[39,40,69,70]. A *tumor growth paradox*—CSCs driven out of

dormancy due to spontaneous DCC cell death from therapy interventions resulting in accelerated tumor progression—has been previously demonstrated with mathematical models and biological experiments[71-73].

Classical radiobiological models do not take into account such distinct radiobiology among different groups of tumor cells but instead assume uniform radiosensitivity within a tumor. The limitations of these models came to light as stereotactic ablative radiotherapy (SABR) became successful in the clinic, contrary to predictions of the Linear-Quadratic (LQ) model using conventionally established radiosensitivity parameters[74-76]. Modified LQ models that include dose dependent repair and cell killing terms, and synthesis of the LQ model with the multi-target model and a dose transition point that moderates the cell survival behavior towards higher fractional doses[74,76-79] have been developed to address this discrepancy. These models showed superior data fitting of single fractional *in vitro* cell survival for a wide range of doses compared to the unmodified LQ model. However, these models remain controversial due to their lack of biological foundations[80,81], difficulty in determining the additional fit-parameter values for individual patients and inability to provide insight to the paradoxical treatment outcomes of cancers with known high α/β ratios, such as non-small cell lung cancer (NSCLC) and glioblastoma multiforme (GBM) that respond to hypofractionation differently. Therefore these modified radiobiological models have been rarely used in practice despite the great interest of comparing treatment outcome from different regimens.

As the role of CSC in cancer progression has become more prevalent, we propose that the incorporation of its properties to radiobiological modeling might improve its performance in predicting radiotherapy treatment response. Therefore, in this study, we

performed preliminary exploration with a simplistic mathematical CSC interaction model to determine whether the tumor intrinsic heterogeneity and dynamic equilibrium between CSC and DCC can better explain radiotherapy treatment response with a dual-compartment linear quadratic (DLQ) model.

2.1.2 Methods

Two major components come into play when modeling the distinct radiosensitivity and dynamic interaction between CSC and DCC. First, the determination of the radiosensitivity parameters of both compartments. Second, an ordinary differential equation (ODE) that models the CSC self-renewal, differentiation to DCC, and DCC growth and apoptosis. These two components were then combined to model CSC and DCC interaction alongside with radiotherapy cell killing of each compartment.

2.1.2.1 Determination of radiobiological parameters

A simple way to include intra-tumor radiosensitivity heterogeneity is a dual-compartment linear quadratic model (DLQ) consisting of CSC and DCC. For a single fraction of treatment, the model was constructed as

$$SF(D) = Fe^{-\alpha_1 D-\beta_1 D^2} + (1-F)e^{-\alpha_2 D-\beta_2 D^2},$$

Equation 2-1

with F ($0 \le F \le 0.2$) as the fraction of CSC out of all cells, and α and β describing the radiobiological properties of each population. The upper bound of F was set to 0.2 due to the indication from publications that CSC is a minor subpopulation of a solid tumor[82,83]. Least square fitting of the model was then performed on 8 previously published clonogenic cell

survival datasets digitized from multiple human cancer cell lines, including U373MG (GBM), CP3, DU145 (prostate carcinoma)[84], HeLa (cervical cancer)[85], MDA-MB-231 (breast cancer)[86], H460 (NSCLC)[74], TX-4 (Osteosarcoma)[75] and Melanoma[87] using MATLAB R2013a (MathWorks, Natick, MA). All experiments were conducted using X-rays or gamma rays with relative biological effectiveness of 1. To compare the fitting performance and model quality of the DLQ model to the classical LQ model and a modified LQ (Universal Survival Curve (USC)) model[74], we calculated the sum of squares error (SSE), Akaike Information Criterion (AIC) and Bayesian Information Criterion (BIC) in log10 scale for all datasets corresponding to all three models. The USC model with three fit parameters D_0, D_q and $\alpha_{USC,}$ is shown in Equation 2-2.

$$lnSF = \begin{cases} -(\alpha_{USC}D + \beta_{USC}D^2), & D \le D_T \\ -\frac{1}{D_0}D + \frac{D_q}{D_0}, & D > D_T \end{cases}$$
$$\beta_{USC} = \frac{(1-\alpha_{USC}D_0)^2}{4D_0D_q}, \qquad D_T = \frac{2D_q}{1-\alpha D_0}$$

Equation 2-2

For the dataset of the breast cancer cell line MDA-MB-231, the CSC fraction *F* was measured to be 0.0204 in the same publication[86] and fixed in curve-fitting.

2.1.2.2 Ordinary Differential Equation (ODE) model: the interplay of CSC and DCC and Radiation Therapy

The interaction between CSC and DCC was modeled based on an ODE model developed by Hillen et. al[69] and utilized by Bachman et al[40]. The simulated tumor was assumed to be spatially homogenous, with equal cell density, growth and apoptosis throughout the tumor region. The ODE with a CSC and a DCC compartment is shown in Equation 2-3.

Self-Renewal

$$\dot{U}(t) = (2P-1)m_U K\big(W(t)\big)U(t)$$
$$\dot{V}(t) = 2(1-P)m_U K\big(W(t)\big)V(t) + m_V K\big(W(t)\big)V(t) - a_V V(t)$$

Differentiation from CSC DCC Growth Apoptosis

$$W(t) = U(t) + V(t)$$
$$K(W) = \max\{1 - W^4, 0\},$$

Equation 2-3

where $U(t)$, $V(t)$ and $W(t)$ are the volume fractions of the CSCs, DCCs, and total tumor with respect to a specified volume of interest, *P* represents the probability that a CSC gives rise to two CSCs, and 1-*P* is the probability that a CSC gives rise to two DCCs. The growth rates of CSC and DCC are m_U and m_V, respectively and a_V is the apoptosis rate of the DCCs. The apoptosis rate of CSCs was set to 0 assuming that CSC had unlimited replicative potential. $k(W)$ is a volume constraint that keeps the total tumor volume fraction within the range of 0 and 1. At time $t = 0$, the total tumor cell number was set to be 1.3×10^7 within a volume-of-interest of 4.2×10^9 cells. The initial starting fractions of the CSC and DCC compartments were then calculated based on the parameter *F* (fraction of CSC out of total tumor volume) obtained from data fitting of the DLQ model, as shown in Equation 2-1. Following Bachman et. al[88], growth and apoptosis rates (m_V, m_U, a_V) were set to $\ln(2)/T_{pot}$ day^{-1}, where T_{pot} represents the tumor potential doubling time of the simulated cancer at question. The T_{pot} values were set to be 23, 23, 4, 7.1, 8.2, 11, 1.3, and 3.9 days following published data for cell lines CP3, DU145[89], H460[90], HeLa[91], MDA-MB-231[92], Melanoma[93], TX-4[94], and U373MG[95], respectively. *P* was determined to maintain a dynamic equilibrium between CSC and DCC. In this study using the ODE formula, this requires the probability of CSC self-renewal to be slightly greater than 0.5. 0.505 was typically used in previous studies[40,69] and adopted in this study. In addition, within a reasonable range of 0.5005-0.55, we studied the sensitivity of the

conversion probability P in the conventional 2 Gy x 30 and hypofractionated 10 Gy x 5 fractionation schemes. Radiotherapy was modeled by applying the classical LQ equation using the corresponding radiobiological parameters to each compartment at times of treatment. To simplify, we assumed a spatially homogeneous yet biologically heterogeneous tumor receiving a spatially homogeneous dose.

To compare the difference between our model and the SLQ model, treatment response was simulated with the same procedure as described above, but only using the set of radiobiological parameters obtained from classical LQ fit. All ODE simulations were performed in MATLAB.

Dose fraction sizes of 2, 3, 4, 5.1, 6.5, 7.7, 9.7, and 14.3 Gy were used and the number of dose fractions required to achieve tumor control probability (TCP) of 0.9 was determined. Treatment was administered once per day, every weekday. The corresponding biological effective doses (BED) to the surrounding normal tissue were also evaluated using Equation 2-4, with n, d, and α/β representing the number of fractions, dose fraction size, and alpha beta ratio of the surrounding normal tissue, respectively. α/β was set to 3 for all BED calculations. The tumor control probability for the DLQ and SLQ models, indicated as TCP_{DLQ} and TCP_{SLQ}, were calculated based on Poisson distribution as shown in Equation 2-5, with $N_{DCC+CSC}$ and N_{CSC} representing the average number of remaining total tumor cells and remaining cancer stem cells after treatment, respectively.

$$BED = nd \times (1 + \frac{d}{\alpha/\beta})$$

Equation 2-4

$$TCP_{DLQ} = \exp(-N_{CSC})$$
$$TCP_{SLQ} = \exp(-N_{CSC+DCC})$$

Equation 2-5

Due to the representative treatment outcome from GBM and NSCLC, we compared GBM and NSCLC using parameters obtained from cell lines U373MG and H460, respectively. We selected NSCLC for comparison because hypofractionation in NSCLC has been remarkably successful[96] while the same approach has been ineffective in treating GBM[22]. Using the DLQ model, we applied currently utilized or previously applied GBM treatment schemes including, 2 Gy×30, 1.8 Gy×33, 1 Gy×78 B.I.D[7], 2 Gy×45[97], 1.3 Gy×60 B.I.D, 1.5 Gy×40 B.I.D[8,97], and 5 Gy×10 B.I.D[15] to study the tumor response to treatment.

2.1.3 Results

2.1.3.1 DLQ fit results

The radiobiological parameters obtained from DLQ, SLQ, and USC fitting results to all eight clonogenic survival datasets are shown in Table 2-1. The AIC, BIC and SSE values of all three models are shown in Table 2-2. The α values of CSC were smaller than that of their DCC counterpart for all except Tx-4, whose CSC compartment had a smaller β. As shown in Figure 2-1, the original LQ model resulted in over-prediction of cell death in the high dose range. Assessing by SSE, both DLQ and USC models more accurately described the cell survival behavior for the entire dose range than LQ with the exception of the melanoma cells. Factoring in the larger number of fitting parameters in the DLQ and USC models, the average AIC and BIC values of the DLQ and USC model were lower than that of the LQ as shown in Table 2-2. The melanoma cell was an outlier due to the extremely low α/β ratio (0.16)

resulted from the LQ fit. For MDA-MB-231, *F* was fixed based on literature. The fit-obtained β value for CSCs was close to zero, agreeing with the publication[86].

	Dual compartment fit parameters					**Single LQ fit**			**USC model fit parameters**		
	F	α1	β1	α2	β2	α	β	α/β	Dq	D0	α_{USC}
CP3	0.047	0.021	0.036	0.098	0.057	0.15	0.04	3.45	3.78	1.01	0.07
DU145	0.010	0.099	2.22E-05	0.191	0.017	0.22	0.01	17.53	2.28	2.19	0.19
HeLa	0.052	0.010	0.071	0.197	0.203	0.54	0.06	8.89	1.50	0.84	0.52
H460	0.010	0.010	0.042	0.010	0.079	0.16	0.05	2.95	4.21	0.76	0.01
MDA-MB-231	0.020	0.125	2.43E-06	0.271	0.032	0.36	0.01	32.74	1.50	1.75	0.31
Melanoma	0.166	0.038	0.059	0.013	0.061	0.01	0.06	0.16	4.39	0.89	0.01
TX-4	0.200	0.244	0.022	0.128	0.105	0.50	0.01	38.90	1.50	1.34	0.18
U373MG	0.016	0.010	1.77E-07	0.125	0.028	0.17	0.02	9.49	2.05	2.30	0.12

Table 2-1: DLQ, SLQ, and USC model clonogenic survival fit parameters F is the fraction of CSCs within the tumor. (α1, β1) and (α2, β2) are the radiobiological parameters of the CSC and DCC compartment, respectively. Single LQ fit indicates the parameters obtained from a classical LQ model fit. The last three columns show the fit parameters of the USC model, D_q, D_0, and α_{USC}.

	Akaike information criteria (AIC)			**Bayesian information criteria (BIC)**			**Sum of square error (SSE)**		
	DLQ	**LQ**	**USC**	**DLQ**	**LQ**	**USC**	**DLQ**	**LQ**	**USC**
CP3	-50.30	-40.05	-53.25	-42.10	-35.95	-47.78	0.198	0.347	0.205
DU145	-104.84	-98.37	-106.66	-96.63	-94.27	-101.19	0.030	0.046	0.033
HeLa	-34.51	-20.56	-18.25	-30.67	-18.64	-15.69	0.030	0.123	0.126
H460	-13.19	4.03	-17.80	-12.71	4.26	-17.48	0.020	0.366	0.019
MDA-MB-231	-17.38	-12.54	-13.97	-18.42	-13.17	-14.80	0.004	0.016	0.009
Melanoma	-44.22	-50.76	-44.59	-38.55	-47.92	-40.81	0.058	0.056	0.070
TX-4	-40.17	-18.33	-31.80	-35.92	-16.20	-28.97	0.027	0.174	0.062
U373MG	-92.19	-75.91	-93.94	-85.64	-72.64	-89.57	0.011	0.031	0.013
Average	-49.60	-39.06	-47.53	-45.08	-36.82	-44.54	0.047	0.145	0.067

Table 2-2: AIC, BIC, and SSE comparison. The Akaike Information Criteria (AIC), Bayesian Information Criteria (BIC) and sum of square error (SSE) values in log10 scale for all three models on all clonogenic survival datasets.

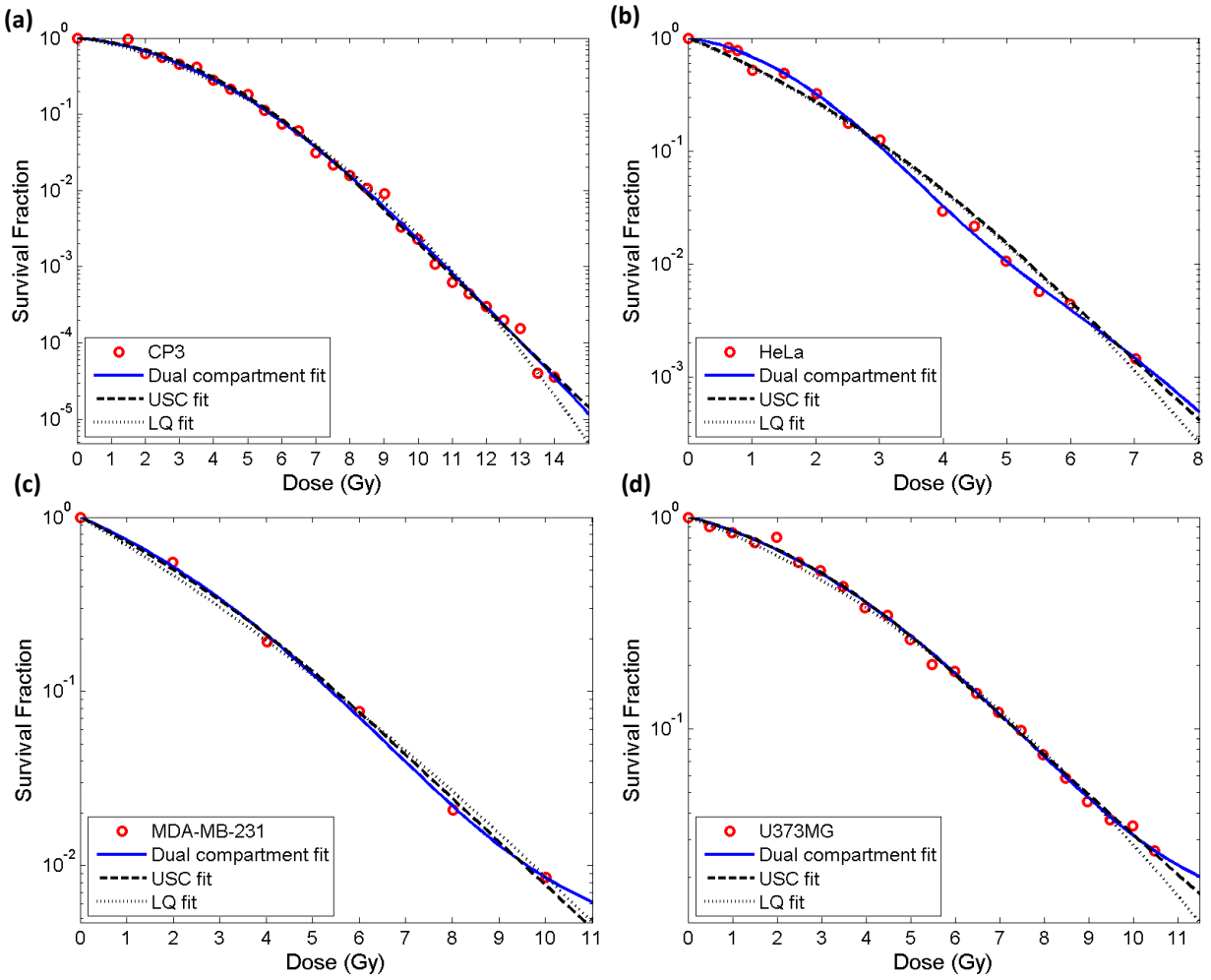

Figure 2-1: DLQ, USC and LQ model fit comparison (a) Prostate carcinoma cell line CP3 (b) Cervial cancer cell line HeLa. (c) Breast cancer cell line MDA-MB-231. (d) GBM cell line U373MG. The DLQ, USC and LQ fit results are represented by the solid, dashed and dotted lines, respectively.

2.1.3.2 ODE simulations and therapy schedule optimization

The number of dose fractions and BED required to achieve total tumor control (TCP = 1) for each dose fraction sizes and cell lines are shown in Table 2-3 and Table 2-4. As evident from Table 2-3, DLQ indicated a greater dose for tumor control than the SLQ model. However, the greater radioresistance can still be overcome with hypofractionation except for GBM cell U373MG. The GBM cells were remarkably resistant to hypofractionated treatment, requiring prohibitively high dose to control. In Table 2-4, the lowest possible BED values that achieved tumor control for each cell line were boxed. Here, the dose fraction size

that attained the lowest normal tissue BED was considered the optimal treatment fractionation schedule for each cell line. SLQ indicated conventional 2 Gy fractionation schemes to result in the least normal tissue effect while attaining tumor control for all cell lines except Melanoma, for which 7.7 Gy fraction was optimal due to its low α/β ratio. In comparison, DLQ indicated hypofractionation approaches (>7.7Gy) to be preferable for U373MG, CP3, HeLa, and H460.

	2 Gy		3 Gy		4 Gy		5.1 Gy		6.5 Gy		7.7 Gy		9.7 Gy		14.3 Gy	
CP3	85	39	41	22	24	15	16	10	10	7	7	5	5	4	3	2
DU145	71	39	48	25	36	18	28	13	22	10	19	8	15	6	10	4
HeLa	52	15	24	9	14	6	9	5	6	4	4	3	3	2	2	1
H460	75	35	35	20	20	13	13	9	8	6	6	5	4	3	2	2
MDA-MB-231	60	25	40	16	30	12	24	9	19	7	16	6	13	5	9	3
Melanoma	54	73	26	33	16	19	10	12	7	7	5	5	3	4	2	2
TX-4	30	20	19	13	13	9	10	7	7	6	6	5	4	4	3	2
U373MG	>150	45	>100	28	>75	19	>59	14	>46	10	>39	8	>31	6	>21	3

Table 2-3: Number of fractions needed for each dose fractionation scheme for DLQ and SLQ. Dual-compartment result is shown in the shaded columns and the neighboring unshaded column represents the single-compartment simulation result.

	2 Gy		3 Gy		4 Gy		5.1 Gy		6.5 Gy		7.7 Gy		9.7 Gy		14.3 Gy	
CP3	283	130	246	132	224	140	220	138	206	144	192	137	205	164	247	165
DU145	237	130	288	150	336	168	386	179	453	206	522	220	616	246	825	330
HeLa	173	50	144	54	131	56	124	69	124	82	110	82	123	82	165	82
H460	250	117	210	120	187	121	179	124	165	124	165	137	164	123	165	165
MDA-MB-231	200	83	240	96	280	112	330	124	391	144	439	165	534	205	742	247
Melanoma	180	243	156	198	149	177	138	165	144	144	137	137	123	164	165	165
TX-4	100	67	114	78	121	84	138	96	144	124	165	137	164	164	247	165
U373MG	>500	150	>600	168	>700	177	>812	193	>947	206	>1071	220	>1273	246	>1732	247

Table 2-4: Biological effective dose (BED) to surrounding normal tissue required to achieve tumor control for DLQ and SLQ simulations. DLQ result is shown in the shaded columns and the neighboring unshaded column represents the single-compartment result. The boxes highlight the lowest possible BED value achieved in various fractionation schemes for each cell line, with DLQ and SLQ represented in solid and dashed boxes, respectively.

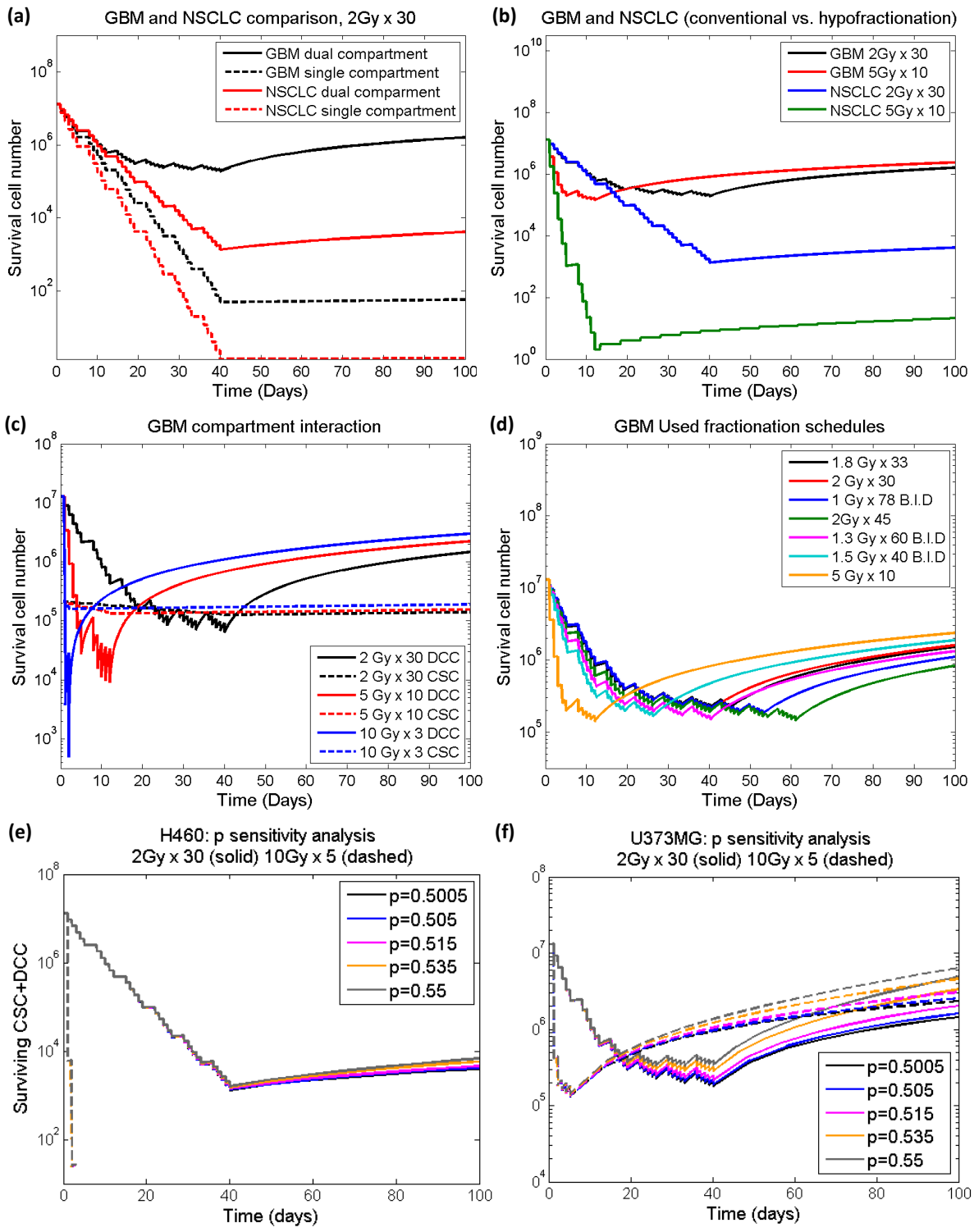

Figure 2-2: (a) GBM (black) and NSCLC (red) 2 Gy× 30 SLQ (dashed) and DLQ (solid) comparison. (b) GBM and NSCLC comparison between conventional 2 Gy×30 and hypofractionation 5 Gy× 10. (c) GBM CSC and DDC compartment interaction with fractionation schedules of 2 Gy×30 (black), 5 Gy×10 (red), and 10 Gy×3 (blue). CSC: dashed, DCC: solid (d) Current and previous treatment schedules for GBM. (e-f) sensitivity analysis of the stem cell conversion factor P for GBM and NSCLC cell lines.

Figure 2-2a demonstrates the difference between the SLQ and DLQ treatment outcome of the GBM and NSCLC cells. With a regularly fractionated treatment of 60 Gy, SLQ indicated similar outcomes between the two different cells but in DLQ, the number of remaining GBM cells was 2 orders-of-magnitude greater than remaining NSCLC cells. Figure 2-2b compares the conventional 2 Gy×30 and 5 Gy×10 SABR treatment outcome. For NSCLC, SABR resulted in significantly more effective tumor control than conventional fractionation schedules. In stark contrast, for GBM, SABR fractionating did not noticeably improve tumor control.

To understand the unique GBM radioresistance to hypofractionated treatment, we plotted the CSC and DCC compartment growth over time to explore their relationship and interactions (Figure 2-2c). The interaction between the two compartments was simulated and compared for fractionation schedules of 2 Gy×30, 5 Gy×10, and 10 Gy×3. From Figure 2-2c, the dynamic equilibrium was disrupted when the DCC population became substantially smaller than the CSC population as a result of aggressive treatment. Consequently, rapid DCC regrowth occurred to restore the equilibrium. For conventionally fractionated treatments, the equilibrium was disrupted to a lesser degree, resulting in slower re-growth that offset the disadvantage of tumor cell killing compared to the hypofractionated approaches.

The sensitivity of the DLQ model to the conversion probability P (P = 0.5005-0.55) on cell lines U373MG (GBM) and H460 (NSCLC) at the 2 Gy x 30 (solid) and 10 Gy x 5 (dashed) fractionation schemes is shown in Figure 2-2e and Figure 2-2f. The results show that increasing P leads to more rapid GBM growth but minimally impact the NSCLC cells (and other non-GBM cells that are not shown in the figure). The sensitivity study proved that a small variation in P does not affect the superior treatment outcome from hypofractionation on NSCLC and definitive treatment failure in GBM.

The results of a sample of currently used or previously tested fractionation schedules are shown in Figure 2-2d. 5 Gy×10 and 2 Gy×45 resulted in the worse and best outcome at 100 days, respectively. However, the tumor still recurred for all treatment schedules, consistent with clinical trial results.

2.1.4 Discussion

The classical LQ model has been challenged to explain response to SABR doses. In addition to its deviation from *in vitro* cell survival data, it often employs unreasonable radiobiological parameters when explaining patient treatment outcome. For example, fitting of clinical prostate treatment response to conventionally fractionated and hypofractionated treatment using LQ results in either unreasonably low α or fast repopulation time[98].

Modifications including the USC, linear-quadratic linear (LQL) and generalized LQ models have been made to moderate the LQ function towards the ablative dose range to resolve the apparent discrepancy between model prediction and measured cell survival data. However, these modifications are highly controversial because the modifications are incompatible to the underlying mechanisms of the original LQ model. These modified LQ models were further challenged by their failure to show superior modeling of the clinical data[81]. Fowler showed that these synthetic modifications can be avoided by assuming a much higher α/β value in the LQ model when fitting experimental cell survival data [99]. However, increasing α/β values would increase the difficulty to explain the success of SABR.

Instead of assuming dose dependent radiobiological parameters of a uniform cell population, we showed that when the intact LQ model is applied to tumor cell subpopulations, previously published single fraction cell survival data can be accurately

represented throughout the entire dose range. DLQ naturally leads to a more radioresistant subpopulation, which we referred as cancer stem cells, whose greater radioresistance results in their increasing weight with high dose fractions, straightening the survival curve and providing a duality in the cell biological behavior. Therefore, our model explains the cell survival curve without violating the underlying biological mechanisms of the LQ model.

A mathematical model is essential to describe the dynamic equilibrium of CSC and DCC. To achieve this goal, we adopted an integro-differential model previously utilized to test the efficacy of combination radiation and differentiation therapy[39,40]. The original model set the same α for both CSC and DCC, a β value of zero for CSC and equal number of CSC and DCC cells (F=0.5) at the beginning of treatment. These assumptions oversimplify the heterogeneous radiobiology because the CSC fraction is known to vary between tumors, and are usually a minor population within the tumor[82,83]. Our model is also different from a previous study investigating the glioma stem cell division kinetics modulated by acute and fractionated radiation treatment that assumed the same α/β for both the stem and non-stem cells[73]. We improved these models by adopting individual radiobiological parameters obtained from the DLQ fit to cell survival data. We showed that the improved DLQ model led to possible insights in tumor response to various treatment fractions.

Among the simulated dose fraction sizes, the dual-compartment model generally indicated greater radioresistance to treatment as an effort to restore cell sub-population equilibrium. We found that SLQ indicated conventional fractionation schemes to result in the least normal tissue BED while attaining tumor control, while DLQ preferred hypofractionation approaches of 7.7 or 9.9 Gy/Fx for 4 tumor sites. The only exception is the melanoma cells with an extremely low α/β ratio, which unsurprisingly prefers

hypofractionation. This study may provide an alternative angle to understand recent success of SABR, in addition to significantly improved dose conformity.

Although clinical treatment fractionations were used as reference doses in this study, due to the uncertainties in estimating the radiobiological parameters and then the significant simplification involved in using these parameters to simulate actual tumor response to treatment, DLQ in its current form may be better understood as a "surprise implication" model instead of a treatment planning model. Bear the limitation in mind, this study suggests that radioresistance can be generally overcome by using hypofractionated treatment regimens with the exception of a GBM cell line that is resistant to both conventionally fractionated *and* hypofractionated treatment. The significance of this finding not only lies in the consistence with the particularly high GBM local recurrent recurrence rates, despite aggressive treatment[97,100], it may also be used to explain the discrepancy of GBM cell *in vitro* and *in vivo* radiosensitivity[101,102]. Our model suggests that that the poor treatment outcome in GBM is perhaps driven by a CSC population that is much more radioresistant than its DCC counterpart, with $\alpha_1/\alpha_2=0.08$ and $\beta_1/\beta_2=6.26\times10^{-6}$ (β_1 on the order of 10^{-7}). This significant difference between radiosensitivities resulted in the rapid regrowth of the DCC compartment, fueled by its depletion without simultaneously eliminating the more radioresistant CSC cells, despite their small fraction at the beginning of treatment (F=0.016). CSC β values close to zero were also observed for DU145 and MDA-MB-231. However, the ratios of α for both cell lines were approximately 6 fold larger than that of U373MG. The less dramatic difference between compartmental α values enabled hypofractionation approaches to overcome the regrowth of DCC. Therefore, this model

provides a possible explanation for previously failed hypofractionated and SABR GBM treatments.

There are several limitations in this study. DLQ increases the number of fitting parameters which may increase complexity in calculating tumor BED doses. However, different from existing modified LQ models, they can be measured based on individual biopsy. For example, Lagadec et al showed that not only the CSC[86] fraction can be quantified using flow cytometry, the radiosensitivity of subpopulations can be separately measured. Therefore, our model parameters can be experimentally determined for an individual tumor or patient. DLQ can still be overly simplistic as a tumor may or may not present the CSC phenotype or there may be more than two types of cells. Environmental factors such as tumor vasculature, oxygen content in its microenvironment, and endothelial cell damage can greatly affect tumor response to radiotherapy but are not modeled by the proposed method[81]. Furthermore, tumors are modeled under a spatial homogeneous assumption. The mitotic rates of CSC and DCC and the apoptosis rate of DCC were also set to be equal, which may not realistically simulate tumor growth and cell death. Also, the statistical error of *in vitro* cell survival measurement data was not reported, preventing us from including it into data fitting. Furthermore, a shift in CSC differentiation probability and CSC cell cycle may be considered following fractionated radiation[73]. Finally, dose dependent reprogramming of DCC to CSC by radiation has recently been shown[103]. Incorporation of reprogramming may provide more insight in treatment outcome modeling[42]. However, as the first step to incorporate intra-tumor heterogeneity in radiobiological response modeling, a simple model is better to shed light on the subject at hand.

As a natural extension of the study, we will utilize the new model to optimize treatment schedules, particularly for the tumors that conventional and hypofractionated treatment failed to control.

2.1.5 Conclusion

A dual-compartment model for cell survival was studied on the basis of co-existing cancer stem cells and differentiated cancer cells. Without modifying underlying LQ cell survival behavior, the model was shown to be capable of describing the clonogenic cell survival behavior for a wide dose range. By using ODEs that simulate the dynamics of CSC and DCC differentiation and apoptosis, we found tumor response to conventionally and hypo-fractionated treatments that were consistent with clinical observations. Most remarkably, we demonstrated that the dynamic equilibrium between DCC and CSC compartments within a GBM tumor might contribute to the poor clinical outcome after radiotherapy despite its apparently low *in vitro* radioresistance.

2.2 Treating Glioblastoma Multiforme (GBM) with Super Hyperfractionated Radiation Therapy: Implication of Temporal Dose Fractionation Optimization Including Cancer Stem Cell Dynamics

2.2.1 Introduction

Glioblastoma multiforme (GBM) is a devastating primary brain cancer with abysmal survival rates. Approximately 12,000 people are newly diagnosed with GBM each year in the United States alone, accounting for more than 51% of all brain gliomas, making it the most common type of primary brain tumor [1-3]. Even with surgical resections followed by radiotherapy and chemotherapy, predominantly local recurrence occurs and the overall median survival is still only 14 months [2,4,5]. Aside from the conventionally utilized fractionation schemes of 1.8 Gy × 33 and 2 Gy × 30, numerous alterations in dose fractionation and escalation schemes were attempted in hopes to improve treatment outcome and reduce treatment duration. Accelerated hyper-fractionated twice a day (b.i.d) delivery of 1 to 1.5 Gy fractions 2 or 3 times a day[7-11], accelerated dosing of multiple 2 Gy fractions a day[12-14], hypofractionated 3 to 6 Gy[15-18] dosing schemes and aggressive dose escalation to 110 Gy using combined regularly fractionated external beam therapy and low dose rate (LDR) brachytherapy[100,104] were implemented with no significant benefit in overall survival or durable local control[20]. Greater incidence of brain necrosis was found in the hypo-fractionated and aggressive dose escalation approaches. Although the toxicity was not increased in the hyper-fractionated and accelerated -radiotherapy methods, the benefit of reducing treatment time alone did not gain sufficient support for a paradigm shift.

In the meantime, fractionation schedule optimization (FSO), the method of systematically deriving the most effective fractionation schedule that maximizes biological effective dose (BED) to the tumor while maintaining acceptable toxicity to surrounding normal tissue, has been actively investigated. With fixed time intervals of once or twice per weekday, Wein et al. demonstrated that up to two time increase in tumor control probability could be achieved by utilizing larger fractions before overnight and weekend breaks[24]. A dynamic programming framework in the presence of tumor repopulation was established to determine the optimal dose delivery schedule, which suggested a gradual increase in fraction size throughout the treatment course can improve tumor control by up to 50% [26]. Lindblom et al. studied the effectiveness of varying fractionation for non-small cell lung cancer based on the concept of heterogeneous spatial and temporal oxygenation, differing effects of accelerated repopulation, and intra-fraction repair. The study revealed that schedules with a baseline fractional dose of 2 Gy accompanied by an escalation to 3 or 4 Gy per fraction could improve the tumor control probability by up to 3 fold [25]. Kim et al. showed that the tumor equivalent uniform dose (EUD) may be increased by 17% using spatiotemporal optimization[27]. Therefore, it is interesting to test the efficacy of FSO on GBM tumors. To test FSO, the unique radiobiological properties of GBM need to be considered.

Despite the extreme radioresistance demonstrated in patients, GBM cell lines do not appear to be particularly radioresistant *in vitro*. Instead, an extremely wide range of intrinsic radiosensitivities largely overlapping with the *in vitro* survival results of tumors curative with radiation was observed[105-107]. This discrepancy suggests that the aggressive tumor behavior of GBM cannot be adequately reflected with the simple classical radiobiological models that assume a tumor cell population with uniform radiosensitivity and

radiobiological characteristics. A recently proposed ordinary differential equation (ODE) model that took into consideration the dynamic interaction and distinct radiosensitivity between cancer stem cells (CSC) and its non-stem counterpart, differentiated cancer cells (DCC), was shown capable of describing the definitive treatment failure of GBM based on human GBM cell parameters[40,43,69]. A mathematical model of PDGF-driven glioma with consideration of heterogeneous tumor subpopulations was utilized in an iterative combined theoretical and experimental strategy and identified two hyper-fractionated schedules within a five day treatment period that led to superior survival in mice[42]. These studies clearly show the potential of substantially delaying GBM recurrence without increasing normal tissue toxicity. Thus, the goal of this study is to develop a temporal dose fractionation optimization framework with consideration of CSC dynamics in an effort to discover dosing schemes with the potential to significantly delay GBM recurrence. A novel super hyperfractionated approach which was discovered through the creation of an optimization formulation will also be introduced.

2.2.2 Methods

The methodology of this study will be introduced in four major components. First, the ODE model utilized to describe the dynamic interaction between the CSC and DCC compartments. Second, the workflow of simulating radiation therapy along with ODE tumor growth. Third, the temporal dose fractionation optimization problem formulated specifically for the proposed tumor growth and radiation killing model followed by the utilized algorithm will be demonstrated. Lastly, the optimization scenarios and conditions applied,

including conventional time frames and a prolonged super hyperfractionated approach will be described.

2.2.2.1 ODE model

The ODE model used to simulate the dynamic interaction and growth of CSC and DCC is shown in the Equation 2-6 below:

$$\begin{aligned} &\text{Self-renewal} \\ &\dot{U}(t) = (2P-1)m_U k\big(W(t)\big)U(t) \\ &\dot{V}(t) = 2(1-P)m_U k\big(W(t)\big)U(t) + m_V k\big(W(t)\big)V(t) - a_V V(t) \\ &\quad\text{Differentiation from CSC} \quad\text{DCC growth} \quad\text{DCC natural cell death} \\ &W(t) = U(t) + V(t) \\ &k(W) = \max(1 - W^4, 0), \end{aligned}$$

Equation 2-6

where U(t), V(t), and $W(t)$ represent the volume fractions of CSCs, DCCs, and total tumor with respect to a specified volume of interest in which the tumor can grow. The model assumes no asymmetric divisions, where one CSC gives rise to either two CSCs or two DCCs, with probabilities of *P* and 1-*P*, respectively. The growth rates of CSC and DCC are m_U and m_V, and a_V is the natural cell death rate of DCCs. Following previous publications[40,43], all three parameters were set to $\ln(2)/T_{pot}$ day^{-1}, where T_{pot} represents the tumor potential doubling time of malignant brain tumors[95]. *k(W)* is a monotonically decreasing volume constraint function that keeps the total tumor volume fraction (*W*) within the range of 0 and 1 while simulating the slowdown in growth rate as new born cells compete for resources within the available growth volume[69]. All simulations in this study were set to have the specified volume of interest to be 10^{11} cells. The simulation was initialized with a tumor volume of 1.8×10^9 cells, corresponding to a postoperative mean T1 post-gadolinium enhancement volume of 1.8 ml from 721 patients[108]. As patients typically receive radiation

thirty days after surgery (range, 3-6 weeks)[109], the ODE was utilized to simulate 30 days of tumor growth with no treatment intervention from the specified initial conditions prior to starting radiation therapy. The ODE simulation parameters are summarized in Table 2-5.

2.2.2.2 Modeling Radiation Therapy

The distinct radiosensitivity of the CSC and DCC compartments specific to GBM were determined by performing curve fitting on clonogenic cell survival data with a dual-compartment linear quadratic (DLQ) model[43], as shown in Equation 2-7.

$$SF(D) = F \cdot \exp\{-\alpha_{CSC}D - \beta_{CSC}D^2\} + (1 - F) \cdot \exp\{-\alpha_{DCC}D - \beta_{DCC}D^2\},$$

Equation 2-7

with F as the fraction of CSC out of all tumor cells, and α_{CSC}, β_{CSC}, α_{DCC}, and β_{DCC} describing the radiobiological properties corresponding to the CSC and DCC compartments.

Furthermore, there is recent evidence suggesting that a fraction of DCC reprograms back into CSC after radiation exposure and the reprogramming rate is proportional to the dose received[103,110]. A new reprogramming term linear to dose was therefore incorporated into the model. Linear quadratic radiation therapy cell killing and reprogramming to both compartments are applied as follows in Equation 2-8:

$$U(t) = U_0 \exp\left\{-\alpha_{CSC}(D_U)_i - \beta_{CSC}(D_U)_i^2\right\} + cV_0(D_V)_i$$
$$V(t) = V_0 \exp\left\{-\alpha_{DCC}(D_V)_i - \beta_{DCC}(D_V)_i^2\right\} - cV_0(D_V)_i,$$

Equation 2-8

where U_0 and V_0 are the compartmental cell fractions after halting the ODE at dosing time points, $(\boldsymbol{D_U})_i$ and $(\boldsymbol{D_V})_i$ are the radiation delivered to CSC and DCC on the ith fraction, and c is the reprogramming coefficient. After applying the radiation therapy term shown in Equation 2-8, the ODE resumes 0.01 days (14.4 minutes) after the treatment time point.

The dose dependent reprogramming coefficient *c* was determined based on linear regression on percentage of radiation-induced CSC from purified non-stem human breast cancer specimens with respect to dose[103]. The data and corresponding linear fit is demonstrated in Figure 2-3, where both patient specimen specific and averaged patient data are shown. The fitting was performed using the average of all three patient derived data sets, indicated with red circles. The resultant slope from the linear regression was utilized as the reprogramming coefficient in simulations. A full schematic of the tumor growth and radiotherapy simulation is shown Figure 2-4.

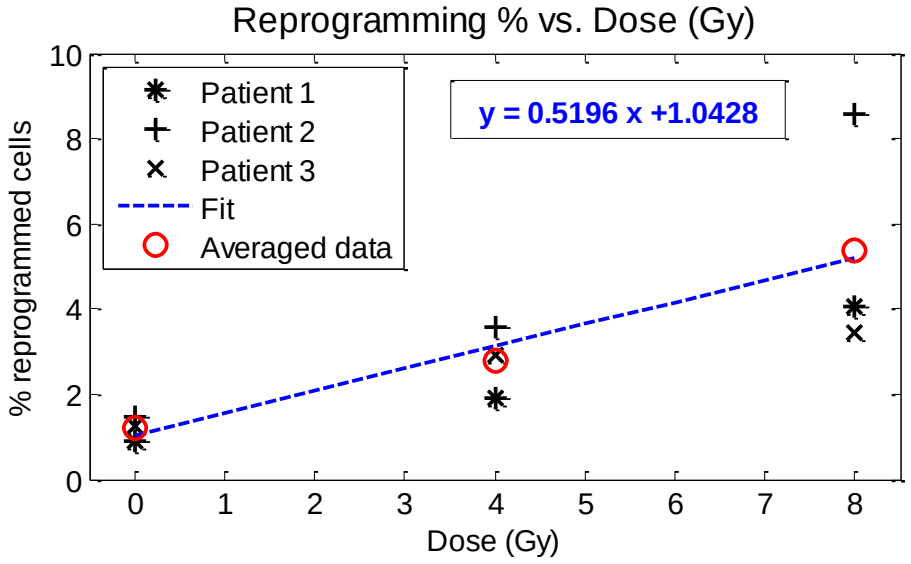

Figure 2-3: Percentage of radiation-induced DCC reprogramming to CSC with respect to received dose. Determination of reprogramming coefficient *c* with linear regression

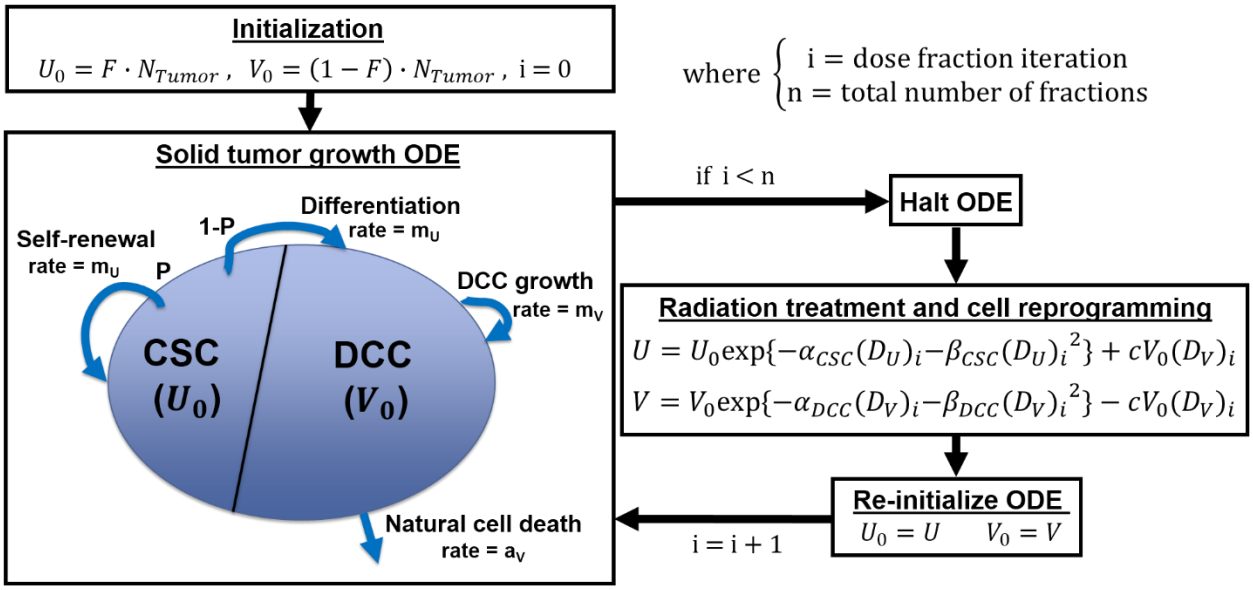

Figure 2-4: Tumor Growth ODE and radiation therapy simulation schematic

2.2.2.3 Optimization formulation and algorithm

The formulated optimization problem is shown in Equation 2-9 below:

$$\underset{D_U, D_V, T}{\operatorname{argmin}} \; W(t_{eval}|D_U, D_V, T) + \mu \frac{\sum_{t=0}^{L}(L-t)W(t|D_U, D_V, T)}{\sum_{t=0}^{L}(L-t)} + \lambda \sum_{t=0}^{L} \max(W(t|D_U, D_V, T) - R, 0)$$

$$\text{subject to} \quad \sum_{i=1}^{n} (D_U)_i + \frac{(D_U)_i^2}{\alpha/\beta} \le \text{BED}_U, \quad \sum_{i=1}^{n} (D_V)_i + \frac{(D_V)_i^2}{\alpha/\beta} \le \text{BED}_U,$$

$$D_{min} \le D_U, D_V \le D_{max}, \quad \sum_{i=1}^{n-1} T_i = L \;, L_s \le \text{T} \le L, \quad \frac{1}{r} \le \frac{(D_U)_i}{(D_V)_i} \le r \;\; for\; i = 1..n$$

Equation 2-9

The optimization variables of interest are D_U, D_V, and T. D_U and D_V are vectors of length n, with each element $(D_U)_i$ and $(D_V)_i$ representing the dose applied to the CSC and DCC compartments during the ith dose fraction. T is a vector of length n-1, with each element T_i as the time interval between fractions i and i+1.The total treatment duration is specified as L. A schematic of the optimization variables with respect to treatment time is shown in Figure 2-5.

The objective function is formulated in three terms. The first and main objective term, $W(t_{eval}|D_U, D_V, T, X)$, indicates the total tumor fraction U+V at the evaluation time point day t_{eval} given D_U, D_V, and T. Minimization of total cell number at a later time point delays disease recurrence. To reduce tumor burden during the treatment period, the second objective term that introduces time-weighted penalty on the total tumor fraction at each time point t, $W(t|D_U, D_V, T)$, with t spanning from the beginning to end of specified treatment duration, was incorporated. The weighting of each evaluation time t is based on the corresponding remaining treatment duration to simulate the accumulation of tumor burden over time. The third term applies strong penalty when the total cell fraction W exceeds the defined disease recurrence total cell fraction R. μ and λ are weighting coefficients for the second and third objective terms.

Optimization constraints include total normal tissue biological effective dose (BED_{normal}) to both compartments (BED_U and BED_V), fractional dose limits (D_{min} and D_{max}), time interval limits, and ratio constraint (r) between dose delivered to CSC and DCC to ensure plan deliverability. L_s indicates the lower bound of the time intervals, which was set to 1 to ensure at least one full day between all fractions. α/β represents the ratio between the linear and quadratic terms within the classic LQ model for surrounding normal brain tissue, which was set to 3 for all calculations.

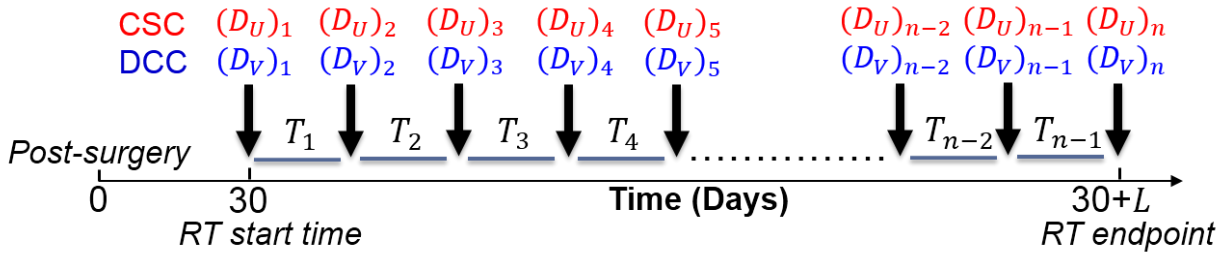

Figure 2-5: Schematic of optimization variables with respect to treatment time

The optimization problem was solved using a paired simulated annealing algorithm[111], in which a pair of elements within decided variable for change (T, D_U, or D_V) were changed in each iteration to maintain problem constraints. The problem was initialized at equal dose and time intervals for all fractions. For each iteration, a random number between 0 and 1 was generated as decision to vary either the time variable T or dose variables D_U and D_V. The decision probability given to changing T, D_U, D_V were 0.5, 0.25, and 0.25, respectively. A pair of elements in the decided variable were randomly selected to be varied, with both changes stepping in opposite directions to maintain equal total time or BED. To ensure that the optimized delivery times are feasible, the time intervals in T were maintained as integers by rounding the generated time step in each iteration. The change applied to the selected elements was sampled from a Gaussian distribution, with standard deviations specific to dose (σ_D) or time (σ_T) presented in Equation 2-10 below:

$$\sigma_D = \frac{s_D - 1}{(N_D + 1)^{1/T_{step}}} \qquad \sigma_T = 1 + \frac{s_T - 1}{(N_T + 1)^{1/T_{step}}},$$

Equation 2-10

where s_D and s_T are the step sizes at the beginning of the optimization, N_D and N_T are the number of times that a change in the dose and time were accepted. To account for the rounding procedure performed for time changes, σ_T was kept above 1 to ensure sufficient variation in T. T_{step} controls the decreasing rate of σ_D and σ_T as the number of acceptances increase. For dose changes, ratio constraints were applied by calculating the upper and lower bound specific to the opposite dose compartment corresponding to the same fractions. Cutoffs were applied to the generated changes if the resultant new value did not satisfy problem constraints. The objective function was evaluated after each iteration, and the change was accepted unconditionally if the objective function value decreased. If objective

function value was not reduced, the change was accepted with conditional probabilities of P_D and P_T shown in Equation 2-11.

$$P_D = \frac{1}{(N_D+1)^{1/T_{prob}}} \qquad P_T = \frac{1}{(N_T+1)^{1/T_{prob}}},$$

Equation 2-11

where N_D and N_T were updated each time a dose or time change was accepted due to improvement in the objective function or the passing of conditional probabilities P_D and P_T. 10000 total iterations were performed and the set of variables resulting in the best result was taken as the final optimization result. Outcome was assessed by the recurrence time point, the time at which the total cell number grows to 2.8×10^9 cells, corresponding to radiographically noticeable volume increase of 1 ml in total tumor volume from the initialized postoperative volume. All optimization parameters are shown in Table 1. All calculations were performed in MATLAB 2013a (MathWorks, Natick, MA).

ODE parameters				Radiation therapy parameters					
N_{Tumor}	m_U	m_V	α_V	F	α_{CSC}	β_{CSC}	α_{DCC}	β_{DCC}	c
1.80E-02	0.1777	0.1777	0.1777	0.016	0.01	1.77E-07	0.125	0.028	5.196E-03
Universal optimization parameters									
μ	λ	R	s_D	s_T	T_{prob}	T_{step}	L_s	D_{max}	D_{min}	r
10	10000	2.8E-02	40	15	1	2	1	15	1*	2

Table 2-5: ODE simulation and optimization parameters. *exception in b.i.d schedules

2.2.2.4 Optimization scenarios

2.2.2.4.1 Optimization within conventional time frame

Optimization was performed within the equivalent duration, number of fractions, and BED_{normal} of a subset of currently utilized or previously applied GBM treatment fractionation schemes, including 2 Gy × 30, 1.8 Gy × 33, twice a day (b.i.d.) schedules of 1 Gy × 72[7], 1.5 Gy × 40[8], and hypo-fractionated approach of 5 Gy × 10[15] to assess the potential in

delaying recurrence with temporal dose optimization. For b.i.d fractionation schemes, the time increments were set in units of half days and D_{min} was lowered to 0.5 Gy. The objective function evaluation time point (t_{eval}) was set to 300 days. The recurrence time resulting from optimization was compared with the recurrence time of the original dose fractionations predicted by the model.

2.2.2.4.2 Super hyperfractionated regular schedules

Varying dose fractionation within the conventional treatment time frames has been shown to modestly impact the outcome of GBM radiotherapy. The potential in further delaying recurrence time with a super hyperfractionated treatment approach was therefore tested. Specifically, the potential in improving outcome with the novel approach of treating GBM with a protracted schedule was explored with a total treatment course of up to one year. Simulated annealing optimization on dose was performed with fixed time points of weekly, bi-weekly, and monthly, with total BED_{normal} of 100 Gy (equivalent to that of 2 Gy × 30, assuming $\alpha/\beta = 3$). The objective function evaluation time point (t_{eval}) was set to 500 days. The optimized recurrence results were compared with that of equal dose throughout all fractions for all time schedules.

2.2.2.4.3 Super hyperfractionated temporal dose optimization

Full optimization with both time and dose as variables was performed with number of fractions equivalent to weekly, biweekly, and monthly over one year. The objective function evaluation time point (t_{eval}) was set to 500 days. The resultant recurrence times were also compared with corresponding regular time schedules with equal dose over time. To assess the synergy of dose escalation and hyperfractionation, the outcome with dose

escalation to BED_{normal} of 150 Gy (equivalent to 2 Gy × 45, assuming $\alpha/\beta = 3$) was also generated.

2.2.3 Results

2.2.3.1 Optimization within conventional time frame

The resultant recurrence time from optimizing within conventional time frames is shown in Table 2-6. The recurrence time point of the conventional 2 Gy × 30 delivery predicted by the model is 250.3 days, in close agreement with the observed average recurrence time of 7-9 months[109,112]. Variation in time and dose did not significantly improve the recurrence time for all attempted historically and currently administered fractionation schemes. The improvement in overall recurrence time is slightly greater for 1 Gy × 72, which has the longest treatment duration, indicating that an extension in the treatment duration might help improve the result.

Equivalent Fractionation scheme	Total duration L (days)	$BED_{U,V}$ (Gy)	Original recurrence (days)	Optimized recurrence (days)
2 Gy × 30	39	100	250.3	254.7
1.8 Gy × 33	44	95.04	247.6	251.3
1 Gy × 72 B.I.D.	49.5	96	258.2	269.1
1.5 Gy × 40 B.I.D.	25.5	90	249.4	255.5
5 Gy × 10	11	133.33	234.4	234.5

Table 2-6: Conventional fractionation optimization results

2.2.3.2 Super hyperfractionated year-long regular and variable schedules

Outcome from optimizing super hyperfractionated schedules equivalent to year-long weekly, bi-weekly, and monthly treatment with fixed and variable times are shown in Table 2-7. Within Table 2-7, the column labeled “Constant” indicates equal dose and time interval throughout the year, “fixed time” results from holding constant time intervals while

optimizing doses, and "variable time" shows outcome with doses and time intervals all as optimization variables. With BED_{normal} equivalent to that of the conventional 2 Gy × 30 treatment, which had recurrence time of 250.3 days, all three super hyperfractionated year-long regular schedules with equal dose ("Constant") significantly delayed recurrence by more than 70 days. Optimization of time intervals in conjunction with doses further postponed recurrence by more than 2 months from the regular fixed dose schedules. The weekly equivalent plan with 53 fractions, as shown in Figure 2-6, achieved the largest benefit of 180 days compared with conventional therapy using 2Gy × 30. The time interval result (Figure 2-6b) indicates relatively infrequent treatments in the beginning, followed by aggressive once per day delivery in the middle of the treatment course, where the tumor size is significantly reduced. With an appreciably smaller tumor, the treatment again becomes infrequent, until the tumor size approaches the recurrence level, where an increase in treatment frequency is observed. The rate of treatment continues to increase up to the end of the treatment course in order to complete the treatment with the lowest possible tumor size while keeping total tumor size under the defined recurrence level. In terms of dose, D_U was relatively constant throughout time, while D_V was held at minimum dose of 1 Gy for most fractions and peaking at the fractions immediately following larger time intervals (Figure 2-6a). The dose and time results of the bi-weekly (n = 27) and monthly (n = 13) equivalent plans are shown in Figure 2-7 and Figure 2-8, respectively.

The trend in outcome of less aggressive fractionation in the beginning of treatment, preceded by dense fractions in the middle of the treatment course, followed by a decrease in frequency, and then a final increase in treatment aggressiveness was also observed. Dose

optimization alone achieved substantial benefit as well but less than variable time as expected, as demonstrated in the column labeled "fixed time" in Table 2-7.

	Equivalent Fractionation scheme	**Total duration L (days)**	$\boldsymbol{BED_{U,V}}$ (Gy)	**Recurrence time (days)**		
				Constant	Fixed time	Variable time
Weekly	1.3125 Gy × 53	364	100	372.4	401.2	430.5
Bi-weekly	2.1553 Gy × 27	364	100	351.1	403.7	423.9
Monthly	3.5325 Gy × 13	360	100	322.2	411.8	413.3

Table 2-7: Super hyperfractionated year-long optimization results

	Equivalent Fractionation scheme	**Total duration L (days)**	$\boldsymbol{BED_{U,V}}$ (Gy)	**Recurrence time (days)**		
				Constant	Fixed time	Variable time
Weekly	1.7773 Gy × 53	364	150	407.6	413.6	452.0
Bi-weekly	2.8493 Gy × 27	364	150	406.1	412.7	441.3
Monthly	4.5716 Gy × 13	360	150	325.7	410.2	424.5

Table 2-8: Super hyperfractionated year-long optimization with dose escalation

The result from escalating BED_{normal} to 150 Gy is shown in Table 2-8. Maximum recurrence time was also observed for the weekly equivalent plan at 452 days, which provides a 201 days delay in recurrence compared with conventional delivery. The resultant plan from the weekly equivalent optimization with dose escalation is shown in Figure 2-9. In terms of time intervals, trends similar to the results without dose escalation was observed. However, oscillations between one and two Gy was shown for D_V, unlike the stable one Gy dose fractions shown in Figure 2-6a. For the bi-weekly and monthly optimizations, dose escalation did not alter the general trend of the result.

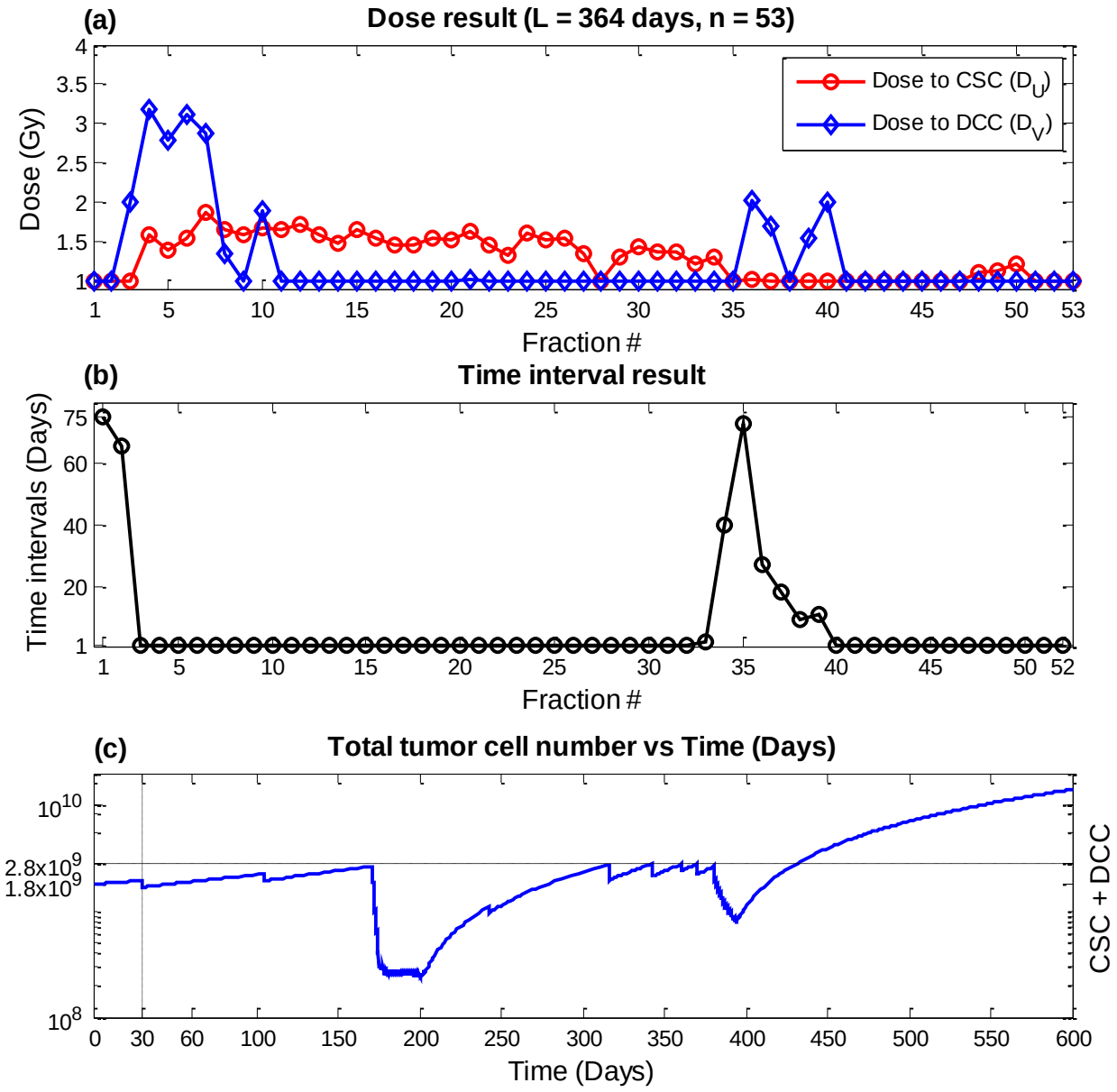

Figure 2-6: Optimization result, total duration L = 364 days, number of fractions n = 53 (weekly equivalent). (a) $\boldsymbol{D_U}$ (red circles) and $\boldsymbol{D_V}$ (blue diamonds) (b) Time interval $\boldsymbol{T}$ (c) Total tumor cells vs. time. Recurrence time with this plan was predicted to be 430.5 days.

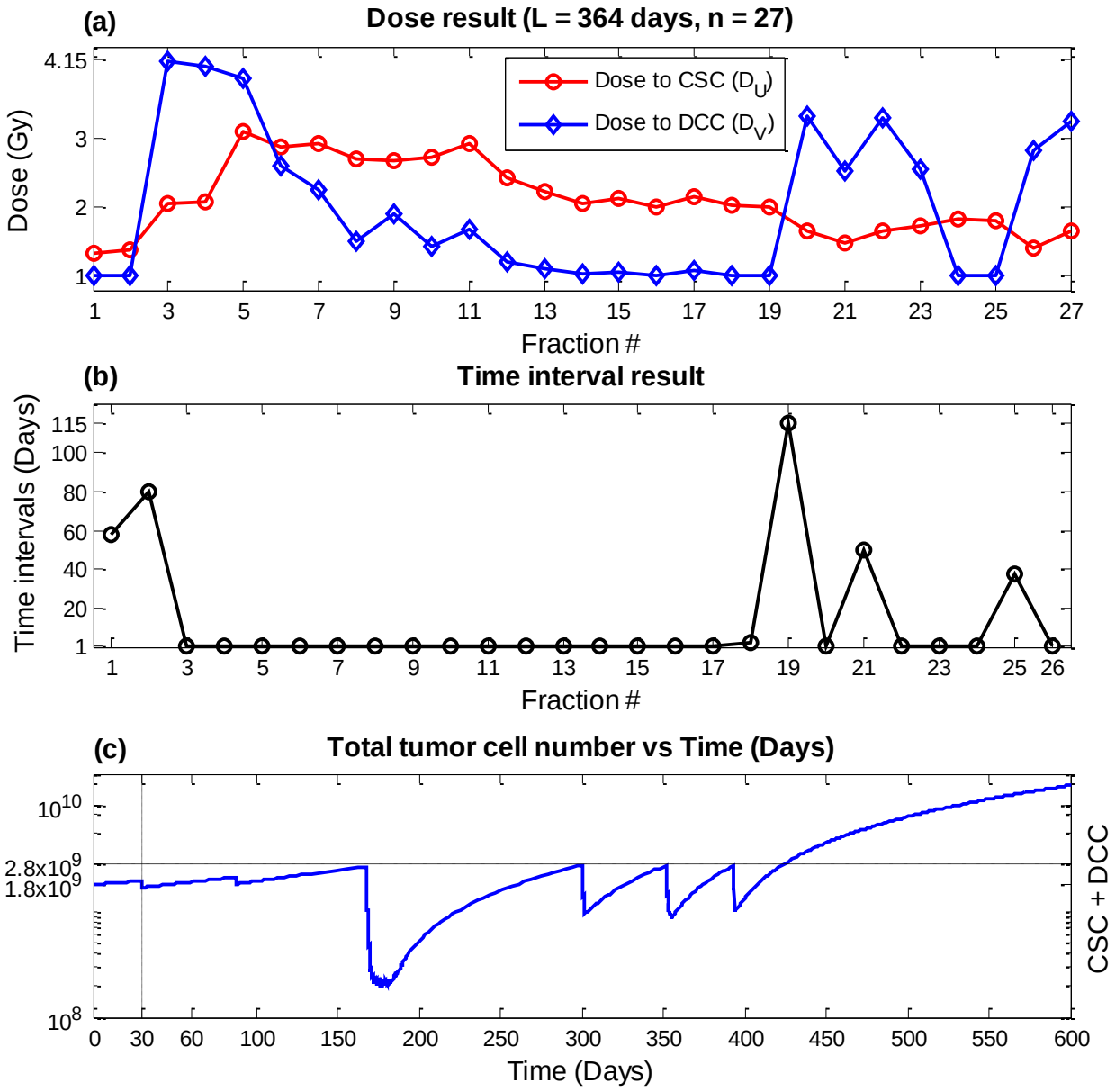

Figure 2-7: Optimization result, total duration $\boldsymbol{L}$ = 364 days, number of fractions $\boldsymbol{n}$ = 27 (bi-weekly equivalent). (a) $\boldsymbol{D_U}$ (red circles) and $\boldsymbol{D_V}$ (blue diamonds) (b) time interval $\boldsymbol{T}$ (c) Total tumor cells vs. time. Recurrence time with this plan was predicted to be 423.9 days.

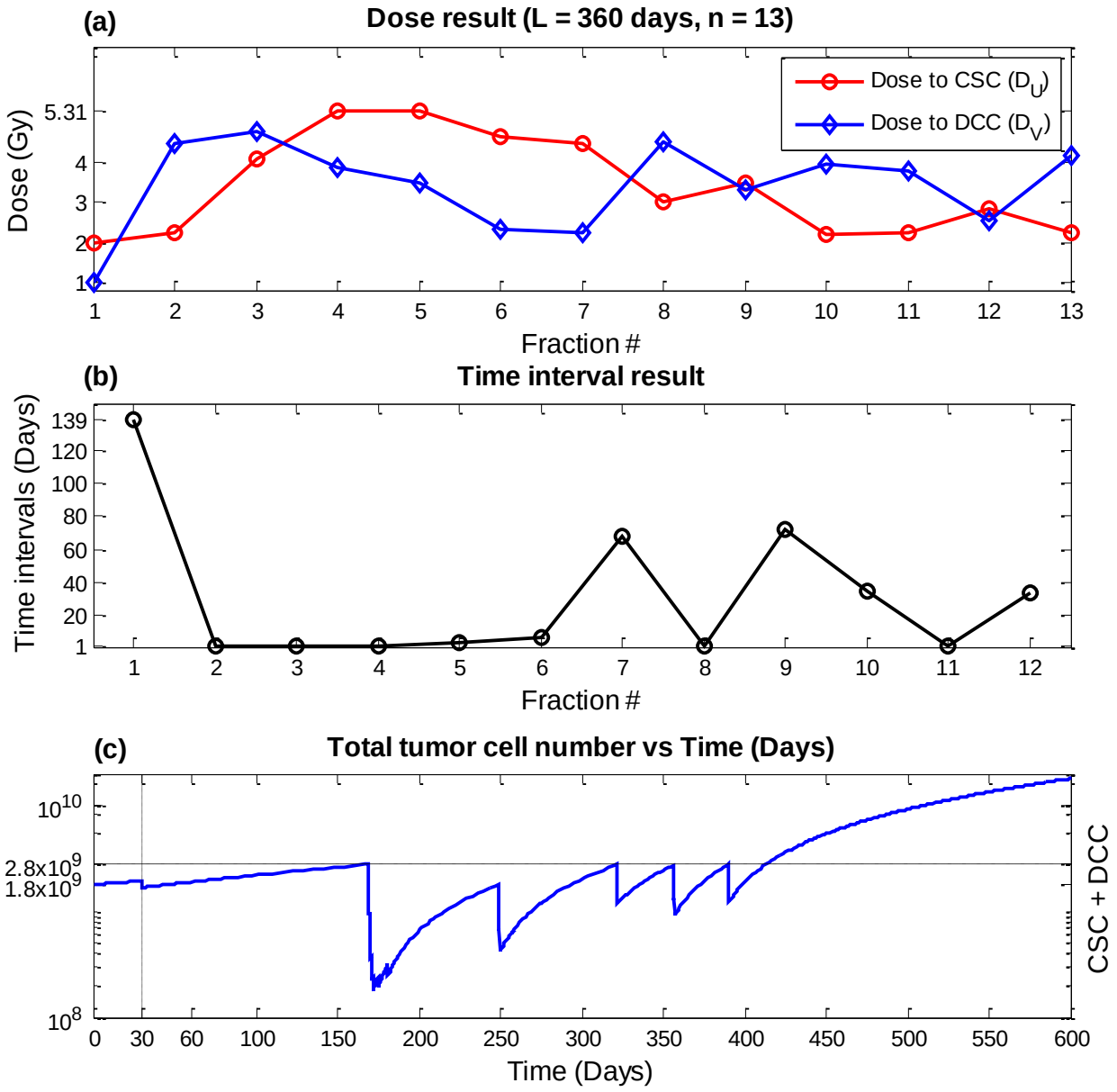

Figure 2-8: Optimization result, total duration $\boldsymbol{L}$ = 360 days, number of fractions $\boldsymbol{n}$ = 13 (monthly equivalent). (a) $\boldsymbol{D_U}$ (red circles) and $\boldsymbol{D_V}$ (blue diamonds) (b) time interval $\boldsymbol{T}$ (c) Total tumor cells vs. time. Recurrence time with this plan was predicted to be 413.3 days.

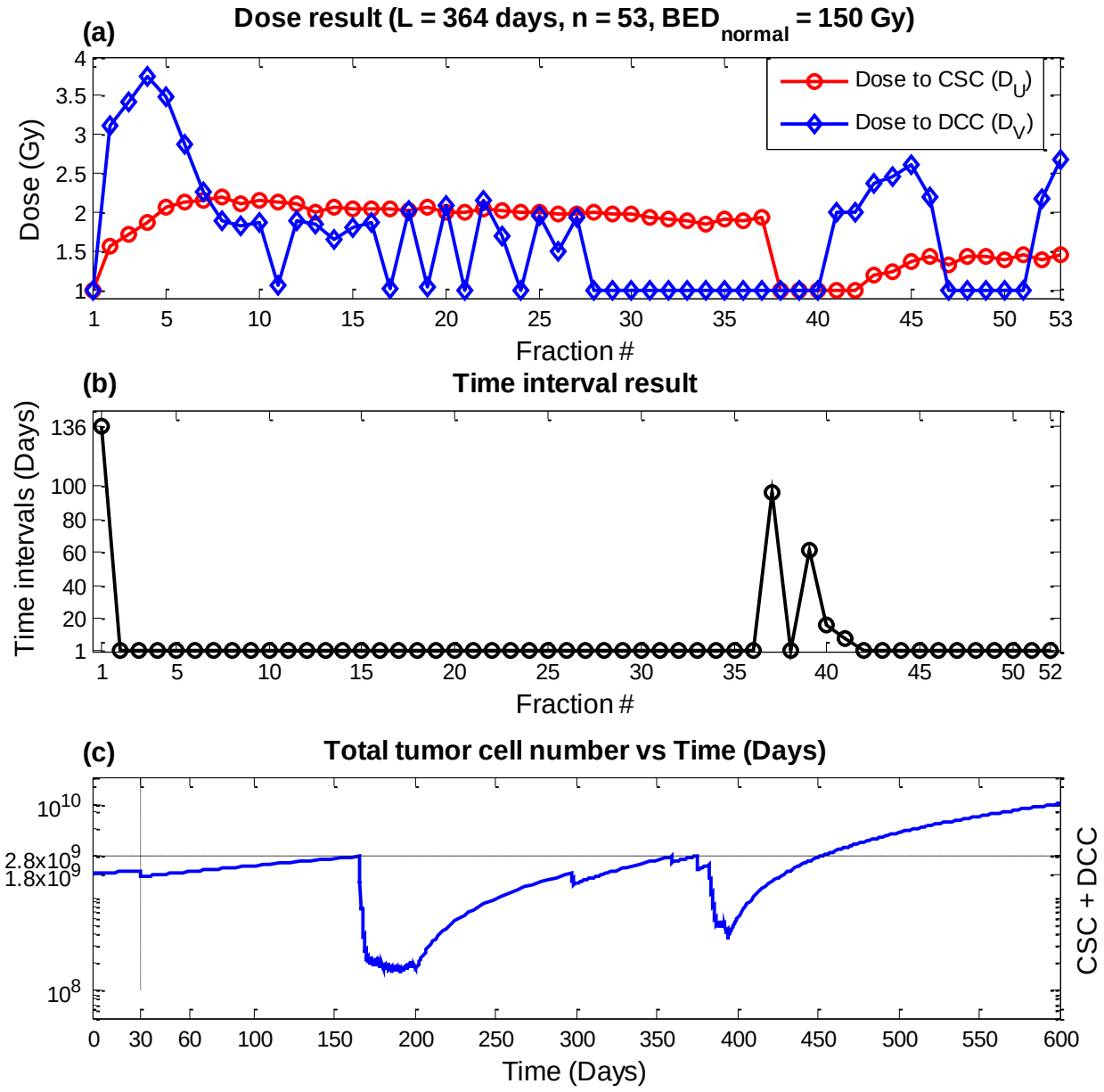

Figure 2-9: Dose escalation (BED_{normal} = 150 Gy) optimization result, total duration L = 364 days, number of fractions n = 53 (weekly equivalent). (a) $\boldsymbol{D_U}$ (red circles) and $\boldsymbol{D_V}$ (blue diamonds) (b) time interval $\boldsymbol{T}$ (c) Total tumor cells vs. time. Recurrence time with this plan was predicted to be 452 days.

2.2.4 Discussion

Without assuming different radiobiology than the well tested linear quadratic model, the previously proposed dual compartment ODE model[43] was the first radiobiological model to our knowledge capable of reconciling the perpetual radioresistance in patient and the apparent moderate radiosensitivity *in vitro* of human GBM, therefore providing us with a theoretical platform in exploring the potential in delaying GBM recurrence with differing dose fractionation schemes. We extend the model into an optimization formulation allowing for optimization of dosing temporal fractions.

Previously work focused on optimizing within the confinement of conventional once or twice per weekday treatment times, and significant improvements in outcome were shown[24-26,113]. However, the unique pattern of aggressive recurrence of GBM leads to considerably different dose fractionation strategies. As shown in our study, optimization within the conventional time frame was ineffective in substantially delaying disease recurrence, which therefore inspired the idea of treating GBM with a prolonged super hyperfractionated approach. The protracted treatment duration, along with dose fractionation optimization, resulted in recurrence delay of up to 180 days. With dose escalation to BED_{normal} of 150 Gy, which is substantially lower than the BED_{normal} of combined external beam and brachytherapy therapy trial previously conducted[100,104], the recurrence time point was further delayed to 452 days from the simulated postoperative time point. Although still not a cure, the predicted delay is not trivial in reference to one of the most effective chemotherapy for GBM by temozolomide[114] that was shown to improve median survival by 3 months.

Another interesting observation is that our results suggest super hyperfractionated treatment to be carried out in four cycles with varying strategies. The first treatment cycle consists of low and infrequent dose fractions, just enough to maintain the total tumor cell number below the recurrence level. The second cycle applies aggressive once per day treatments beginning with larger dose fractions that gradually decreases and stabilizes at a lower level. The compacted therapy quickly reduces the total number of tumor cells before moving into the third stage, without depleting the total allocated BED_{normal}. The third cycle again uses fractions spaced farther apart, mainly to maintain the total number of cells. The final phase is characterized by another series of densely spaced treatment fractions to minimize the total cell numbers as much as possible before the end of radiation therapy.

The simulated annealing (SA) optimization algorithm generally applies only one variable change within each iteration[111]. The one variable approach required a constraint check after each iteration and resulted in early local minimum convergence due to the difficulty in finding additional answers that satisfy problem constraints. The novel pair-wise opposite step size approach we have presented for this problem helped maintain the random-walk search within the time and dose domain that satisfies problem constraints, contributing to increased optimization efficiency and results far superior to that of one variable SA approach. This method can also be utilized on many other applications when the optimization constraints are not straightforward.

There are several limitations with the study. Although the model was able to successfully reproduce the aggressive regrowth of GBM after aggressive treatment, it does not take into consideration biological factors such as tumor vasculature, oxygen content, the effect of asymmetric divisions, and spatial heterogeneity. Modeling tumor

microenvironment may render the model more realistic but also increase the complexity of modeling and the uncertainty from estimating additional model parameters. Modeling the intratumoral heterogeneity may improve our capability of predicting treatment response and optimize the treatment fractionation but this study still highly simplifies an actual tumor. Rigorously designed preclinical and clinical studies are needed to test the mathematical model prediction.

2.2.5 Conclusion

A temporal dose fractionation optimization in the context of cancer stem cell dynamics and heterogeneous radiosensitivity within GBM was introduced. The model demonstrated that substantial delay in GBM recurrence could be attained with a super hyperfractionated treatment approach. Further testing is needed to validate the efficacy of this novel treatment method.

3 4π RADIOTHERAPY

3.1 Prospective clinical trial on recurrent brain glioma patients

3.1.1 Introduction

Current state-of-the-art medical digital linear accelerators are capable of delivering radiation therapy in complex dynamic trajectories that involves orchestrated movements of the gantry, couch, multileaf collimator (MLC), in conjunction with dose rate modulations. These new capabilities have motivated active research to explore the potential in further improving radiotherapy plan quality through optimization of beam orientations and dynamic trajectories, in which substantial dosimetric improvements have been shown[115-120]. The main dosimetric advantages arose from the maximal and optimal utilization of the non-coplanar beam solution space that facilitates superior spatial dose distribution shaping.

4π radiotherapy, a novel delivery technique that integrates static intensity modulated radiotherapy (IMRT) beam orientation and fluence map inverse optimization[44], has also been shown capable of significantly improving critical organ sparing compared with volumetric modulated arc therapy (VMAT) or IMRT with manually selected beam orientations in dosimetric studies for the brain[46], head and neck[47], lung[49], liver[48], and prostate[50,121].

The dosimetric benefit and potential increase in delivery efficiency of the aforementioned methods were demonstrated through retrospective dosimetric evaluations with in-house treatment planning software and automated technique implementations in Varian Developer Mode, but have not yet been translated into standard clinical workflow. Particularly for the complex techniques that involve dynamic couch motion during beam-on, clinical utilization is limited by pending commercial release and FDA approval. Clinical implementation for 4π radiotherapy, while potentially challenging due to its highly non-coplanar nature that requires extensive coordination of couch and gantry movements, is not limited by the need for further approval due to the fact that dynamic couch movements are not required during beam-on.

In this study, we demonstrate the first clinical implementation of 4π radiotherapy through a prospective clinical trial testing its feasibility, safety, dosimetric benefits, intrafractional motion, and delivery efficiency on patients with recurrent glioma, a disease that requires demanding dosimetric constraints due to primarily local recurrences.

3.1.2 Methods

3.1.2.1 Recruitment criteria and patient characteristics

The recruitment inclusion criteria include a histologic diagnosis of primary and recurrent glioma, Karnofsky performance status (KPS) greater than 70, and age of more than 18 years old. Eleven patients consented to participate in the clinical trial from December

2014 to January 2017 at University of California, Los Angeles. Patient and treatment characteristics of both the prior radiotherapy for the primary disease and the delivered plan during trial participation is shown in Table 3-1.

Pt #	Histology	Age	Sex	Prior Dose (Gy)	PTV Vol (cm^3)	Dosing Scheme	Total Dose (Gy)	Machine	# Fields	# Couch Kicks
1	GBM	54	F	59.4	13.99	5 Gy x 5	25	TrueBeam	18	12
2	GBM	64	F	60	110.14	3 Gy x 10	30	TrueBeam	19	14
3	GBM	60	F	60	0.95	5 Gy x 5	25	Novalis Tx	15	11
4	GBM	54	M	60	1.84	5 Gy x 5	25	Novalis Tx	13	11
5	GBM	52	M	59.4	124.51	3 Gy x 10	30	TrueBeam	20	15
6	GBM	48	M	60	18.17	6 Gy x 5	30	TrueBeam	15	9
7	GBM	39	M	46	47.15	3 Gy x 10	30	TrueBeam	16	10
8	EPD	80	F	54	2.57	5 Gy x 5	25	TrueBeam	17	10
9	GBM	59	M	60	3.86	5 Gy x 5	25	Novalis Tx	15	11
	Recruited but not treated with 4π							**Reason**		
10	GBM	56	M	59.4	10.94	3 Gy x 10	30	Both plans did not meet dose constraints		
11	GBM	66	M	40 + 20 SIB	141.09	3 Gy x 10	30	Comparable VMAT plan		

Table 3-1: Patient and treatment plan characteristics. SIB = simultaneous integrated boost. EPD = Ependymoma.

3.1.2.2 4π radiotherapy plan generation

An in-house 4π radiotherapy treatment planning optimization platform, as mentioned and implemented in previous publications[44,46,47,50] , was utilized to select an optimal set of twenty beam angles for each plan. The starting candidate beam pool contains 1162 beams evenly distributed throughout the entire 4π solid angle with 6° separation between adjacent beams. The beam angles that are collision-free with an isocentric set up (source to target distance of 100 cm) was determined through exhaustive search on a verified computer-aided design model of the Varian TrueBeam linear accelerator with a volunteer on the couch[62]. To perform inverse optimization of all candidate beams, dose contribution matrices with resolution of 2.5 x 2.5 x 2.5 mm^3 corresponding to 5 × 5 mm^2 beamlets were precomputed using convolution/superposition of 6MV poly-energetic X-ray

kernels. The intensity modulating beamlets were defined as all beamlets covering the PTV within the beam eye view of each candidate beam angle. A greedy column generation algorithm was utilized to iteratively select beam orientations and perform fluence optimization with all selected beam orientations until the desired number of beam angles is reached[45].

To generate a clinically deliverable and FDA approved plan, the 20 beam orientations selected by 4π were imported into Eclipse (Varian Medical Systems, Palo Alto, CA, USA) for intensity modulated radiation therapy (IMRT) planning. For increased delivery efficiency, couch kicks within 6° were merged and neighboring beam orientations with gantry and couch angles both within 20° were manually averaged and combined during planning if the plan quality can be maintained after the reduction in delivery fields. The resultant number of fields and couch kicks for each patient are shown in Table 3-1. The final beam orientations were sorted in order of couch angle to minimize couch movements during delivery. VMAT plans with 3-4 full and partial coplanar or non-coplanar arcs were also generated for each cases for comparison, and the plan achieving superior tradeoff between dosimetric quality and delivery efficiency was selected for treatment.

3.1.2.3 Pre-treatment quality assurance

Dosimetric quality assurance measurements were made on OCTAVIUS® 729 (PTW, Freiburg, Germany) for cases with PTV diameter larger than 3 cm. Field-by-field measurements were performed at the corresponding gantry angles with the couch angle maintained at the central position for all beam angles. Resultant distributions were analyzed in VeriSoft. For cases with PTV smaller than 3 cm, the relative dose distribution and absolute

point dose was verified on GafChromic film EBT3 (Ashland Advanced Materials, Bridgewater, NJ, USA) and PTW Pinpoint 3D TN31016 ion chamber with active volume of 0.016 cm^3 (PTW, Freiburg, Germany). Film results were analyzed with FilmQA Pro software (Ashland Advanced Materials, Bridgewater, NJ, USA). γ index of 3% dose difference / 3 mm distance to agreement and a 95% passing rate was used as the passing criteria for all dosimetric analyses[122].

In addition to performing patient-specific dosimetric QA, a dry run with patient-specific radiosurgical mask and couch translational positions aligned to treatment position was performed prior to the first treatment of each case. A generalized beam map containing the non-colliding beam solution space, as shown in Figure 3-1(a), was utilized to guide safe beam navigation for each case. The navigation route and intrafractional imaging time points were pre-planned and instructed to the therapist to further ensure safety.

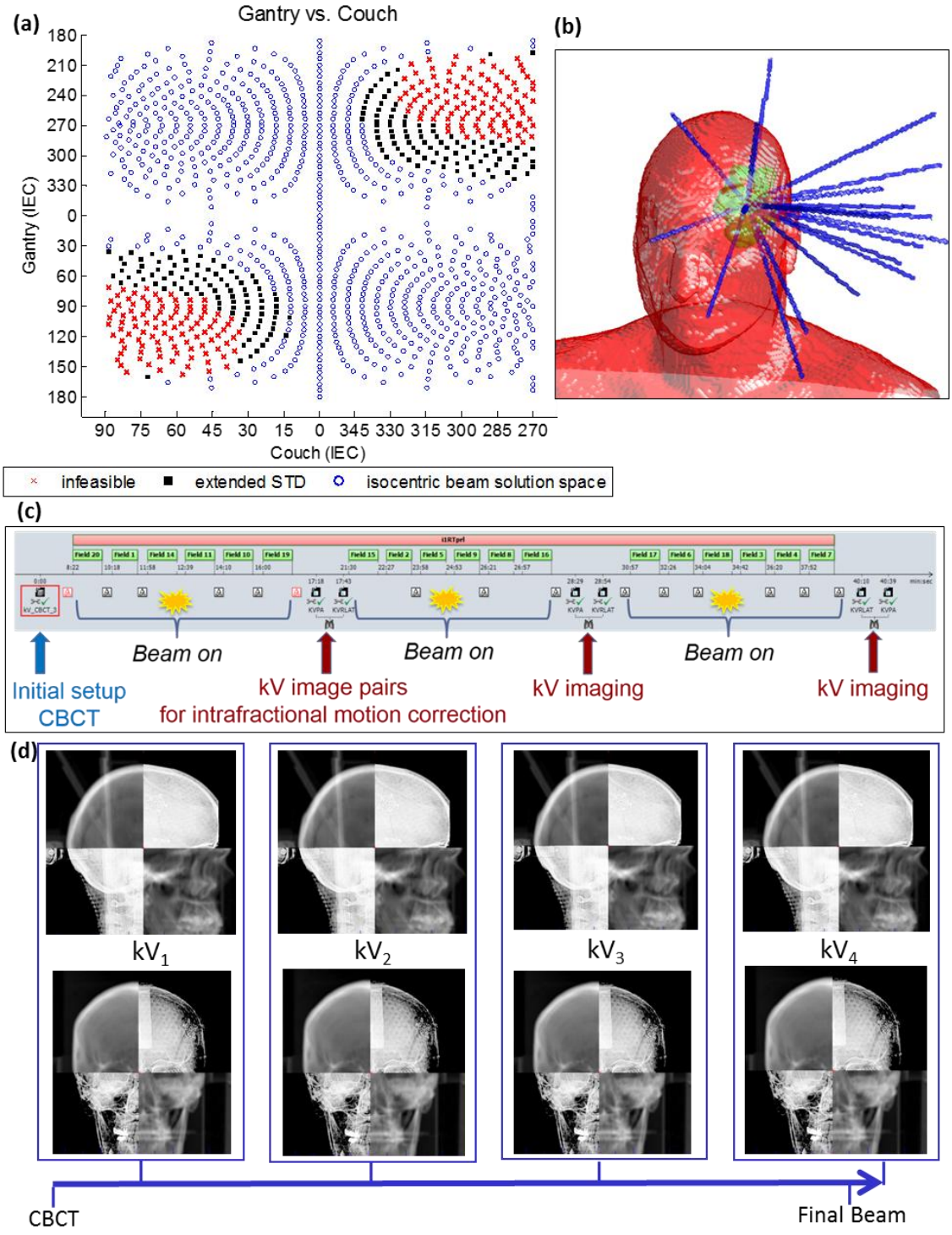

Figure 3-1: (a) Beam solution space with deliverable with isocentric setup with more than 5 cm clearance (blue hollow circles). Angles requiring extended source to target distance (STD) to avoid collision (black filled squares). Infeasible beams regardless of STD extensions (red crosses). (b) Example of Selected 4π beam orientations (c) Schematic of treatment delivery workflow. (d) Intrafractional kV imaging results acquired with the TrueBeam on-board imager.

3.1.2.4 Treatment delivery and patient survey

All patients were immobilized with radiosurgical masks during treatment. CBCT was utilized for initial set up, and intrafractional motion was evaluated by acquiring 3-4 orthogonal kV image pairs with ExacTrac (Brainlab, Munich, Germany) or the Varian TrueBeam on-board imager during each fraction. The typical treatment delivery workflow is demonstrated in Figure 3-1(c).

Treatments were delivered with the Varian TrueBeam linear accelerator or the Novalis Tx radiosurgery system. For treatments performed with the TrueBeam, remote couch rotation was utilized for increased efficiency.

Patient comfort questionnaires were collected at the end of each daily treatment with scoring of 1 – 10 for treatment tolerability, dizziness, nausea, and pain to assess and record the comfort level and potential unforeseen issues associated with 4π delivery.

3.1.3 Results

Nine out of the eleven recruited patients were treated with 4π radiotherapy. One patient was not treated because neither VMAT nor 4π met the dosimetric criteria for safe treatment due to the high dose already delivered to the brainstem in the prior irradiation. The other patient was treated with VMAT instead of 4π due to undemanding dosimetry that resulted in a comparable VMAT plan with higher delivery efficiency. An example of selected 4π beam orientations is shown in Figure 3-1(b).

Substantial OAR sparing was demonstrated with 4π compared with VMAT, as demonstrated in Table 3-2(a). Statistically significant improvements were found for the

mean and maximum dose to the brainstem, chiasm, right eye, lens, and left optic nerve. Particularly remarkable average brainstem mean dose reduction of 32.9% enabled treatments that would otherwise not satisfy safe dose constraints with VMAT, as demonstrated in example dose wash in Figure 3-2(a) below, where the dose spillage in the brainstem direction was markedly reduced by 4π. An example dose volume histogram (DVH) is shown in Figure 3-2(b) in which global OAR dose reduction is apparent, particularly for the brainstem and chiasm. The spread of mean and maximum dose of the generated 4π plans compared with VMAT relative to plan prescription dose is shown in Figure 3-3(a) and Figure 3-3(b). No statistical significant differences were found for R50 and PTV homogeneity index (D5/D95) between the 4π and VMAT plans. OAR dosimetry of the cumulative dose distribution between the previous dose delivered to the primary GBM, with prescription doses shown in Table 1 (labeled as "Prior Dose"), and the 4π or VMAT plan generated during the clinical trial, is also demonstrated in Table 3-2(b).

(a)		**Average OAR Dose Statistics (Gy)**									
		Brainstem	**Chiasm**	**Cochlea**		**Eye**		**Lens**		**Optic Nerve**	
				L	**R**	**L**	**R**	**L**	**R**	**L**	**R**
4π	**Mean**	3.30*	2.59*	2.33	1.45	0.94*	0.58*	0.64*	0.39*	2.03*	1.70
	Max	9.52*	5.00*	3.47	1.92	1.96	1.35*	0.87*	0.51*	2.96*	2.61
VMAT	**Mean**	4.37	4.69	3.05	2.04	1.62	1.52	1.30	1.30	3.10	2.19
	Max	13.01	7.04	3.81	2.79	2.59	2.42	1.59	1.61	4.30	3.02

(b)		**Average OAR Dose Statistics of Cumulative Plan (Gy)**									
		Brainstem	**Chiasm**	**Cochlea**		**Eye**		**Lens**		**Optic Nerve**	
				L	**R**	**L**	**R**	**L**	**R**	**L**	**R**
4π + PreRT	**Mean**	35.87*	31.88*	30.53	21.19	6.46*	8.78*	4.05*	5.48*	17.58*	19.70
	Max	61.44*	41.90	35.77	28.40	12.53	15.99*	5.10*	7.20*	26.58*	29.08
VMAT + PreRT	**Mean**	36.93	34.00	31.24	21.73	7.13	9.72	4.71	6.40	18.64	20.18
	Max	64.20	43.71	36.16	29.13	13.13	17.03	5.75	8.24	27.75	29.49

Table 3-2: Average OAR dose statistics comparison (n = 11). *p<0.05 from Wilcoxon signed-rank test (a) Comparison of 4π and VMAT plans generated during the clinical trial (b) Comparison of cumulative dose of previous plan (PreRT) and trial plans.

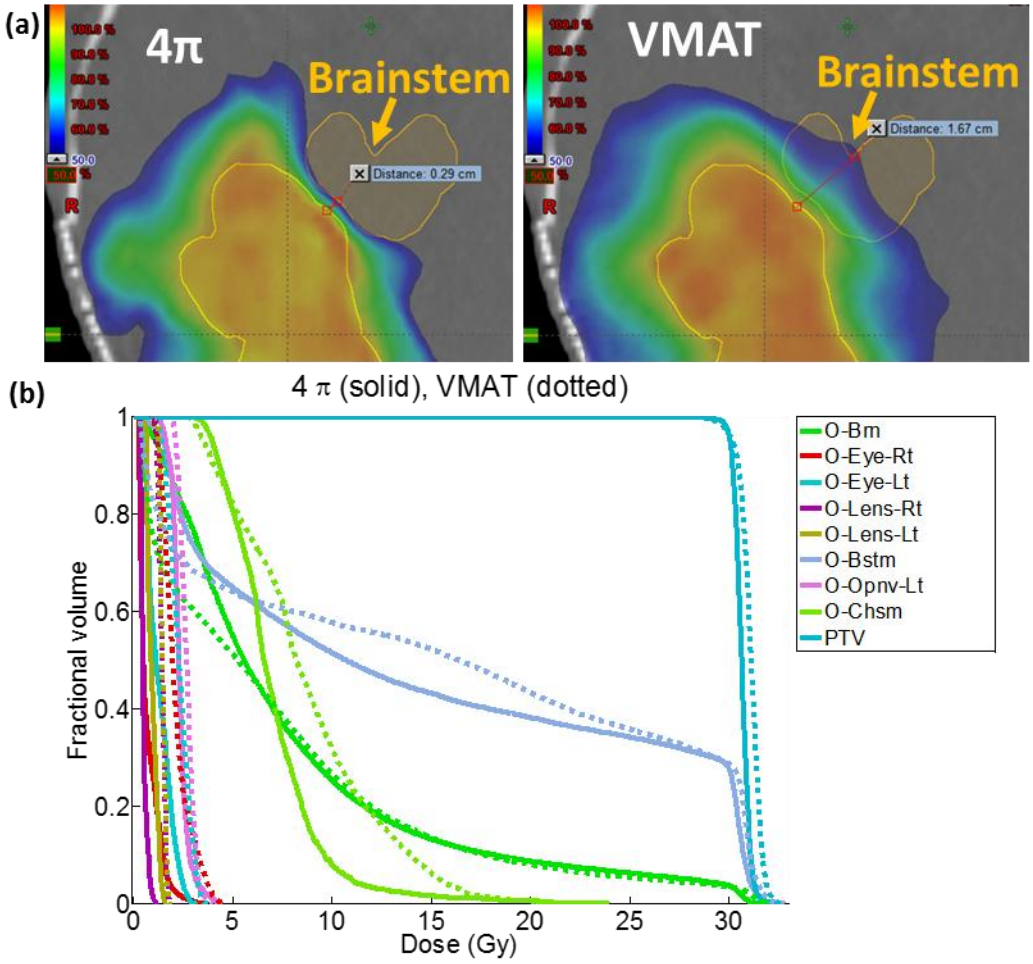

Figure 3-2: (a) 50% prescription isodose distribution. Distance from PTV to isodose edge in the brainstem direction: 0.29 cm (4π), 1.67 cm (VMAT) (b) DVH illustrating the sparing power of 4π. Global OAR sparing, particularly for the brainstem and chiasm, in addition to lower PTV maximum dose and increased homogeneity, can be visually observed.

All treatments were well tolerated with no incidents. The treatment time was 26 – 50 minutes. The fastest treatments were achieved for cases delivered on the TrueBeam with remote couch kick and ExacTrac intrafractional imaging. Factors that decreased delivery efficiency include the need to rotate the couch back to central position for on-board imaging or treatments of which remote couch kick capabilities were not available. kV imaging have shown that intrafractional motion was maintained under 1 mm for all except one acquired kV image pair, in which intrafractional couch shifts were not required. For the maximum

observed shift of 1.5 mm, an intrafractional couch shift was performed to correct for the measured displacement. The intrafractional imaging result from one case is shown in Figure 3-1(d).

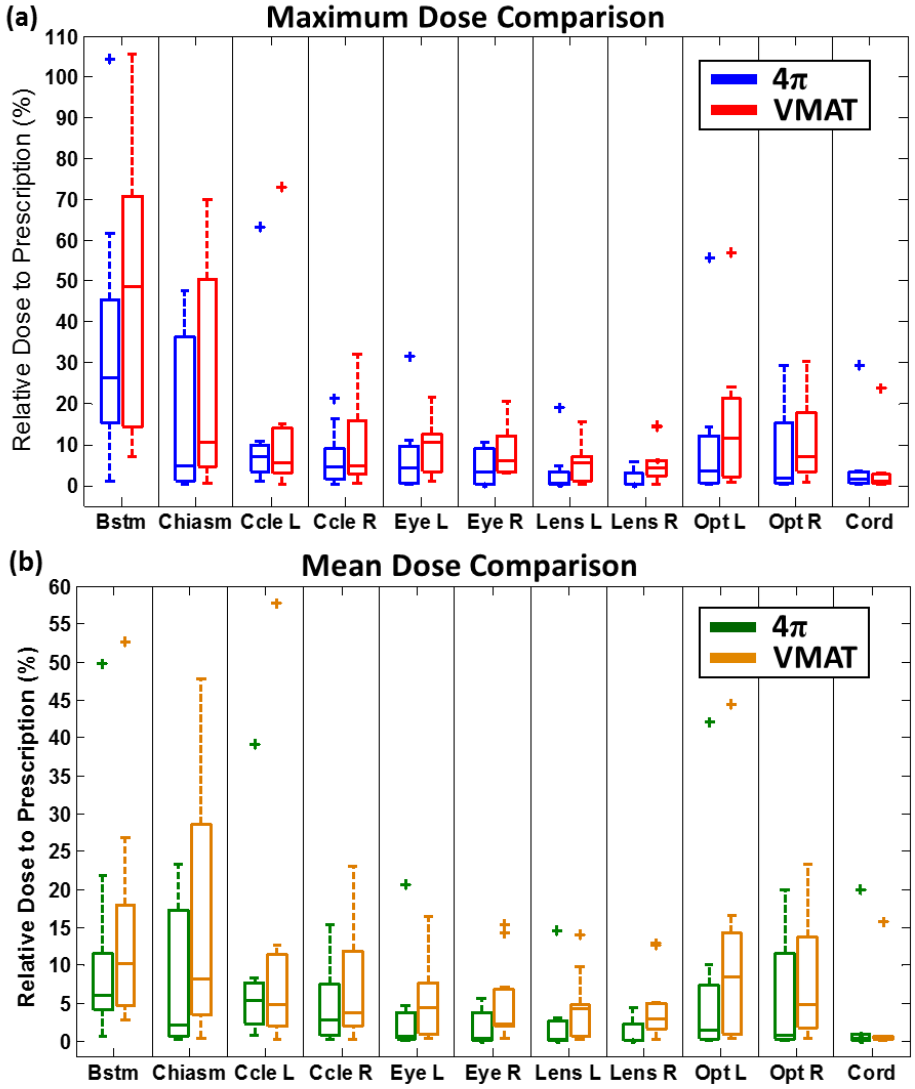

Figure 3-3: 4π vs. VMAT dosimetric comparison, dose relative to prescription dose of each plan. (a) Maximum dose, 4π (blue), VMAT (red). (b) Mean dose. 4π (green), VMAT (mustard)

Patient survey outcome with the average score from 1-10 of four categories, including treatment duration tolerability, nausea, dizziness, and pain, is summarized in Table 3-3. The average treatment tolerability score was high and the nausea, dizziness, and pain scores were low. Six out of nine patients gave full score to treatment tolerability throughout the

entire treatment course. Out of the three patients that did not perceive treatment duration to be completely tolerable, two patients reported pain and discomfort from the radiosurgical mask being too tight, with pain scores decreasing over the treatment course. One patient reported headache and dizziness throughout the treatment course that appeared to be disease symptom related rather than treatment delivery related.

Treatment Duration Tolerability	Nausea	Dizziness	Pain
8.625	0	0.66	1.07

Table 3-3: Summary of patient questionnaire**.**

3.1.4 Discussion

With advancements in linear accelerator technology and recent breakthroughs in robust optimization methods, the exploitation of radiotherapy dosimetric benefits from the noncoplanar beam solution space through optimization of static beam orientations or dynamic beam trajectories have been an active field of research, in which significant normal tissue sparing was demonstrated[44,115-117,119,120,123]. However, clinical translations of many of these complex trajectories, particular ones with couch movements during beam-on, remain difficult due to pending FDA approval and commercial release. The nature of 4π radiotherapy, in which static IMRT beams are utilized, allowed for clinical implementation through approved treatment planning and delivery systems and its utilization is not TPS or Linac-specific.

Through this study, the clinical utility and substantial dosimetric benefit of 4π was demonstrated and validated. The global inverse optimization approach that mathematically incorporates the entire non-colliding non-coplanar beam solution space and fluence map optimization resulted in dosimetry that is consistently superior to that of state-of-the-art

VMAT plans. The improvement in dosimetry allowed for the re-irradiation of patients who, having previously received high irradiation to the brainstem, experienced in-field recurrences that could not be treated with conventional planning methods which are unable to meet critical organ dose constraints. Patient motion induced by the relatively more extensive couch motions was also shown to be negligible through intrafractional imaging. Based on the collected patient surveys, the treatments were also well tolerated. Motivated by these validated advantages, 3 challenging spine SBRT cases had also been treated with 4π at UCLA, and we continue to implement the method on cases that demand superior dosimetry.

The major drawback of the technique is the prolonged treatment time. However, with the aid of pre-established couch and gantry motion sequencing from the CAD-model generated beam solution space map and dry run, treatment delivery efficiency was greatly increased with safe remote couch movements. In addition, we have also tested the feasibility and efficiency of fully automated delivery through executing XML scripts in the Varian TrueBeam Developer Mode. The automated delivery times of the 20 beam 4π treatments to the brain, lung and prostate were 10, 12, and 15 minutes[62]. These tested deliveries included additional shifts required from non-isocentric beam orientations, which were proven not necessary in this trial. Therefore, the required time could be reduced even further if all beam angles were isocentric and additional couch or beam orientation merges were made.

The feasibility of delivering 4π on commonly available Linacs with C-arm gantry provides potential in more widespread adoption of this method, especially for dosimetrically challenging cases that are unachievable with conventional planning methods. As a short-term goal, we aim to further assess the selected beam angles at different treatment sites as

our database continues to grow and generate robust treatment-site-specific beam angle templates through machine learning methods. These beam angle templates could be shared across institutions to further increase the utilization of 4π.

3.1.5 Conclusion

The feasibility, safety, and dosimetric benefits of 4π radiotherapy have been clinically demonstrated with a prospective clinical trial. Treatments were well tolerated despite prolonged treatment time, which can be substantially reduced with automation. These results pave the way for 4π implementation in many more clinically challenging cases.

3.2 The development and verification of a highly accurate collision prediction model for automated non-coplanar plan delivery[62]

3.2.1 Introduction

Radiation therapy dosimetry can benefit from expanding the beam orientation solution space to include non-coplanar beams. The improvement is particularly facilitated by recent breakthroughs in robust optimization algorithms capable of automatically solving the complex non-coplanar beam orientation/trajectory, and fluence optimization problem, such as static intensity modulated radiation therapy (IMRT)-based approaches including 4π radiotherapy[44], iCycle[115], and rotational trajectory-based volumetric modulated arc therapy (VMAT) methods including TMAT[116,124], Tra-VMAT[117], and DCR-VMAT[120]. Significant dosimetric advantages including improved dose conformality and normal organ sparing have been demonstrated for treatments to the brain[46,117], head and neck[47,125], liver[44], lung[49],

breast[116], and prostate[50,126] employing a large number of non-coplanar static beams or arcs, in comparison to current state-of the-art coplanar VMAT and IMRT techniques employing manually selected beams.

Clinical adoption of the plans using increasing number of optimally selected non-coplanar beams and arcs requires the development of corresponding quality assurance protocols. Compared to existing plans that employ dominantly coplanar beams, non-coplanar beam plans increase the possibility of collision between the gantry, couch, and patient. Furthermore, to expand the solution space to include non-coplanar beams, non-isocentric treatments with source-to-target distances (STD) beyond 100 cm that require additional couch translations between beams may be needed. A quantitative and automated process needs to be developed to predict and prevent collisions, and to be able to determine the necessary STD for each beam.

Collision prediction models have been previously developed for the purpose of evaluating collision zones for isocentric treatments and avoiding unforeseen collisions that result in re-planning and treatment delays. Humm described a computerized collision prediction method[127], where a simplified 3D surface model of the machine was used and combined with experimental measurements of potential collision points. The patient was modeled as an elliptical cylinder fixed to the couch. The method was later adopted and modified to improve visualization[128-131], incorporate patient specific external contours from the CT[132] and develop an analytical collision model that is computationally inexpensive[133]. Hamza-Lup et al. digitized the surface of individual moveable components on external beam therapy machines using 3D scanners and generated an augmented reality environment for virtual collision detection[134]. While these methods provided an approximation for collision

prediction, they were either not individualized to each patient, or have not been end-to-end tested for the purpose of non-coplanar radiotherapy. Studies in which patient specific external contours from CT images were utilized, the patient contour not only does not include the entire body, but also could not be extensively verified via measurements due to the impracticality of placing any patient on the couch for an extended period of time.

In this current study, we report a method to generate an individualized collision model, test its accuracy via extensive measurements with a phantom and then predict safety buffer distances based on measurements for various treatment sites.

3.2.2 Methods

3.2.2.1 Model construction

A highly detailed 3D computer-aided design (CAD) model of a digital linac (Varian TrueBeam, Varian Medical Systems) provided by the manufacturer was employed. To reduce the file size and improve processing time, components such as nuts and bolts that would not be involved in collisions were removed from the CAD model using engineering software Autodesk Inventor (Autodesk, San Rafael, CA). The CAD model allowed the gantry and couch to be moved according to the International Electrotechnique Commission (IEC) convention.

A hand held 3D scanner (Artec MH, Palo Alto, CA) was used to capture the surface geometry of a clothed foam anthropomorphic phantom (Zing Display, Rancho Santa Margarita, CA) in standing position. The phantom was selected for three reasons. First, the phantom material was pliant, yielding under pressure and lessening the risk of damaging the machine in case of an inadvertent collision. Second, the phantom could be placed in different

poses to facilitate testing of the collision space with various set up positions. Lastly, the full body phantom was relatively light for easy maneuvering.

3.2.2.2 3D scanner specifications and accuracy verification

The 3D scanner projected a patterned pulsed LED laser light for distance measurement. The working distance of the scanner was 0.4 m -1.0 m with 214 × 148 mm^2 field of view at the closest distance and 536 × 371 mm^2 at the furthest distance. The frame rate was 15f/s. To scan a larger or complete 3D object in the hand held mode, the camera software fused image patches from multiple views after registration. Because of the high frame rate, there was a large overlap between adjacent patches to facilitate the registration. The 3D scanning resolution was 0.5 mm according to the manufacturer.

The accuracy of the 3D camera was tested by performing a 3D scan on a rigid high precision phantom (MIMI, Standard Imaging, Middleton, WI), as shown in Figure 3-4a. The phantom dimension was 14 × 14 × 14 cm^3. The size of the scanned phantom was measured using the 3D scanning software Artec Studio (Artec Group, Palo Alto, CA).

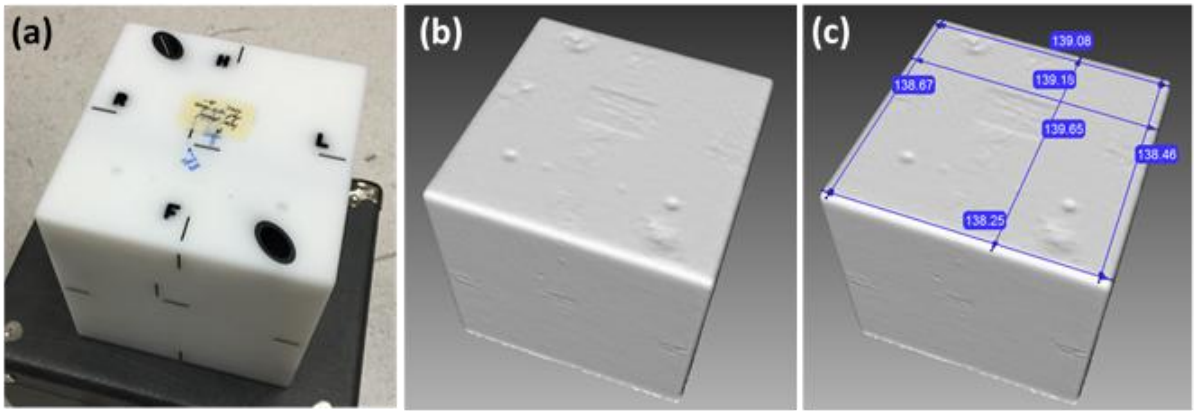

Figure 3-4: 3D scanner verification with the MIMI phantom. (a) MIMI phantom (b) resultant 3D scan (c) resultant 3D scan with 6 measurements in millimeters.

The anthropomorphic phantom surface model was then placed onto the couch within the CAD model to explore the linac non-coplanar collision space. The same method was used to incorporate a human subject surface in the CAD model[50]. The complete CAD model of the TrueBeam system with the phantom on the couch within is shown in Figure 3-5a.

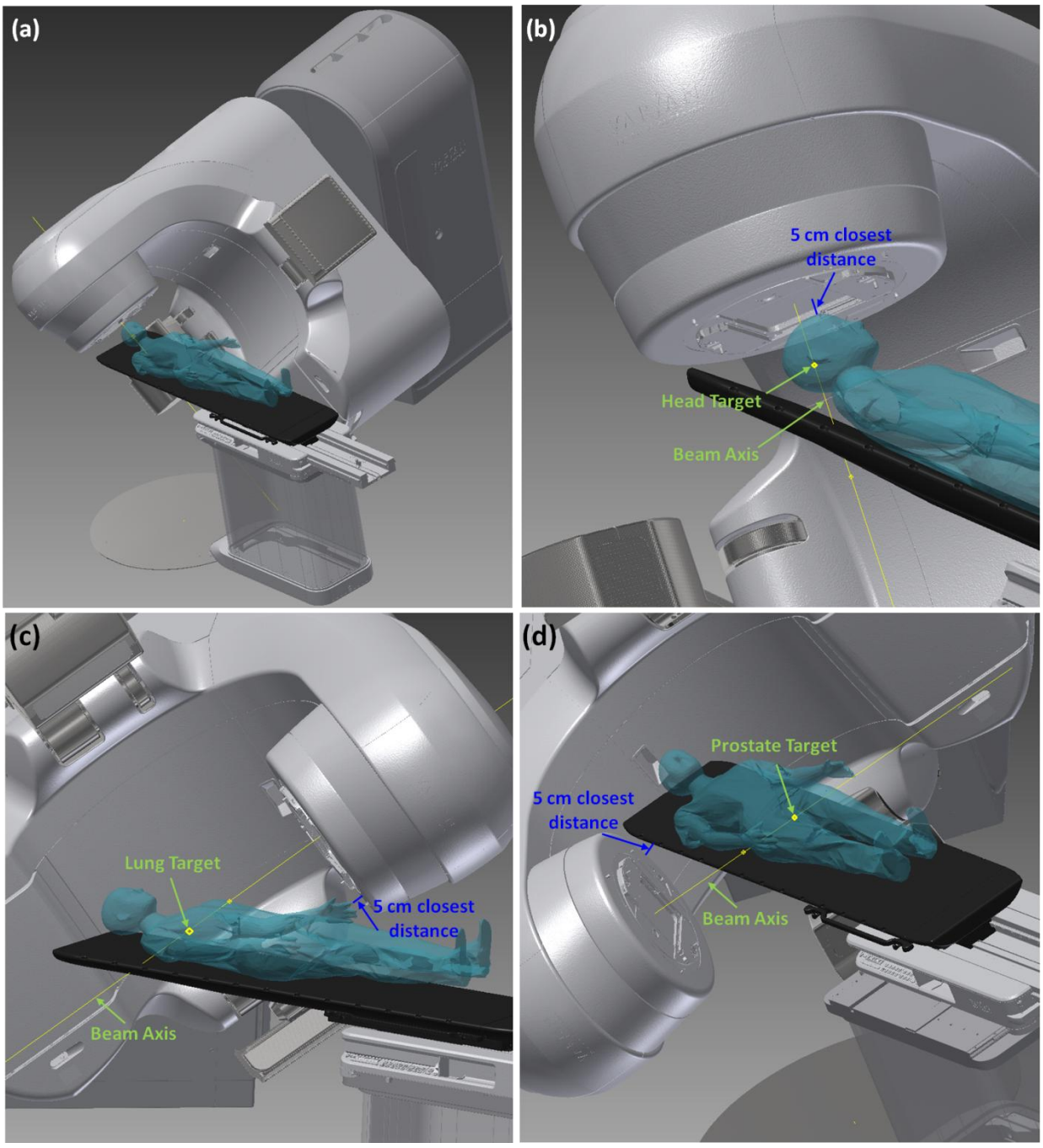

Figure 3-5: Minimum distance measurement demonstration in CAD (a) full CAD model within Autodesk Inventor with phantom on couch (b) example 5 cm closest distance measurement for treatment to the head. (c) 5 cm closest distance measurement to lung (d) closest distance measurement to prostate.

3.2.2.3 Verification between model and physical system with phantom measurements

To explore and verify specifically the non-coplanar beam candidate pool for treatments to the head, lung, and prostate, representative targets of interest of all three sites were added to the phantom surface model. For each treatment site of interest, 100 couch and gantry angle combinations were uniformly sampled from the candidate pool of 1162 beams with 6 degrees of separation between 2 nearest neighbor beam pairs throughout the entire 4π steradian. For each beam angle, the couch position was translated along the beam axis until the closest distance from the gantry to the couch or patient was 5 cm within the CAD model, using Equation 3-1,

$$\begin{cases} Lat = \Delta r \sin\theta \cos\phi + Lat_0 \\ Lng = \Delta r \sin\theta \sin\phi + Lng_0 \\ Vrt = \Delta r \cos\theta + Vrt_0, \end{cases}$$

Equation 3-1

where Δr indicated the displacement of target from the isocenter, θ and ϕ indicated the gantry and couch angles, respectively. The gantry and couch angles followed the IEC convention, as demonstrated in Figure 3-6. Lat_0, Lng_0, and Vrt_0 were the couch lateral, longitudinal, and vertical axes positions at which the treatment site of interest was aligned to the machine isocenter. Demonstrations of the closest distance measurements between gantry to patient or couch for treatments to the head, lung, and prostate are shown in Figure 3-5b, Figure 3-5c, and Figure 3-5d, respectively. The phantom was positioned on the linac couch based on the CAD model (equivalent to a treatment plan) and all 300 gantry and couch positions (100 positions from each treatment site) were transferred to the linac for measurement. The measurement setup is shown in Figure 3-7. Since the phantom 3D surface model was obtained in standing position, there was a gap between the posterior phantom

head and feet surfaces and the couch top. To stabilize the phantom, cushions were placed under the phantom head and feet during measurement. An inside caliper (iGaging, San Clemente, CA) was used to measure the closest distances on the machine setup. The distance discrepancy data points between the CAD and machine measurements were separated into six groups based on the treatment site and measurement location (couch or phantom). The Shapiro-Wilk normality test with an α level of 0.05 was performed on each dataset. For the groups that did not satisfy the normality hypothesis, a double Gaussian fit was performed to find a distribution that best represented the discrepancy data points. The curve fit performance was verified with the Kolmogorov-Smirnov test at an α level of 0.05. The determined distributions were used to estimate safety margins with 0.1%, 0.01%, and 0.001% probability of collision for all six groups based on the treatment site and whether the measurement was gantry-to-couch or gantry-to-patient. The collision probability selected above roughly represents 1 collision per day, 10 days, and 100 days, assuming 30 treatments per day and ~30 beams per treatment.

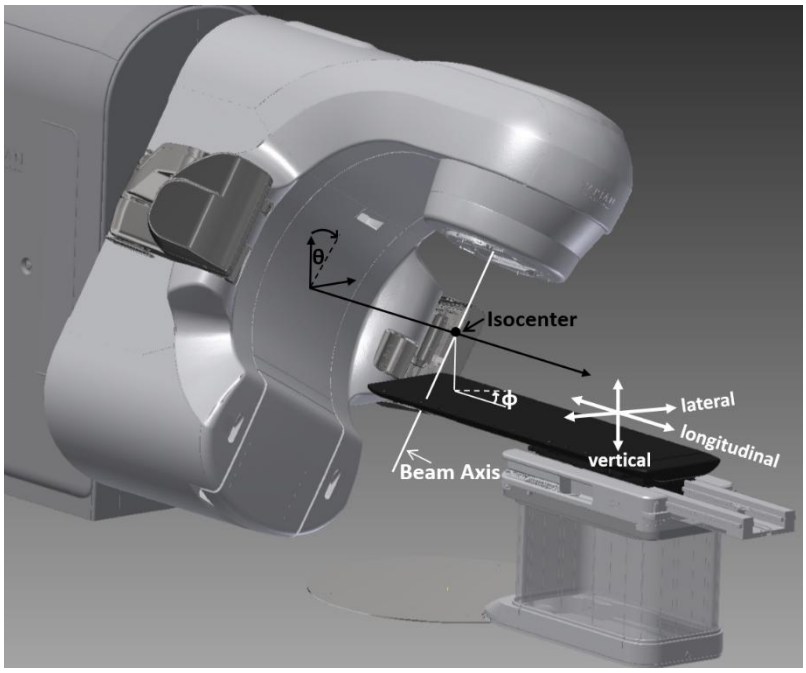

Figure 3-6: IEC convention and couch translations

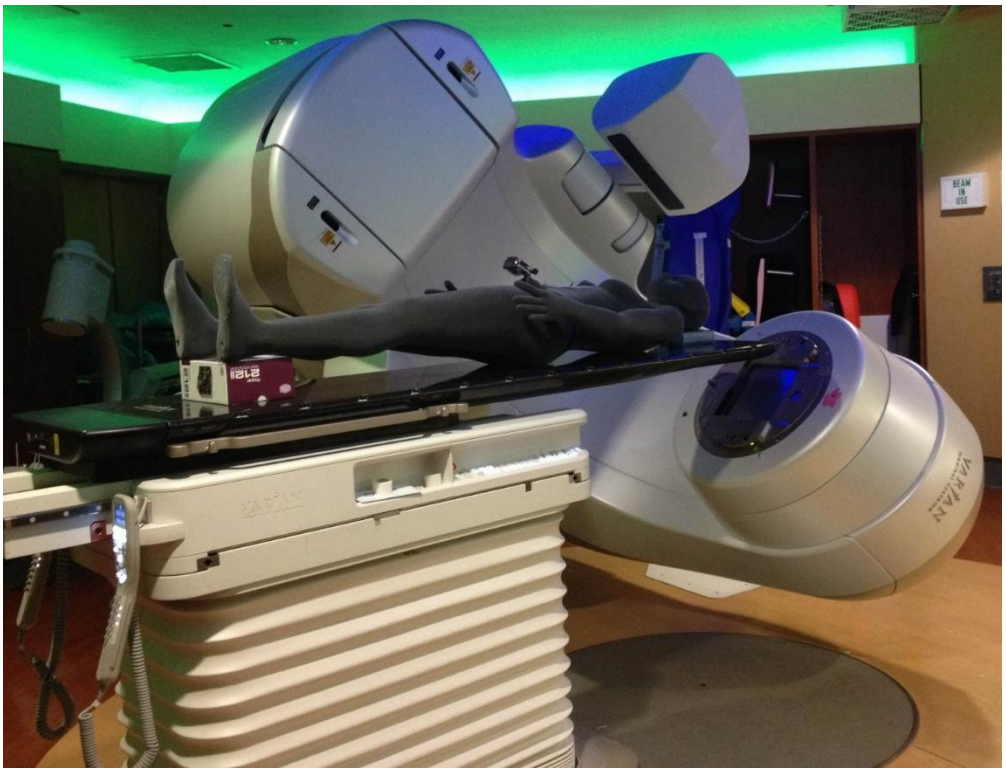

Figure 3-7: Machine measurement setup.

3.2.2.4 Automated 4π delivery

To examine the feasibility and speed of automated treatment delivery, 4π optimized beam angles and the corresponding Eclipse optimized MLC sequences of 20 beam brain, lung, and prostate plans were converted into XML script for automatic delivery in the Varian TrueBeam developer mode. The number of beams requiring extended STD to avoid collision within the generated XML delivery brain, lung, and prostate plans were 3, 3, and 6, respectively. The beam angles were sorted in order of couch rotation angle to minimize total couch motion. A GoPro camera was attached at the phantom eye level during the programmed delivery to examine the patient eye view of automated delivery. The whole automated delivery was recorded and timed.

3.2.2.5 Exploration of collision-free beam angle solution space with human subject model

With the developed model, exhaustive search was performed to examine the available beam angle solution space for treatments to the head, lung, abdomen, and prostate. The exhaustive search was performed with a 3D scan of a healthy volunteer placed on the modeled couch. The model was made into an interactive X3D format where the couch and gantry could be moved according to machine specific locations via MATLAB scripts. The collision status and the particular combination of elements (couch top, couch pedestal, gantry, or imagers) resulting in collision can also be obtained from the model for any linac orientation. For each treatment site, couch shifts were performed within the model to align the desired treatment target location to the isocenter. For each beam angle within the 4π candidate pool of 1162 beam angles, the minimum STD that was deliverable without collision was automatically calculated by incrementally moving the couch translational axes

positions from isocentric setup position via MATLAB control to extend or shorten the STD based on the collision status of each step until the minimum collision-free STD was found. Using the minimum distance information, the beam angles were sorted into six categories: deliverable with conventional isocentric setup (source-to-target distance (STD) = 100 cm), deliverable only with extended STD between 100 and 110 cm (100 < STD ≤ 110), 110 and 120 cm (110 < STD ≤ 120), 120 and 130 cm (120 < STD ≤ 130), more than 130 cm (STD > 130 cm), and undeliverable. The undeliverable beams resulted in either gantry-to-couch or gantry-to-patient collision, or required one or more couch translational axes to exceed the allowed mechanical range.

3.2.3 Results

3.2.3.1 3D scanner accuracy verification

The resultant scan and measurements are shown in Figure 3-4b and Figure 3-4c. The average of 6 measurements was 138.88 ± 0.52 mm or 0.8% relative error.

3.2.3.2 Verification between model and physical system with phantom measurements

The mean and maximum absolute values of measurement discrepancies and the summary statistics of all discrepancies as either single or double Gaussian distributions for all groups are shown in Table 3-4. For the double Gaussian distributions, the mixture weight of the first listed distribution (μ_1, σ_1) is represented in the column labeled w_1. The discrepancy histograms of all gantry-to-couch and gantry-to-phantom measurements are shown in Figure 3-8 and Figure 3-9, respectively. The discrepancy values between the gantry and couch were all less than 1 cm. The discrepancies between the measurement and the CAD

model for gantry-to-phantom distances were greater with a maximum deviation measurement of 2.97 cm, which resulted from a phantom to gantry distance for prostate treatment.

Estimates of treatment-site-specific and overall safety buffer distances with 0.01%, 0.001% and 0.0001% probability of collision between the gantry to couch or phantom based on the fitted Gaussian distributions are also shown in Table 3-5. The maximum discrepancy and safety margin estimates were largest for treatments to the prostate for both gantry-to-couch and gantry-to-phantom measurements. The larger discrepancy values of the prostate measurements resulted from the larger number of closest distance measurements from the gantry to the phantom extremities such as the legs and hands, whose positions cannot be exactly reproduced. The non-normality of the gantry-to-phantom distributions were most likely resulted from the differing setup deviation for different parts of the phantom, as the setup reproducibility for the phantom torso and head were better than its extremities. It is apparent from Figure 3-8 that the distribution of gantry-to-couch prostate measurements is non-normal due to outliers. The three outliers resulted from measurements close to the couch corners, which we concluded was due to measurement errors in determining the exact set of two points that resulted in the closest distance between two curved surfaces for each measurement.

Couch to Gantry									
		|Machine -CAD|		Machine - CAD					
	# of meas.	Mean	Max	normality	w_1	μ_1	σ_1	μ_2	σ_2
Head	62	0.24	0.72	Yes		-0.004	0.29		
Lung	61	0.17	0.61	No	0.66	-0.11	0.05	-0.12	0.001
Prostate	62	0.15	0.95	No	0.86	-0.08	0.01	-0.19	0.27
All	185	0.18	0.95	No	0.59	-0.11	0.01	-0.02	0.12
Phantom to Gantry									
		|Machine -CAD|		Machine - CAD					
	# of meas.	Mean	Max	Normality	w_1	μ_1	σ_1	μ_2	σ_2
Head	38	0.88	2.95	Yes		0.68	0.94		
Lung	39	0.80	2.19	Yes		0.23	0.99		
Prostate	38	1.45	2.97	No	0.86	1.48	0.65	-0.32	2.09
All	115	1.04	2.97	Yes		0.71	1.10		

Table 3-4: Gantry to couch and gantry to phantom measurement statistics.

Couch to Gantry				Phantom to Gantry			
Safety Buffer Distances (cm)				Safety Buffer Distances (cm)			
Collision Prob.	**0.1%**	**0.01%**	**0.001%**	**Collision Prob.**	**0.1%**	**0.01%**	**0.001%**
Head	0.89	1.07	1.23	**Head**	2.24	2.83	3.35
Lung	0.75	0.89	1.01	**Lung**	2.83	3.45	3.99
Prostate	1.48	1.87	2.19	**Prostate**	3.87	4.93	5.73
All	0.98	1.21	1.41	**All**	2.68	3.37	3.97

Table 3-5: Treatment-site-specific safety buffer distance estimations with different collision probabilities.

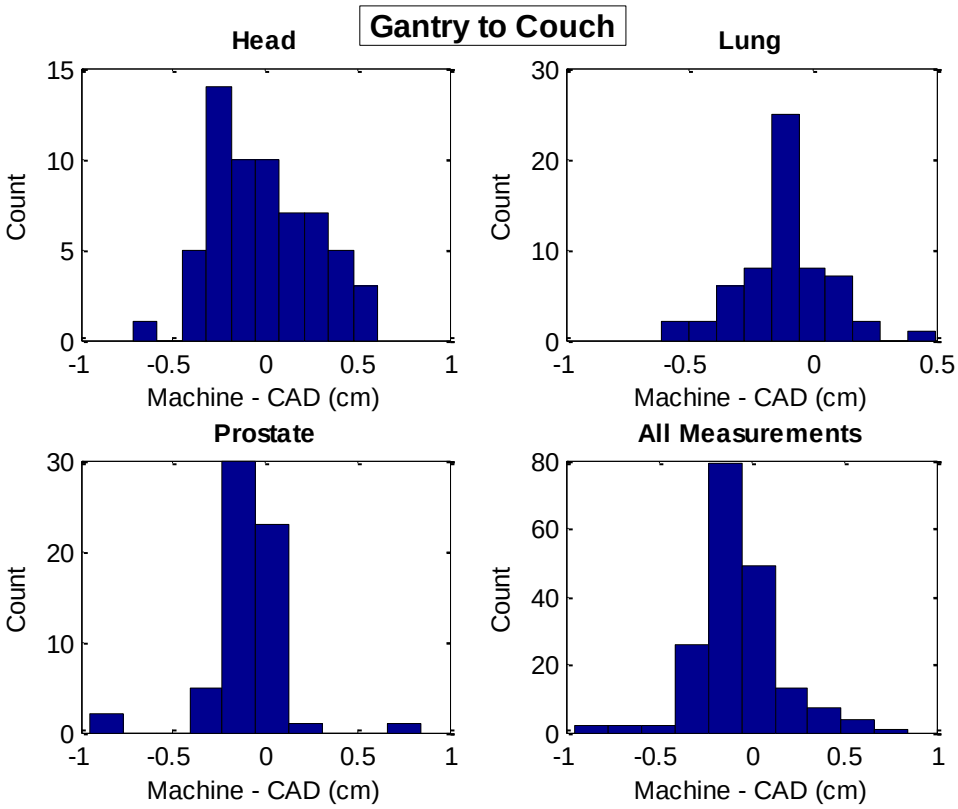

Figure 3-8: Distance discrepancy histograms for gantry to couch measurements.

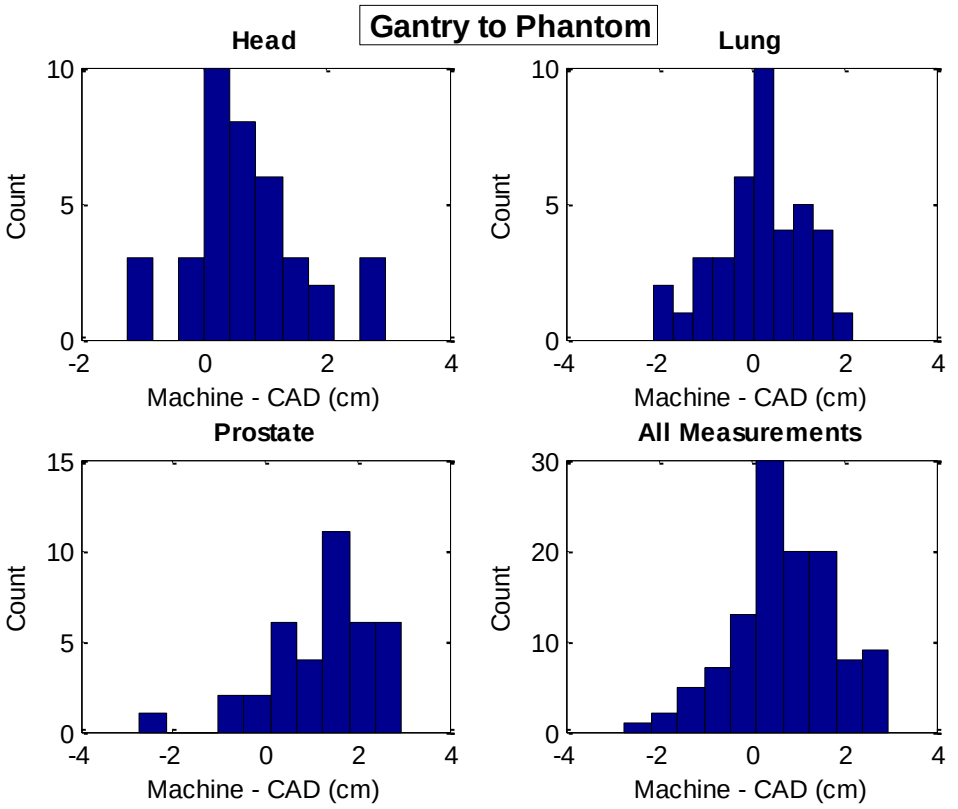

Figure 3-9: Distance discrepancy histrograms for gantry to phantom measurements.

3.2.3.3 Automated 4π delivery

The automated delivery times of the 20 beam 4π treatments to the brain, lung, and prostate were 10, 12 and 15 minutes. The number of MLC segments generated by Eclipse for the delivered brain, lung, and prostate cases were 582, 205, and 265. The patient point-of-view video along with a synchronized room-view video for the brain case, and the room-view videos for the lung and prostate cases are represented in Figure 3-10, Figure 3-11 and Figure 3-12. The XML files of all three deliveries are available as supplementary material to this paper. All videos were sped up 8 times.

Figure 3-10: Automated brain treatment with room-view and patient-eye view (Multimedia View URL: http://dx.doi.org/10.1118/1.4932631.1)

Figure 3-11: Automated lung treatment with room view (Multimedia View URL: http://dx.doi.org/10.1118/1.4932631.2).

Figure 3-12: Automated prostate treatment with room view (Multimedia View URL: http://dx.doi.org/10.1118/1.4932631.3).

3.2.3.4 Exploration of collision-free beam angle solution space with human subject model

The distribution of beam angles in the standard STD, extended STD, and undeliverable categories for each treatment site based on a healthy volunteer are shown in Table 3-6. The scanning time was approximately 15 minutes while the subject was in the standing position. The model of the healthy volunteer on the couch is shown in Figure 3-13. As expected, treatment to the head allowed for a larger number of total angles and standard STD angles compared with the lung, abdomen, and prostate cases. The total number of deliverable beams reduced from 963 for treatment to the head to 842 for treatment to the prostate. In addition, only 55% of the beams that were deliverable in the standard STD setup

for the head remained deliverable in the standard STD setup for the prostate treatment. The extended and standard STD beam solution space surfaces for treatment of the head, lung, abdomen, and prostate are demonstrated in Figure 3-14a-d, respectively. While these images show an intuitive rendering of the collision space, it is helpful to express them in Linac coordinates to guide beam orientation selection and navigation. The gantry vs. couch angles of treatments to the head, lung, abdomen, and prostate are shown in Figure 3-15a-d with the standard STD beams shown as blue hollow circles, extended STD beams shown in black, where $100 < STD \leq 110$, $110 < STD \leq 120$, $120 < STD \leq 130$, and $STD > 130$ categories are specified as squares, triangles, diamonds, and plus signs, respectively, and undeliverable beams shown as red crosses.

	All Available Beams	Deliverable with standard STD	Deliverable with extended STD
Head	963	786	177
Lung	955	452	503
Abdomen	943	471	472
Prostate	842	435	407

Table 3-6: Beam angle distribution in standard STD, extended STD, and undeliverable categories for treatments to the head, lung, abdomen, and prostate

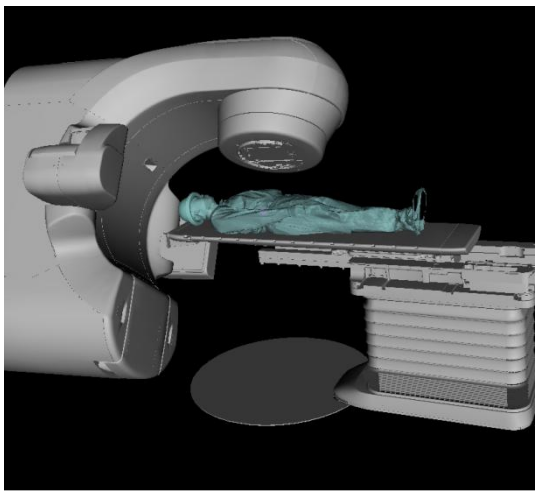

Figure 3-13: Exhaustive search model with healthy volunteer model on couch

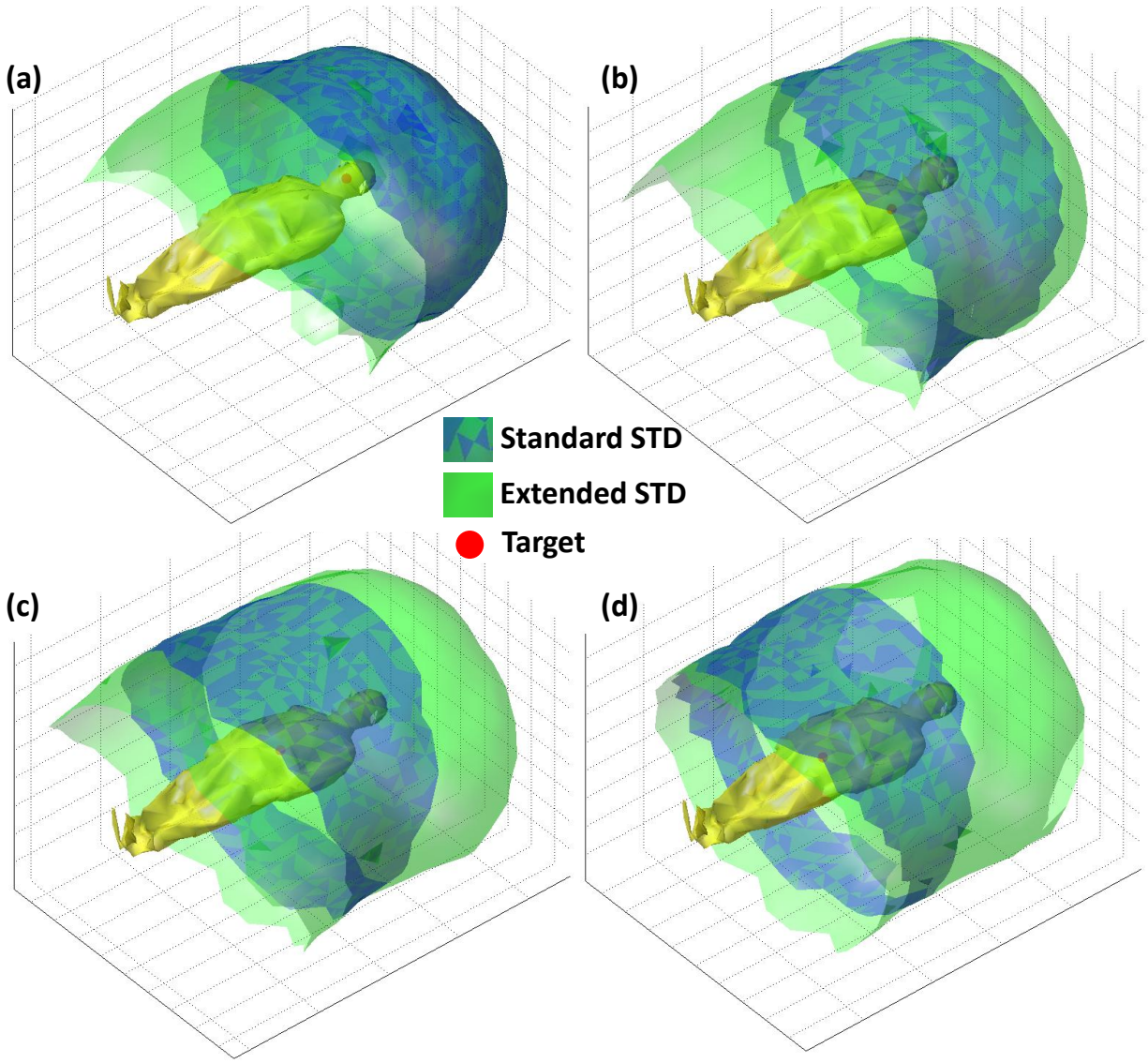

Figure 3-14: Treatment-site-specific beam solution space for standard and extended STD setups. (a) head (b) left lung (c) abdomen (d) prostate

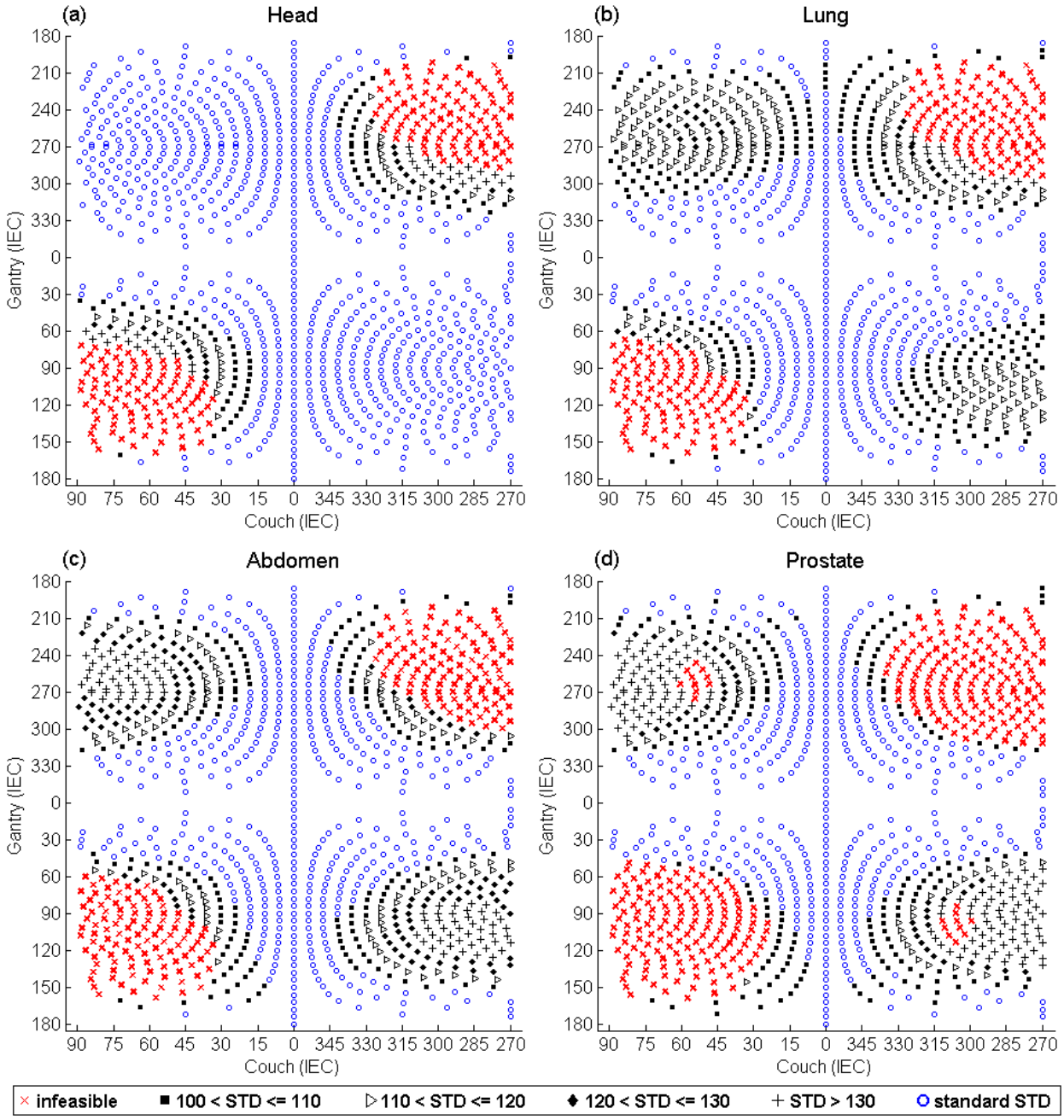

Figure 3-15: Gantry vs. couch angle plots for treatment to the head, lung, abdomen and prostate. The infeasible, standard STD beams are represented as red crosses and blue hollow circles, respectively. Extended STD beams are shown in black, separated into four categories: $100 < STD \leq 110$, $110 < STD \leq 120$, $120 < STD \leq 130$ and $STD > 130$, represented as squares, triangles, diamonds, and plus signs.

3.2.4 Discussion

With the emergence of digital linacs, innovative and effective algorithms to automate the beam orientation/trajectory and fluence map optimization, there has been a renewed interest in non-coplanar radiotherapy. For example, for centrally located and larger lung tumors, late radiation toxicity still remains a major limitation in delivering effective tumor control dose[135]. For recurrent head and neck patients, delivering high dose to the tumor while sparing previously treated organs-at-risk is also still extremely challenging[136]. With 4π radiotherapy, we have demonstrated for both these clinical scenarios the potential for dose escalation and significant improvements in critical organ sparing, tumor control, and PTV coverage[47,49]. Using optimized non-coplanar trajectories in VMAT, Wild et al. showed that the critical organ mean and max doses can be reduced by 19% for nasopharyngeal patients, compared to coplanar VMAT plans[125]. Fahimian et al., Liang et al., and Popescu et al. also demonstrated significant $V_{50\%}$ volume reduction of up to 49% for accelerated partial breast irradiation (APBI) with optimized couch and gantry dynamic arc rotation trajectories[116,124,137]. The significant dosimetry improvement observed in aforementioned studies should motivate clinical adoption of non-coplanar IMRT and trajectory-based VMAT for wider applications. For example, a prospective clinical trial is undergoing at UCLA to test the safety, efficiency, and patient tolerance for plans using inverse-optimized non-coplanar IMRT beams.

A major difference between highly non-coplanar treatments and conventional coplanar treatments is the need for substantial couch motion. Quality assurance procedures have been previously developed to evaluate the dosimetric and geometric fidelity of treatment techniques involving couch motion[138]. The positional accuracy, velocity

constancy, and accuracy for dynamic couch motion were evaluated by performing a series of tests within Varian developer mode. The tests demonstrated the programmed couch translation accuracy to be within 0.01 cm, with rotation accuracy of 0.3˚. The test provided the realistic performance accuracy boundary of an aspect of the digital linac for extensive couch movements. However, the geometric modeling and QA needs for collision avoidance for such treatments had not been addressed.

To overcome these challenges, we introduced a patient specific collision prediction model. The model was based on a vendor provided machine CAD geometry and patient 3D surface created using 3D scanning technology. The accuracy of the model was measured on the Linac.

Based on our measurement, the CAD model of the gantry and couch was accurate within 1 cm including the uncertainties that arose from measuring the minimal distance between two blunt objects. Other sources of error included the slight deformation of the fiberglass gantry cover due to gravity and the magnification effect of couch rotational uncertainties at a distance from the rotational axis. A 0.3˚ couch rotational error would introduce a 5.2 mm translational error at 1 meter away from the rotational axis. In practice, some of the newer clinical systems such as the TrueBeam used in this study already contain robust built-in motion interlocks to prevent collisions between the gantry and couch based on CAD models. However, modifications to the machine surface, including accessories on the gantry and the addition of third party 6 DOF couch top would require new CAD models to predict the collision-free space.

The slightly larger uncertainties in determining the gantry-to-phantom distances were caused by the following reasons. First, there was an intrinsic limitation in the hand-held 3D scanning accuracy. Based on the relative measurement error of the scanner, for a 1.8 m tall phantom, the measurement error would be 1.5 cm for extreme points. The uncertainty could be reduced by using room mounted 3D cameras that would be more stable, along with further camera calibration. Second, the flexible phantom extremities were not immobilized, which is typical in patient treatment. However, the use of a whole body immobilization device may help reduce the uncertainty compared with the phantom used in this study. Despite our best effort in setting up the phantom according to the CAD model, there were residual errors. This uncertainty particularly contributed to the prostate site where the flexible phantom extremities were frequently in the close proximity to the gantry. Finally, the phantom surface yielded under pressure, which made measurement of the minimal gap distances more difficult. In practice, all the uncertainties in the phantom study would still contribute to the patient collision modeling, but the risk of collision can be effectively minimized by employing buffer distances.

The discrepancies between model and measurement were used to calculate safety margin distances with 0.1%, 0.01%, and 0.001% probability of collision between the gantry to couch or phantom. Applying Gaussian predicted safety buffer distances to all beam orientations could be biased by outliers involving situations such as glancing angles and tends to overestimate the buffer. The error distribution could also depend on individual patients, immobilization device, and treatment sites. We will prospectively acquire more patient data to better understand the statistics in a future study.

By establishing a collision model that includes a patient model, the deliverable beams and the extended STD needed for certain beam orientation and treatment sites could be determined. Therefore, the collision model is an integrated component of the automated planning system utilizing the entire feasible non-coplanar beam space. For pelvis treatments, the isocentric treatment beam solution space significantly decreases the number of useful beams. The ability to use extended STD beams is essential in maintaining the size of the non-coplanar beam solution space and maximizing the dosimetric benefits. Our model provides a quantitative guidance for selecting these beams and choreographing the gantry and couch motion to achieve these positions as demonstrated in the automated plan delivery in the TrueBeam developer mode. Both the collision space modeling and automation are shown essential as the plan complexity increases.

It is also important to point out that in practice, we should not rely only on the 3D modeling to ensure treatment safety. Secondary and possibly tertiary collision prevention mechanisms should be in place to stop the machine when it is within a preset proximity to the patient. On the other hand, the 3D modeling should minimize the chance of triggering the secondary interlock and maintain the clinical flow.

3.2.5 Conclusion

In this study, an individualized collision prediction model was developed and verified. With help from the model, we have demonstrated the feasibility of fully automated non-coplanar treatment delivery on a digital linac. This work motivates further developments of clinical workflows and quality assurance procedures to allow more

extensive use and automation of non-coplanar beam geometries for improved radiation dose conformality.

3.3 Spine stereotactic body radiation therapy (SBRT) with 4π radiotherapy

3.3.1 Introduction

More than 1.5 million new cancer cases are diagnosed in the Unites States annually[139], resulting in approximately 600,000 deaths, up to 40% of which exhibit spinal metastases[140,141]. Spinal tumors can cause pain, instability, and progressive myelopathy that results in the loss of motor, sensory, and autonomic functions, significantly affecting the patients' quality of life[142,143]. As cancer treatment efficacy and patient life expectancy continues to improve, increased occurrence in symptomatic spinal metastases has been observed[144-146]. Radiation therapy remains the cornerstone in the management of the disease through palliation of pain and prevention of neurological symptoms and pathological fractures[147]. Stereotactic radiosurgery (SRS) and stereotactic body radiotherapy (SBRT), which utilize highly conformal and modulated treatment planning techniques with accurate tumor localization from image-guided radiotherapy (IGRT), has enabled the safe delivery and quick pain relief in 80-90% of treated cases[148-150]. However, the deliverable prescription dose remains limited by the tolerance of the spinal cord due to the close proximity and encompassing geometry between spinal lesions and the spinal cord, and the associated risk of irreversible radiation-induced myelopathy[151-154]. Many study protocols, such as the ongoing Radiation Therapy Oncology Group (RTOG) 0631 trial[155], exclude tumors less than 3mm from the spinal cord for this reason. This exclusion criteria prevents patients with the

highest risk of spinal cord compression from receiving treatment. Furthermore, in-field recurrence was observed at the epidural space that received lower dose to spare the spinal cord[156]. In addition, in patients with advanced malignancies, treatment on vertebrae adjacent to those already irradiated or re-irradiation of local recurrence is commonly needed. However, these treatment become even more challenging as a result of the further limited allowable dose to the spinal cord and are therefore frequently avoided due to the fear of irreversible spinal cord damage. The aforementioned challenges and evidence illustrate the necessity to further improve target coverage and OAR sparing in spine SBRT and SRS cases.

4π radiotherapy, an inverse optimization platform integrating beam orientation and fluence map optimization, has achieved substantial dosimetric improvements for brain[46], head and neck[47], liver[44,48], lung[49], and prostate[50,121] treatments compared with volumetric modulated arc therapy (VMAT) and intensity modulated radiation therapy (IMRT) with manually selected beam angles. A prospective trial of the technique has also been performed to test its clinical feasibility, safety, and dosimetric sparing capabilities in recurrent Glioblastoma Multiforme patients[157]. The purpose of this study is to demonstrate the significant organ at risk (OAR) sparing achievable with 4π radiotherapy in spine SBRT and SRS cases.

3.3.2 Methods and Materials

3.3.2.1 Patient Selection

Twenty-three spine SBRT patients, with a total of twenty-five treatment plans and prescription doses ranging from 14 to 45 Gy were included in this study. All patients were

treated using the NovalisTx linear accelerator with VMAT or IMRT at University of California, Los Angeles. The patient and case specific fractionation schemes, plan information and parameters are shown in Table 3-7. Three plans contained simultaneous integrated boost (SIB) targets.

Patient ID	PTV Vol (cc)	Location	Gy x fx	SIB Location	Gy x fx	Clinical Plan Delivery Method
1	1.4	S3	20 x 1			2 Arc VMAT
2	12.9	T6	20 x 1			4 Arc VMAT
3	24.5	T6	6 x 5			2 Arc VMAT
4	34.1	L5	16 x 1			4 Arc VMAT
5	31.8	T11	16 x 1	T12	18 x 1	4 Arc VMAT
6	5.9	L3	16 x 1			4 Arc VMAT
7	4.6	T5	20 x 1			9 Field IMRT
8	110.3	L1	6 x 5			2 Arc VMAT
9	24	L2	12 x 3			4 Arc VMAT
	45	C3	8 x 5			4 Arc VMAT
10	25	L5	16 x 1			4 Arc VMAT
11	37.6	T7T9	9 x 5			4 Arc VMAT
	29.6	L1	16 x 1	L1	20 x 1	4 Arc VMAT
12	15.6	T1	16 x 1			4 Arc VMAT
13	7.2	C2-3	7 x 3			4 Arc VMAT
14	20.1	T8	16 x 1			2 Arc VMAT
15	0.3	C1	5 x 5			2 Arc VMAT
16	14.9	C7	16 x 1			2 Arc VMAT
17	77.3	T9-10	14 x 1	T9-10	20 x 1	2 Arc VMAT
18	12.6	T1	14 x 1			4 Arc VMAT
19	10.3	T3	20 x 1			9 Field IMRT
20	33.3	T10	16 x 1			4 Arc VMAT
21	7.9	T5	16 x 1			4 Arc VMAT
22	14.5	C1	16 x 1			4 Arc VMAT
23	73.9	T9	3 x 10			2 Arc VMAT

Table 3-7: Patient and plan information

3.3.2.2 4π Radiotherapy Plan Generation

An in-house 4π radiotherapy treatment planning optimization platform, as mentioned and implemented in previous publications[44,46,47,50] , was utilized to select the

optimal twenty beam angles for each selected spine SBRT plan. The optimization begins with a candidate beam pool of 1162 beams evenly distributed throughout the entire 4π solid angle with 6° separation between adjacent beams. With a detailed and verified surface model of the Varian TrueBeam linear accelerator with a volunteer on the couch, an exhaustive search of all candidate beams were performed and the candidate angles that resulting in collision between the gantry and couch or patient were eliminated[62]. As the selected spine SBRT cases had target locations that varied greatly, all plans were separated into four spinal segment including, cervical (C1 – 7), top thoracic (T1 – 6), bottom thoracic (T7 – 12), lumbar and sacral (L1 – 5 and S1 – 5). A distinct candidate beam angle pool was obtained for each spinal segment specified above to account for variation in collision based on the location of the target. To perform inverse optimization of all non-colliding candidate beams, dose matrices with resolution of 2.5 x 2.5 x 2.5 mm^3 corresponding to 5 × 5 mm^2 beamlets were calculated using convolution/superposition of 6MV poly-energetic X-ray kernels. A column generation algorithm[45] was utilized to iteratively select and optimize beam fluence until the desired 20 beam angles were selected.

The extension of source to target distances allows for more non-colliding beam angles and may result in superior OAR sparing. However, the need to extend the source-to-target- distances (STD) for certain beam angles can greatly increase delivery complexity. Therefore, plans with candidate beam pools containing only beams deliverable isocentrically without extra couch translations during the treatment course were also created for all cases. These isocentric plans optimized using the 4π planning procedure described previously will be referred to as “isocentric 4π” plans in this manuscript. The comparison between the standard 4π and isocentric 4π plans allows for an evaluation of the tradeoff between OAR

sparing and delivery efficiency. To ensure unbiased comparison between the original clinical plans, standard 4π and isocentric 4π plans, the optimal beam angles of each 4π plan were imported into Eclipse (Varian Medical Systems, Palo Alto, CA) for dose recalculation using identical dose calculation methods and optimization parameters. The Wilcoxon signed-rank test with α value of 0.05 was utilized to compare the standard 4π and isocentric 4π plans against the original clinical plans. OAR statistics were generated for both the entire patient cohort and for each spinal segment. The number of candidate beams for each spinal section is shown in Table 3-8 and the spatial distribution of the candidate angles is displayed in Figure 3-16.

Spinal Section	Standard 4π	Isocentric 4π
C1-7	957	810
T1-6	953	695
T7-12	945	536
L1-5 + S1-5	909	544

Table 3-8: Number of candidate beams for each spinal section based on collision modeling

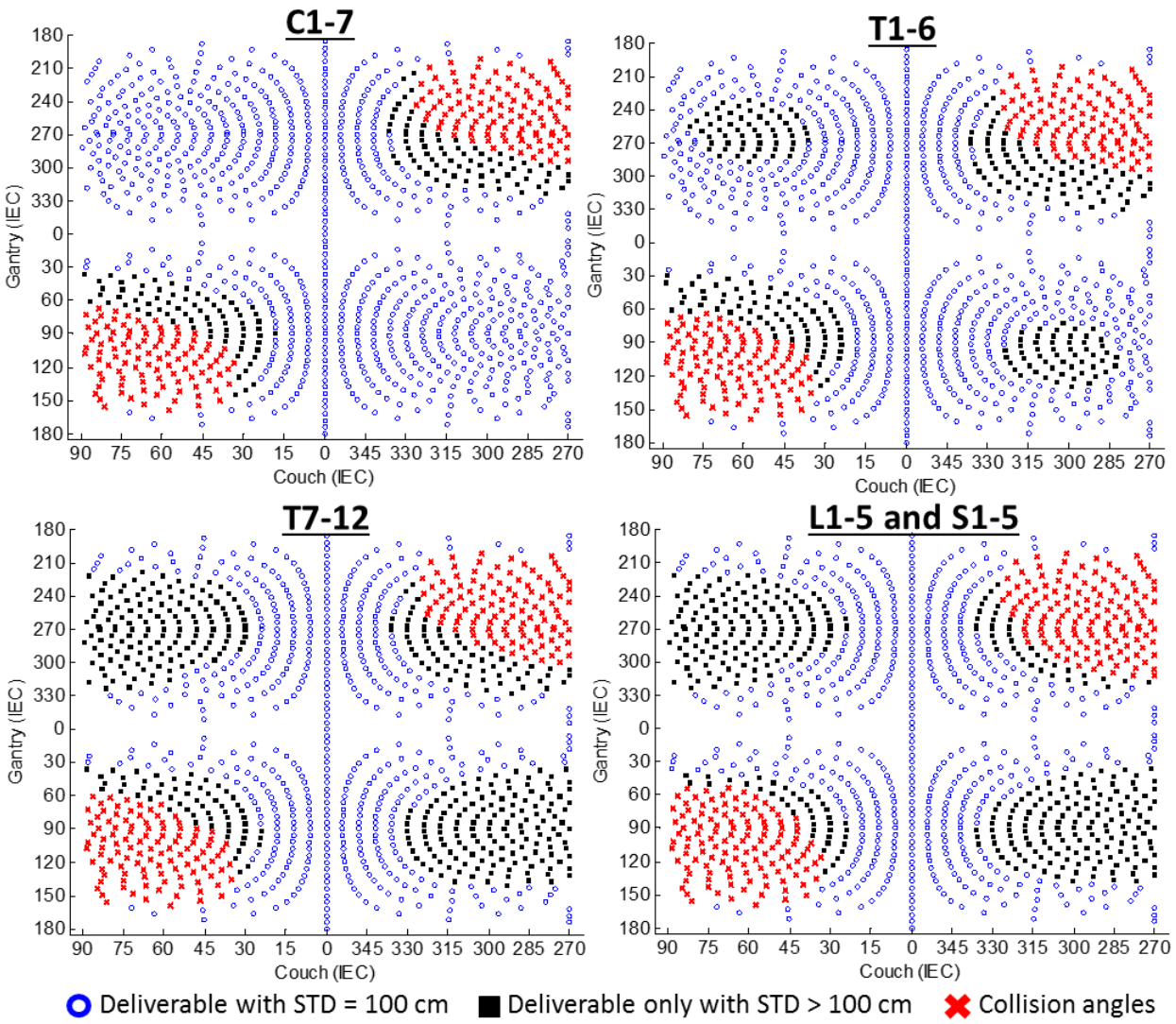

Figure 3-16: Gantry vs. couch angle plots for all four spinal sections. Isocentric 4π includes only the angles deliverable with source to target distances (STD) of 100 cm (blue hollow circles). Standard 4π encompasses all beam angles that do not result in collision (blue hollow circles + black solid squares).

3.3.3 Results

Substantial global OAR dosimetric sparing was demonstrated for both standard 4π and isocentric 4π plans. All dose reduction metrics below are reported as percent dose reductions from the prescription dose of each case relative to the original clinical plan, as demonstrated in Equation 3-2.

$$\text{Dose Reduction (\%)} = \frac{|\text{Dose} - \text{Dose}_{\text{clinical}}|}{\text{Prescription Dose}} \times 100$$

Equation 3-2

The dose reduction statistics for all OARs appearing in more than 6 plans and their corresponding p value obtained with Wilcoxon signed rank test are reported in Table 3-9. Corresponding box plots for the maximum and mean dose reductions are shown in Figure 3-18a and Figure 3-18b. The volume of the spinal cord receiving more than 50% of the prescription dose ($V_{50\%}$) was also calculated for all plans and a box plot representing the percent volume reduction relative to the clinical plan is shown in Figure 3-18c. $V_{50\%}$ of the spinal cord was significantly different from the original clinical plans for both standard and isocentric 4π with $p<0.001$, with average percent reduction of 79.9% and 80.1%, respectively, from that of the original clinical plan. Paired signed rank test between standard and isocentric 4π was also performed and no significant differences were found for mean, maximum OAR doses and $V_{50\%}$ of the spinal cord. Statistically significant improvements were also found in the PTV homogeneity index (D5/D95) and the PTV maximum dose for all generated 4π plans. It is evident that isocentric 4π plans achieved dosimetric performance equivalent to that of the standard 4π plans, indicating that the superior dosimetric quality could be achieved without the increased delivery complexity that is associated with beam angles requiring extended source to target distances in standard 4π. Examples of optimized 4π beam patterns for each spinal section are shown in Figure 3-20. The beam angle distribution of all isocentric 4π cases with each spinal section marked in different colors is shown in Figure 3-21. Overall, slightly more posterior beam angles were selected. In addition, for the T7-12 section, no anterior beam angles were selected in order to avoid abdominal OARs.

Average OAR Percent Dose Reduction from Clinical Plan (%)									
		Standard 4π				Isocentric 4π			
	n	Maximum Dose		Mean Dose		Maximum Dose		Mean Dose	
		%	p value	%	p value	%	p value	%	p value
Cord	23	11.84*	<0.001	14.17*	<0.001	12.03*	<0.001	14.37*	<0.001
Esophagus	13	21.17*	<0.001	8.52*	<0.001	19.97*	<0.001	8.22*	<0.001
Bowel	6	8.15*	0.031	2.54	0.109	8.45*	0.031	2.73	0.109
Kidney Rt	7	3.49	0.148	1.71	0.406	4.08	0.109	1.90	0.406
Kidney Lt	6	4.46	0.063	1.54	0.281	4.62	0.063	1.78*	0.031
Liver	7	1.89	0.422	2.97	0.109	2.41	0.422	2.92	0.055
Cauda	6	15.32*	0.031	9.04	0.031	15.27*	0.031	8.95*	0.016

Table 3-9: OAR percent dose reduction from clinical plan relative to the prescription dose of each plan. *statistically significant reduction ($p<0.05$), obtained from one-sided Wilcoxon signed rank test

A dose volume histogram (DVH) comparing the clinical, isocentric 4π, and standard 4π plans for one case with the T6 segment receiving 20 Gy is demonstrated in Figure 3-17. The corresponding clinical plan was generated with 4 VMAT arcs. Visual demonstration of the spinal cord sparing capability is displayed in Figure 3-19 with the dose wash and DVH comparisons of an SIB case with 16 Gy to T11 and 18 Gy to T12.

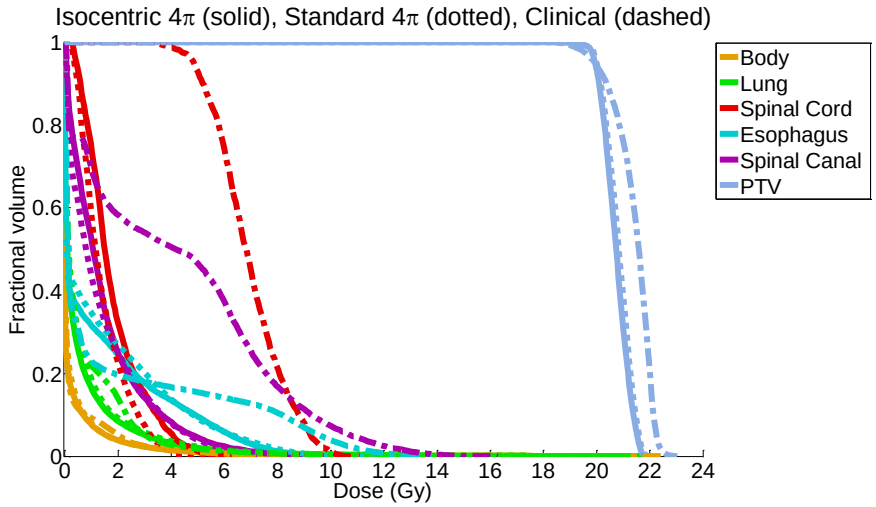

Figure 3-17: DVH comparing clinical, isocentric 4π, and standard 4π for treatment to T6

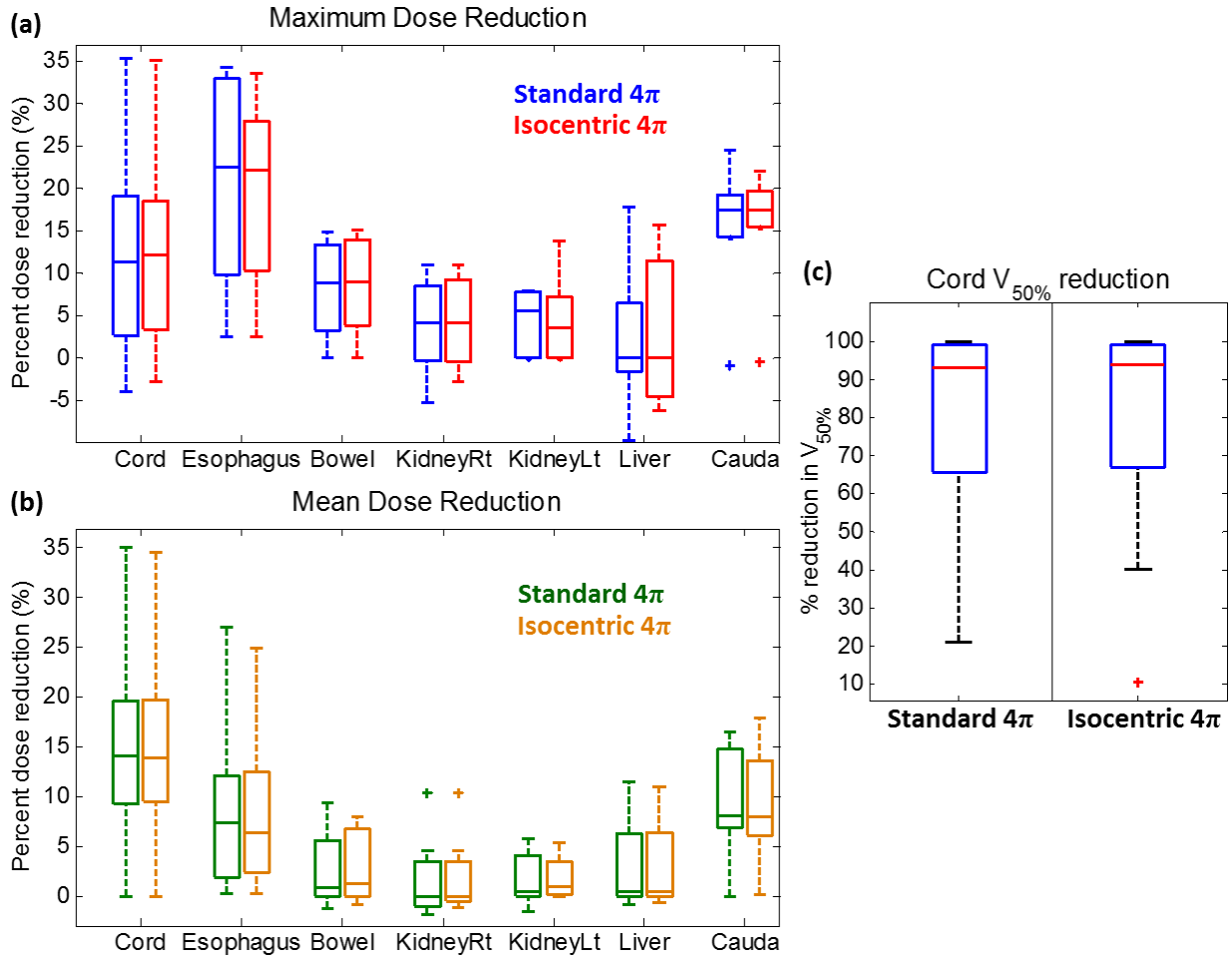

Figure 3-18: OAR dose and volume reduction box plots from the original clinical plans (a) Maximum dose reduction. Standard 4π (blue) and Isocentric 4π (red). (b) Mean dose reduction. Standard 4π (green) and Isocentric 4π (yellow) (c) Percent volume reduction in spinal cord receiving more than 50% of prescription dose ($V_{50\%}$).

Spinal Cord					
		Maximum Dose		Mean Dose	
Spinal Section	n	%	p-value	%	p-value
C1-7	5	9.47	0.063	16.30*	0.031
T1-6	7	11.30*	0.008	13.21*	0.008
T7-12	6	20.70*	0.016	22.76*	0.016
L1-5 + S1-5	5	5.21	0.125	4.01	0.063
Esophagus					
T1-6	7	16.92*	0.008	8.22*	0.008
T7-12	5	26.07*	0.031	7.63*	0.031
Additional OARs in section L1-5 + S1-5					
Cauda	5	15.17	0.063	9.52*	0.031
Bowel	5	10.14*	0.031	3.28*	0.094
Kidney Rt	5	6.29	0.063	2.79	0.219
Kidney Lt	5	5.54	0.063	2.14*	0.031

Table 3-10: Average dose reduction OAR statistics of isocentric 4π plans with spinal section breakdown. *$p<0.05$, statistically significant difference between isocentric 4π and corresponding clinical plans.

To evaluate the variation in the sparing capability from one spinal section to another, dose statistics of the spinal cord, esophagus, in addition to other OARs with more than 5 cases in the section of interest are shown in Table 3-10. Spinal cord mean dose sparing remained statistically significant for sections C1-7, T1-6, and T7-12, and the maximum dose reduction was significant for both thoracic sections. Esophagus mean and maximum dose sparing were substantial for both thoracic sections.

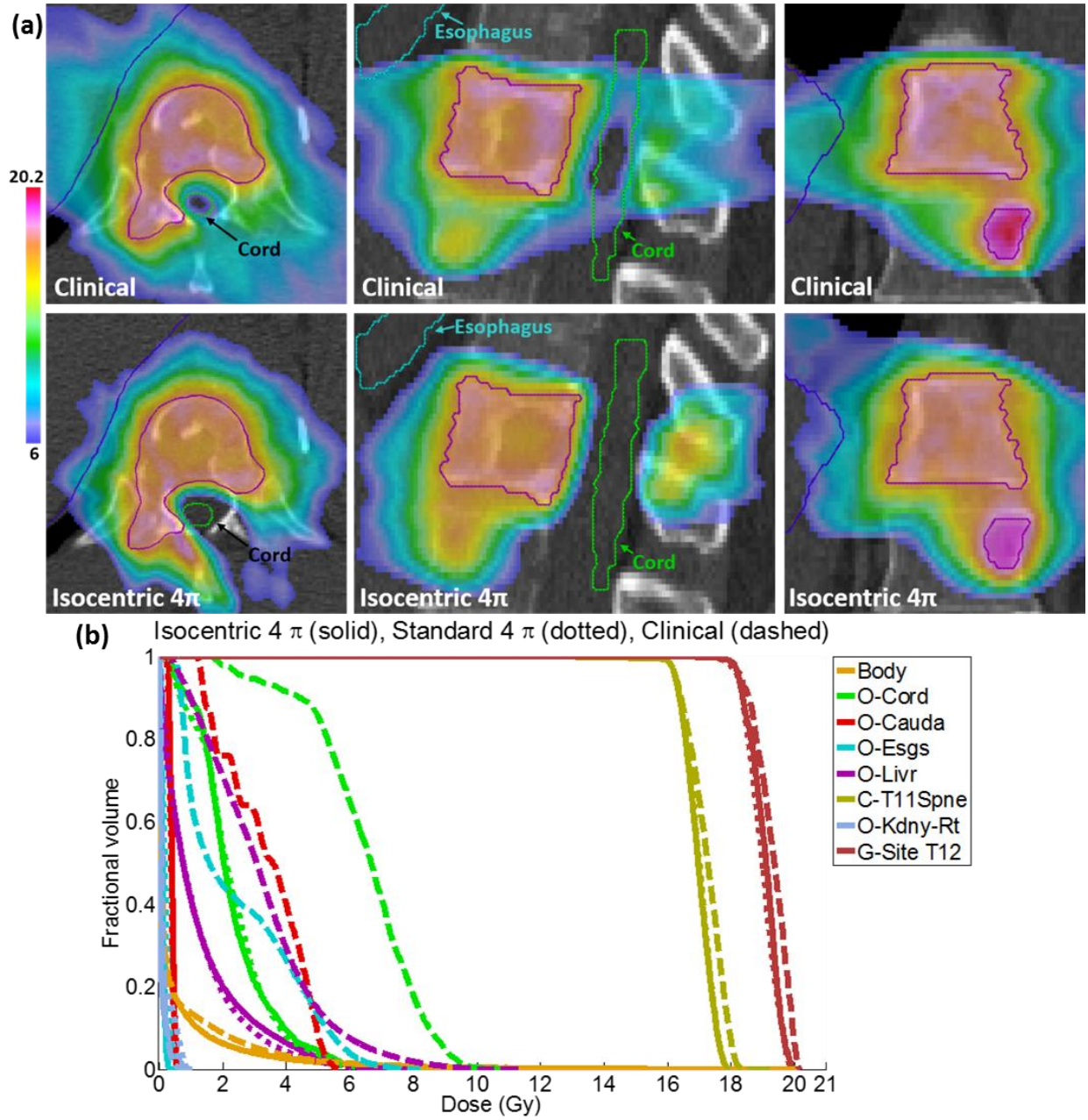

Figure 3-19: Dose comparison of a case with 16 Gy delivered to T11 and 18 Gy simultaneous boost to T12. (a) Dose wash comparing dose distributions above 6 Gy between the 4 Arc VMAT clinical plan and isocentric 4π plan. (b) DVH of the clinical, isocentric 4π, and standard 4π plans

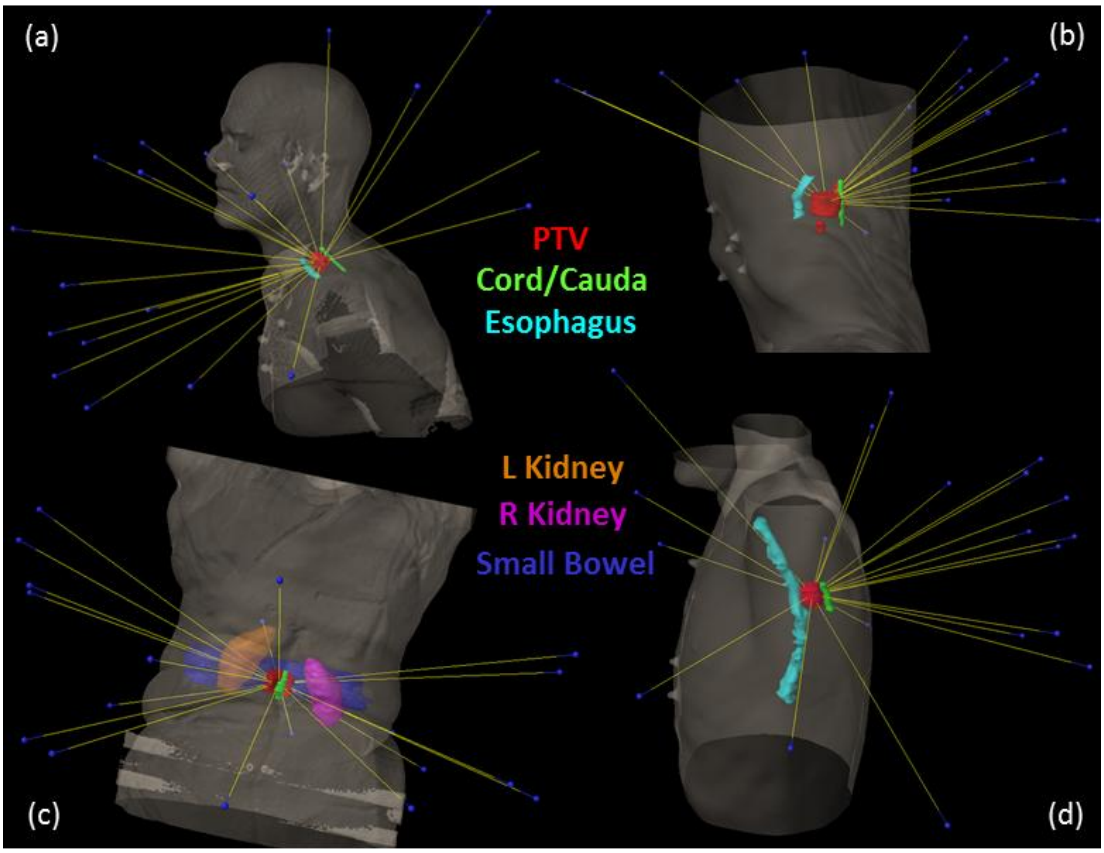

Figure 3-20: Beam orientation visualization from various spinal target locations (a) C1 (b) T11 and SIB T12 (c) L1 (d) T6

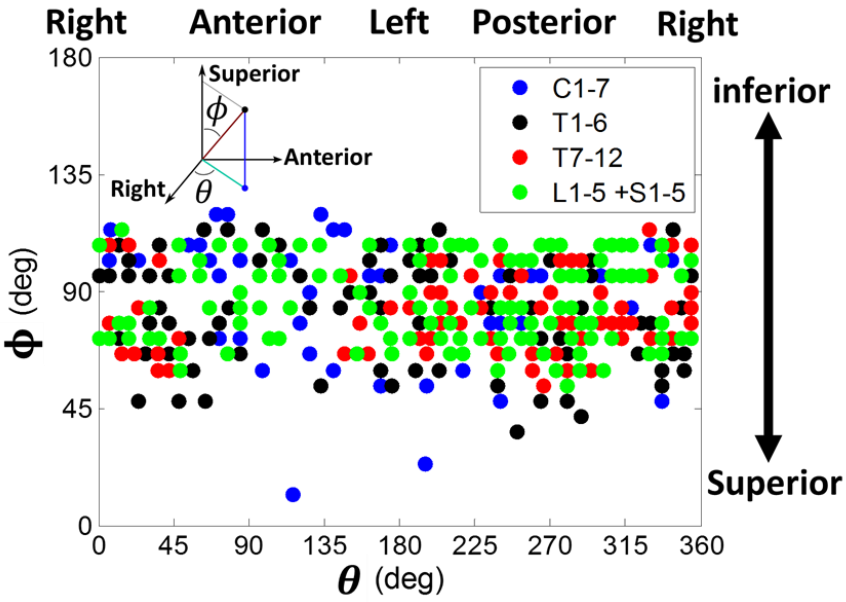

Figure 3-21: Beam angle distribution of all isocentric 4π cases, with angles colored based on PTV location.

3.3.4 Discussion

Sparing of spinal cord and other critical organs including esophagus is the major challenge in SBRT and SRS to spinal lesions. Conventional radiotherapy methods overwhelmingly reply on coplanar beams that result in high dose spillage in this plane and difficulty to spare organs later or A/P to the target. In theory, utilizing non-coplanar beams can shift some of the high dose spill away and then reduce dose to adjacent organs. However, this has not been previously demonstrated due to three challenges. First, non-coplanar beams for body lesions were considered impractical due to mechanical limitations of C-arm gantries that many angles are at risk of collision. Second, there was not an automated beam orientation algorithm to select collision free beams. Third, the feasibility of such non-coplanar beam spine SBRT and SRS has not been demonstrated. We showed that these challenges are not insurmountable.

Possible collisions between the gantry, couch, and patient can be accurately modeled using 3D camera and existing CAD model[62]. The non-coplanar beams can be selected using a column generation algorithm, the resultant IMRT plan can be imported into a clinical planning system for recalculation, validation and safe delivery without modifying existing treatment machines or software. At UCLA, three spine patients have been treated using this method.

It is potentially rewarding to overcome these challenges. With 4π radiotherapy, substantial sparing with average dose reductions of 14.37% and 12.03% of the mean dose and maximum dose relative to the prescription dose was achieved regardless of the inclusion of beam angles requiring extended source to target distances. These percentages translate

to a 2.4 Gy and 2.8 Gy decrease in the maximum dose and mean dose for a single fraction 20 Gy delivery. Maximum dose sparing of 35% was demonstrated for a 3 Gy × 10 case, which is equivalent to a maximum dose reduction of 10.5 Gy compared with the original VMAT clinical plan with 2 arcs. For tumors within the lower thoracic, lumbar and sacral regions, the sparing the *Cauda Equina* was also significant (average 15% reduction from the prescription dose for both mean and maximum doses). The esophagus is also a crucial OAR in stereotactic spine radiotherapy due to its proximity to the target, as demonstrated in Figure 3-20, as well as the risk of radiation-induced stenosis and fistula, if overdosed. As evident from our results, percent dose sparing of 20% and 8.2% to the maximum and mean dose was also achieved for the esophagus. Such remarkable OAR sparing results indicate increased PTV coverage or even dose escalation could be safely implemented with 4π.

Based on the spinal section analysis and results of the isocentric 4π plans shown in Table 3-10, it is apparent that the spinal cord sparing power of 4π is particularly more substantial for treatment to lesions in the thoracic segment, the spinal section in which 60-80% of vertebral lesions occur[158]. For the cervical section, only the spinal cord mean dose reduction was statistically significant. For the lumbar and sacral section, the *Cauda Equina* mean dose, bowl maximum and mean dose, and left kidney mean dose attained $p<0.05$.

As demonstrated by the beam angle distribution shown in Figure 6, the 4π beam angle selection is highly patient-specific. No apparent beam angle clusters were observed for each studied spinal section for general recommendation of beam angles to be made based on the PTV location.

The potential of PTV dose escalation will be quantified in a future study by performing plan normalization up to the maximum prescription dose level that achieve biological effective dose (BED) that is equivalent to the treated clinical plan.

3.3.5 Conclusion

Non-coplanar 4π radiotherapy significantly improves stereotactic spine treatment dosimetry. The clinical feasibility is supported by that isocentric 4π is sufficient to achieve the dosimetric gain. The successful implementation of 4π using an FDA approved planning system (Eclipse) paves the way for prospective clinical trial that can aid in improving local tumor and pain control, and provide treatment to patients that would not otherwise be treated due to strict normal organ dose tolerances.

4 ADVANCING GBM RECURRENCE DETECTION AND TIME PREDICTION WITH RADIOMICS

4.1 Advancing GBM recurrence volume detection with longitudinal Radiomics classification

4.1.1 Introduction

Glioblastoma Multiforme is a devastating disease with nearly 100% mortality. Local disease recurrence after adjuvant chemoradiation is almost inevitable. Due to the aggressive and often short relapse from one recurrence to another, frequent MRI follow-up became standard of practice for these patients. Radiomics have been shown promising in predicting or stratifying based on treatment outcome, tumor extent, and disease histology for GBM patients. The goal of this study is to attempt to utilize Radiomics texture analysis techniques to advance detection of recurrence in order to provide earlier radiotherapy intervention. In addition to the ability to be aware of disease recurrence at an earlier time, advanced detection of the recurrence could also allow for effective treatment with a smaller irradiation volume due to the relatively smaller tumor size at an earlier time point. With a small PTV, more substantial escalation in dose could be achievable, which in turn could further improve disease control. With the abundance of MRI follow-up imaging data, our goal is to utilize

voxel-based image textures to generate an interpatient generalizable recurrence classification model.

4.1.2 Methods

4.1.2.1 Patient characteristics and data summary

Eighteen GBM patients treated at UCLA with a history of recurrence was selected for the study. MRI follow-up images of all time points between the first available after surgery up to the first disease recurrence that contained T1 pre and post-contrast, T2, Flair, and ADC images obtained at UCLA were collected.

4.1.2.2 Image preprocessing

Rigid image registration was first performed within each time point to spatially correlate the images from the T1 pre and post contrast, T2, and Flair images using *Elastix*[159]. At each time point, the image containing the best in-plane resolution was utilized as the fixed image in registration. As the acquired ADC images are often noisier but are directly associated with the Flair images, the ADC image was directly translated to the established image domain within each time point using the obtained rigid transformation for the Flair image to avoid potential registration error.

Unlike computed tomography, a major difficulty in MRI image processing has been that the acquired image intensities do not have a fixed tissue-specific numeric meaning such that wide image intensity variations can be observed even with the same MRI protocol, machine, and patient. Therefore, modality specific image intensity normalization was performed to ensure consistent image intensity values throughout all time points and

different patients. A histogram-based normalization technique was adopted for this study[160,161]. To establish normalization on only the brain volume, and to eliminate the higher image intensity inconsistencies from the skull region, skull stripping was performed prior to image normalization with the Statistical Parametric Mapping (SPM12) toolbox. A standard image template was first chosen for each modality, all images were then mapped to the standard scale by two separate linear mappings, (S_{1i}, μ_i) to $(LIR\,, \mu_s)$ and (μ_i, S_{2i}) to (μ_s, HIR), as demonstrated in Figure 4-1. HIR and LIR are defined as the value at the maximum and minimum 10% of data within the volume of interest on the standard image template. S_{1i} and S_{2i} are the same values corresponding to the input image to be normalized. μ_s and μ_i are the mean image intensity of the standard image and the input image. (m_1, m_2) and (m_1', m_2') are the minimum and maximum values of the input and standard images.

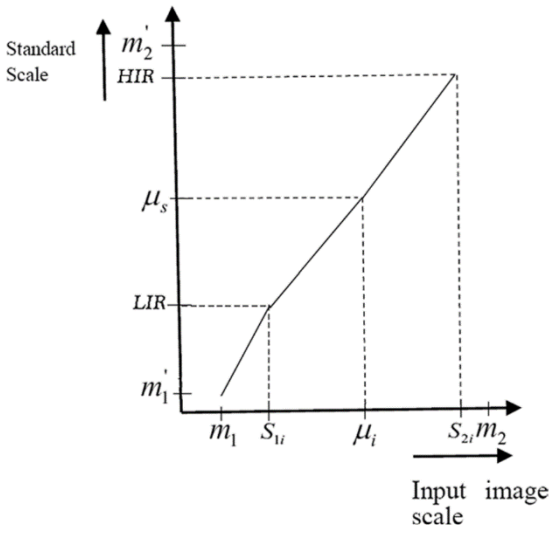

Figure 4-1: Image intensity normalization scheme. Two separate linear mappings from $(\boldsymbol{S_{1i}, \mu_i})$ to $(\boldsymbol{LIR}\,, \boldsymbol{\mu_s})$ and $(\boldsymbol{\mu_i, S_{2i}})$ to $(\boldsymbol{\mu_s, HIR})$.

The image normalization function, indicated as $N(x, y, z)$, and calculated for based on the input image $I(x, y, z)$, is demonstrated in Equation 4-1 below.

$$N(x,y,z) = \begin{cases} \mu_s + (I(x,y,z) - \mu_i)\dfrac{LIR - \mu_s}{S_{1i} - \mu_i}, & m_1' \le I(x,y,z) \le \mu_i \\ \mu_s + (I(x,y,z) - \mu_i)\dfrac{HIR - \mu_s}{S_{2i} - \mu_i}, & \mu_i \le I(x,y,z) \le m_2' \end{cases}$$

Equation 4-1

All images were resampled to an isotropic voxel resolution of 0.9375 mm, the most common inherent in-plane resolution in the dataset. Texture calculation on the same resolution images ensures that the textures are generated from same size local neighborhood and their potential physical meaning will not be confounded by voxel size differences.

4.1.2.3 Image texture generation

3D image textures corresponding to each voxel within the brain volume were extracted from gray level co-occurrence matrices (GLCM)[162] with 64 binned intensities generated from 5 × 5 × 5 local voxel neighborhoods. Common binning ranges were established for each image modality with all images across all time points and patients for further intensity standardization. Twenty four GLCM image textures, along with the histogram-normalized image intensity value were extracted for each modality, totalling 125 image texture values for each voxel. All utilized GLCM textures are listed in Table 4-1 below[55,162-164].

Energy	Homogeneity	Inverse difference moment normalized
Contrast	Autocorrelation	Inverse difference normalized
Entropy	Cluster Prominence	Inverse Variance
Homogeneity	Cluster Shade	Maximum Probability
Correlation	Cluster Tendency	Sum Average 2
Sum Average	Difference Entropy	Sum Entropy
Variance 1	Informational measure of correlation 1	Sum Variance
Dissimilarity	Informational measure of correlation 2	Variance 2

Table 4-1: List of utilized GLCM textures. Texture definition obtained from references[55,162-164].

4.1.2.4 Recurrence classification model generation

4.1.2.4.1 Training contour generation and texture value standardization

To generate a recurrence classification model, regions with recurrence and corresponding control contours with no recurrence were generated for each patient. The recurrence volume were manually contoured on the T1 post contrast or Flair image of the clinically diagnosed recurrence time point with help from an expert physician. For each recurrence volume, two other control volumes the same size as the contoured recurrence volume were generated. The first control contour is a volume that is directly adjacent to the identified recurrence volume, which was utilized as negative volume in recurrence classification model training. The second control contour represents a healthy brain region on the direct opposite side of the brain, used for texture intensity normalization with the assumption that average texture value within a normal brain region would remain similar across all time points and patients. Both control volumes were generated by directly translating the recurrence contours to the area of interest to ensure the data size generated from all contours are on the same scale. Cavity regions were identified for all patients by performing thresholding on the normalized and binned T1 post contrast image, and removed from all training contour regions.

Texture values of all time points and texture values across the entire patient cohort were standardized with Z-score normalization prior to training and classification. All texture values were centered at the mean value of each texture obtained from the transferred remote control volume on the opposite side of the brain. The standard deviation utilized for Z-score normalization was that of the entire calculated brain volume specific to each time point, texture, and patient.

4.1.2.4.2 Feature selection

To avoid model over-fitting and reduction in model generality due to high data dimensionality, feature selection was be performed prior to training. Minimal redundancy maximal relevance criterion (mRMR), a method that evaluates features based on their relevance with the class labels and penalizes the feature redundancy[165], was utilized. The mRMR feature scoring criterion is shown in Equation 4-2 below,

$$mRMR(X_k) = I(X_k; Y) - \frac{1}{S}\sum_{X_j \in S} I(X_k; X_j),$$

Equation 4-2

where Y represents the classification labels, X is the set of features, X_k is the feature to be evaluated, S is the set of already selected features, and the function in the form of $I(A; B)$ indicates the mutual information between parameters A and B, defined in Equation 4-3 below.

$$I(A; B) = \sum_{b \in B}\sum_{a \in A} p(a, b) \log\left(\frac{p(a, b)}{p(a)p(b)}\right),$$

Equation 4-3

with $p(a)$, $p(b)$, and $p(a, b)$ representing the probability density functions of a, b, and their mutual information. The technique was implemented with an open source MATLAB code library for feature selection[166]. The top thirty features were utilized in model training.

4.1.2.4.3 Classification model training and validation

With the selected features, classification model training was be performed on a randomly selected training cohort of ten patients with support vector machine (SVM) [167], formulated as the primal-dual optimization problem shown in Equation 4-4.

Primal		Dual	
$\min_{w,b,\xi}$	$\frac{1}{2}\|w\| + C\sum_{i=1}^{m}\xi_i$	$\min_{\alpha}$	$\frac{1}{2}\alpha^T Q\alpha - \sum_{i=1}^{m}\alpha_i$
$subject\ to$	$y_i(w^T\phi(x_i) + b) \geq 1 - \xi_i$ $\xi_i \geq 0, \quad i = 1, \dots, m$	$subject\ to$	$y^T\alpha = 0$ $0 \leq \alpha_i \leq C, \quad i = 1, \dots, m,$

Equation 4-4

where $x_i \in R^n$ are vectors representing the n selected features corresponding to all m voxels within training, and $y \in R^m$ is an indicator vector defining the recurrence status of each voxel such that $y_i \in \{-1, 1\}$. The features are mapped into a higher dimensional space by the kernel function ϕ for improved classification performance. ξ_i are slack variables in the optimization, allowing for a soft margin in the separation of classes, and are regularized by C. In the dual problem, $Q_{ij} = y_i y_j K(x_i, x_j)$, and $K(x_i, x_j) = \phi(x_i)^T\phi(x_j)$ is the kernel function. By solving the dual problem, the resultant classification decision function $D(x)$ is defined as:

$$D(x_i) = sgn(\sum_{j=1}^{m} y_i\alpha_i K(x_i, x_j) + b)$$

$$K(x_i, x_j) = \exp\{-\frac{\|x_i - x_j\|^2}{2\sigma^2}\}$$

Equation 4-5

The problem was solved using LIBSVM[168], an open source software tool for SVM classification. The model generation workflow is demonstrated in Figure 4-2. The selected feature vectors corresponding to the validation cohort of eight patients was inputted into the classification model created with the training cohort, and the classification results was compared with the ground truth classification status for inter-patient classification performance evaluation.

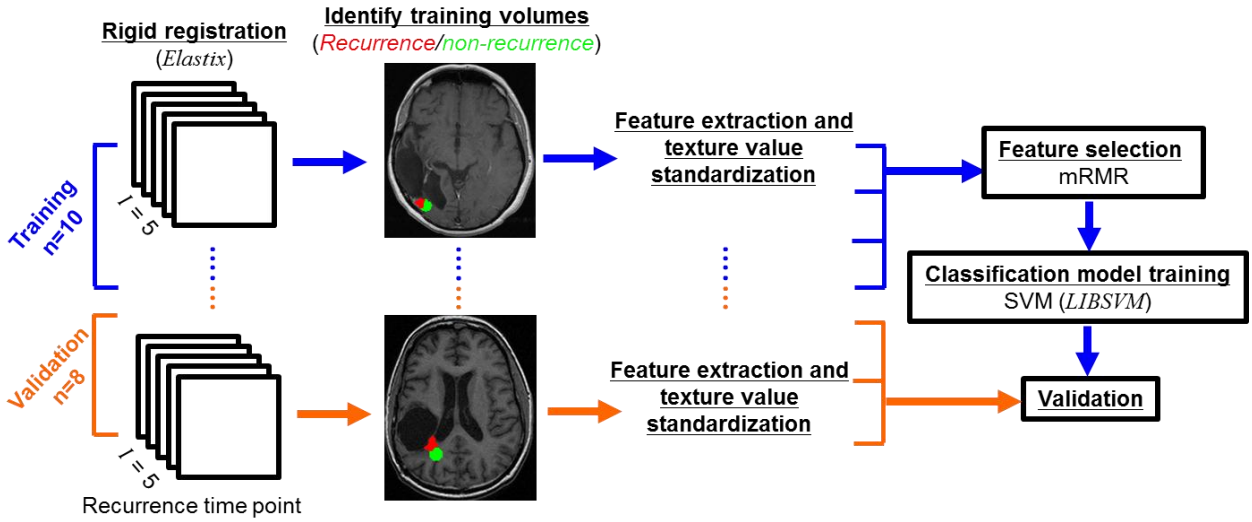

Figure 4-2: Inter-patient general model training workflow

4.1.2.5 Patient-specific recurrence detection and validation

With the generated inter-patient classification model, the follow-up time points prior to recurrence can be classified for all patients in hopes for earlier recurrence detection. Classification was carried out on volumes in the vicinity of the eventual recurrence, and verification was performed on the generated distant control contour. The recurrence and validation volumes defined at the confirmed recurrence time point was transferred to all time prior time points via deformable image registration with the recurrence image as the moving image in registration, performed with *Elastix*[159]. The classification search regions were 2 cm expansions of the transferred recurrence volume at all time points. Through thresholding, irrelevant volumes such as fluid-filled surgical cavities were identified and removed from the classification search and validation regions. The workflow for patient specific classification is shown Figure 4-3. The positive volumes within the classification search regions were obtained and an increasing trend over time is expected.

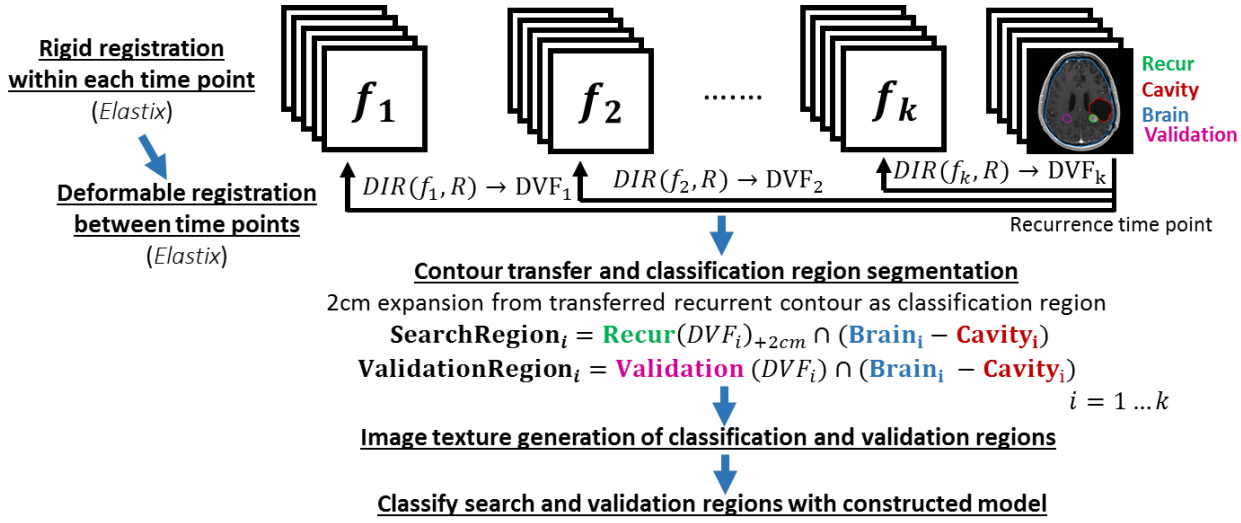

Figure 4-3: Patient-specific recurrence classification and validation workflow

4.1.3 Results

4.1.3.1 Recurrence classification model generation

The top 30 features obtained from mRMR feature selection contained features from all five image modalities. Utilized data size for the training and validation cohort is shown below in Table 4-2. The top five features were T1 Variance, T1 post-contrast Inverse Variance, T1 Inverse Difference Moment Normalized, ADC Inverse Difference Moment Normalized, and T2 first order image intensity. Information on the utilized data and the classification results are shown in Table 4-2. The corresponding ROC curve is shown in Figure 4-4. The reasonable model performance indicated inter-patient generalizability in distinguishing recurrence from non-recurrence at the recurrence time point with the implemented machine learning method.

	Training Cohort (n=10)		Validation cohort (n = 8)	
	Recurrence	**Non-Recurrence**	**Recurrence**	**Non-Recurrence**
Voxel #	79698	68571	31406	22434
Percentage	53.8%	46.2%	58.3%	41.7%
SVM Model Classification Result				
Accuracy	91.34%		72.81%	
Sensitivity	91.39%		77.75%	
Specificity	91.31%		69.28%	

Table 4-2: Data size of training and validation cohorts. Breakdown of recurrence and non-recurrence data size and classification results.

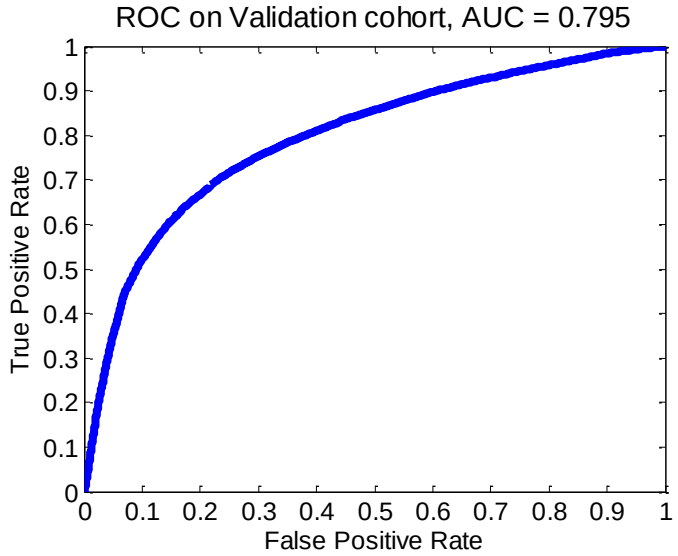

Figure 4-4: ROC curve of classification on the validation cohort.

4.1.3.2 Patient-specific longitudinal recurrence classification in follow-up imaging

The constructed SVM model was utilized to classify the five latest time points prior to the recurrence time point for all patients in hopes to achieve advanced detection of recurrence. The progression of classified recurrence volume over time within the defined search region for all patients are shown in Figure 4-5. Each curve represents the volume progression for one patient and all volumes were normalized to the classified volume size detected at the recurrence time point for visualization on an equivalent scale.

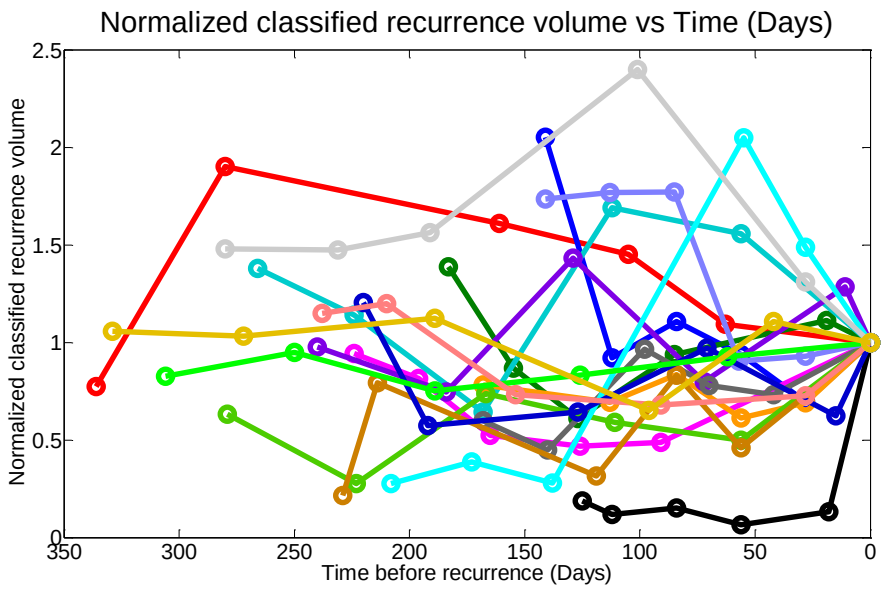

Figure 4-5: Classified recurrence volume within search region over time for all patients. Volumes normalized relative to the volume detected at the recurrence time point.

As evident from Figure 4-5, oscillatory behaviour was observed in the progression of classified recurrence volume throughout the patient cohort, instead of the steady increase that was initially expected. Visualization of classification results from one patient is shown in Figure 4-6, where the model classification region is labelled in blue, volumes classified as recurrence shown in red, and volume classified as recurrence within the remote control search region shown in green (false positives). The recurrence volume progression for the patient case shown in Figure 4-6 corresponds to the black curve in Figure 4-5, in which a slight decrease from the first available time point, followed a sudden increase from the 5th to the recurrence time point can be observed. As specified by white arrows, one region is consistently classified as recurrence, indicating some degree of longitudinal consistency over time. However, the remaining regions that were classified do not appear to remain consistent throughout all time points. Increase in noisy specks is observed in time point 3, and interestingly corresponded to an increase in false positives. This result indicates that the inconsistency in classification volume size could be associated with the image

standardization process. With the consistently detected region connected to the tumor volume that suddenly appeared in the final time point, one could interpret this as an early finding of possible tumor that was in the process of migrating to the final tumor location. However, the existence of surrounding noise renders such speculations inconclusive. More rigorous studies will be needed to study the effect the current image standardization method has on the classification result to further eliminate false positive classifications.

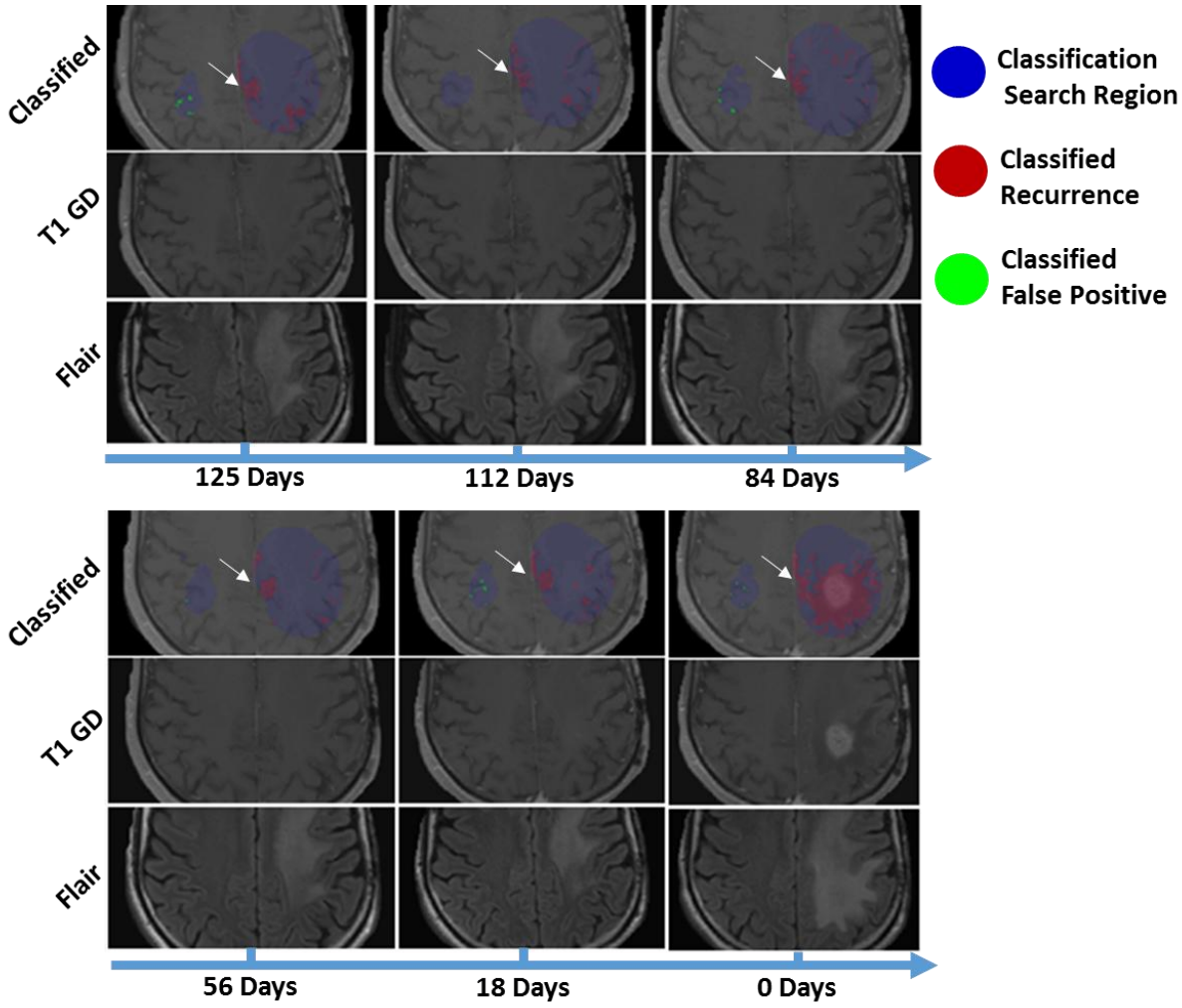

Figure 4-6: Classification results (top) from all six time points with corresponding T1 post-gadolinium contrast (center) and Flair (bottom) images, labeled with days from recurrence. White arrows indicate the region that is consistently classified as recurrence for all time points

4.1.4 Discussion

Radiomics have generally been utilized to establish correlations between image textures obtained from all voxels within a tumor volume to clinical indicators such as patient overall survival, histology and tumor extent. The goal of this study was to classify recurrence on a per-voxel level on a longitudinal time scale. The study result has shown that the classification performance of the proposed method is sensitive to differences in the resultant texture values in the longitudinal time scale. The utilized image normalization method was shown effective for the other purposes such as brain segmentation, but might need to be more stringent for image texture analysis purposes due to the larger dependence on absolute image intensity. The imaging data utilized was also acquired from many different scanners, with differing in-plane resolution and slice thickness. Despite the fact that image histogram matching was performed after voxel resolution standardization, the resampling process still could have confounded the resultant texture values. It might be essential to perform classification training only with textures that are insensitive to the aforementioned unavoidable variations within the data.

In addition, one of the major drawbacks of the proposed method could be that the classification model was established based on recurrence voxels that are readily visible on the images. In order to detect abnormalities prior to those already visible, the training model could need to be established on the time point prior to the tumor being visible.

The abundance of MRI follow-up imaging for GBM patients is an extremely valuable resource for us to further understanding ways to advance the detection of disease recurrence. Methodologies that are not as sensitive to image intensity changes, and with

larger local neighborhoods, might achieve more robust longitudinal classification performance. A sensitivity analysis on parameters such as the texture generation local neighborhood size and number of intensity bins for GLCM calculation could also help produce more robust classification results.

4.1.5 Conclusion

The proposed method in advancing GBM recurrence detection with image texture analysis and machine learning was shown unsuccessful at its current scope. Further studies are needed to understand the classification inconsistencies in between longitudinal time points.

4.2 Predicting time to Glioblastoma Multiforme (GBM) recurrence with MR image texture analysis

4.2.1 Introduction

An additional study was performed to evaluate whether image texture features immediately after surgery could predict time to recurrence. If a prediction model can be built based on the generated image features, the accurate prediction of time to recurrence could guide clinicians in understanding the aggressiveness of the disease and personalizing patient care.

4.2.2 Methods

After performing the same image preprocessing procedures as described in section 4.1.2.2 for the earliest images associated with the earliest available time point, 24 Gray-level

co-occurrence matrix (GLCM) texture features (as listed in Table 4-1), along with the histogram-normalized image intensity values for each modality within a 2 cm expansion of the original tumor volume was generated, resulting in 125 textures features for each patient. The recurrence progression of the patient cohort is shown in Figure 4-7.

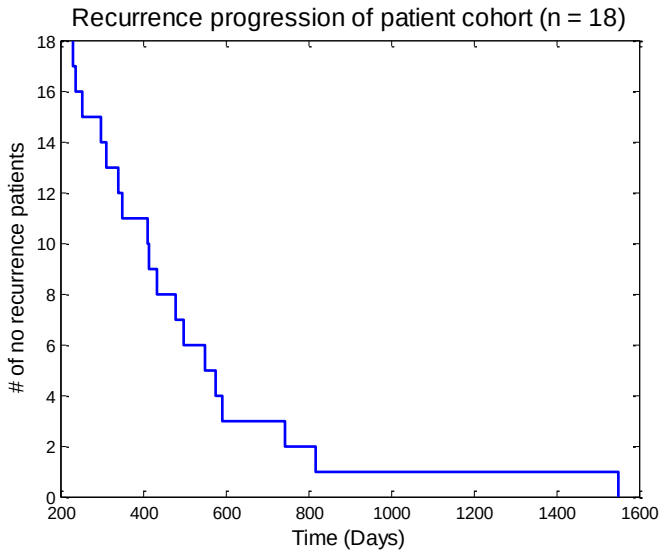

Figure 4-7: Recurrence progression of the utilized patient cohort (n = 18).

To generate a texture model correlating texture features and the time to recurrence with good accuracy, a model with five features was constructed by performing leave-one-out (LOO) least absolute shrinkage and selection operator (LASSO) regression analysis. The formulation of the LASSO regression problem is shown in Equation 4-6 below.

$$\text{minimize} \quad \frac{1}{2}\|\mathrm{Ax}-\mathrm{b}\|_2^2+\gamma\|\mathrm{x}\|_1$$

$$\text{subject to} \quad \mathrm{x}\geq 0,$$

Equation 4-6

with $A = [T\ 1]$, $T_{i,j}$ = ith texture value of the jth patient, b representing a vector containing the time to recurrence for all 18 patients, and γ as a regularization coefficient inducing sparsity in x. γ was tuned until five features were selected. With the selected five features, a polishing optimization without L1 regularization ($\gamma = 0$) was performed to obtain final LOO

models. The predictive power of the resultant models were then evaluated with the correlation-of-determination metric (R^2).

4.2.3 Results

All except one LOO-LASSO regression model selected the identical 5 features, namely, T1 post-contrast cluster shade, T1 pre-contrast cluster prominence, T2 entropy, Flair cluster prominence, and ADC entropy, as demonstrated in Figure 4-8. The average R^2 values of all models were 0.71, and ranged from 0.679-0.891. The correlation between each of the commonly selected texture features and day to recurrence values for all patients is shown in Figure 4-9. A distinct set of textures were selected, corresponding to a significantly lower R^2 value of 0.538, when one patient with particularly long time to recurrence of 1551 days was left out, as demonstrated in Figure 4-10. This result further infers the potential in predicting time to recurrence with image texture features within the vicinity of the original tumor volume.

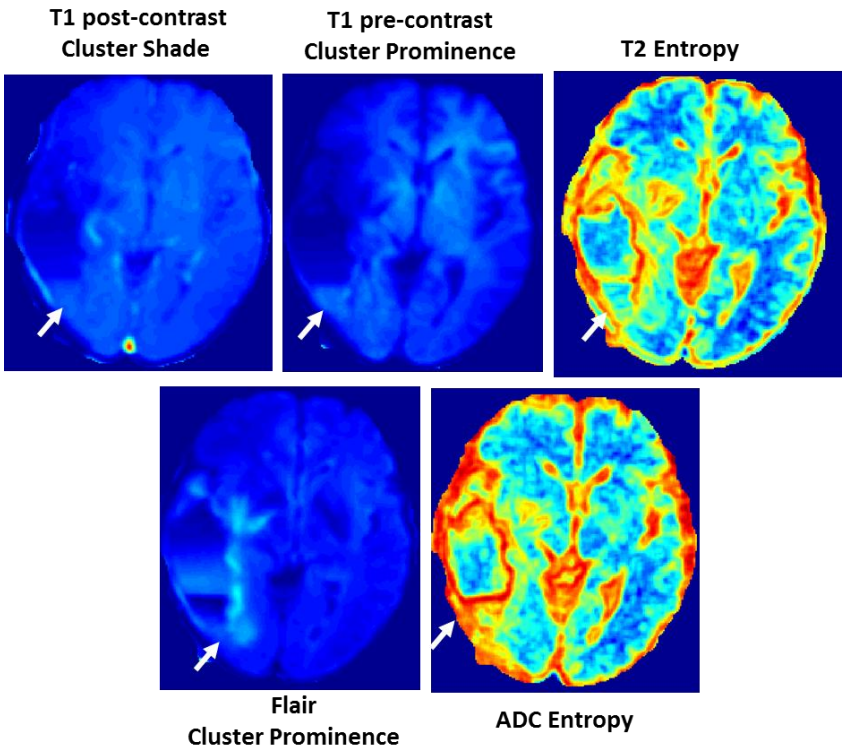

Figure 4-8: Common features selected by all except one LOO-LASSO regression. Arrow indicates region at which the average texture values are taken.

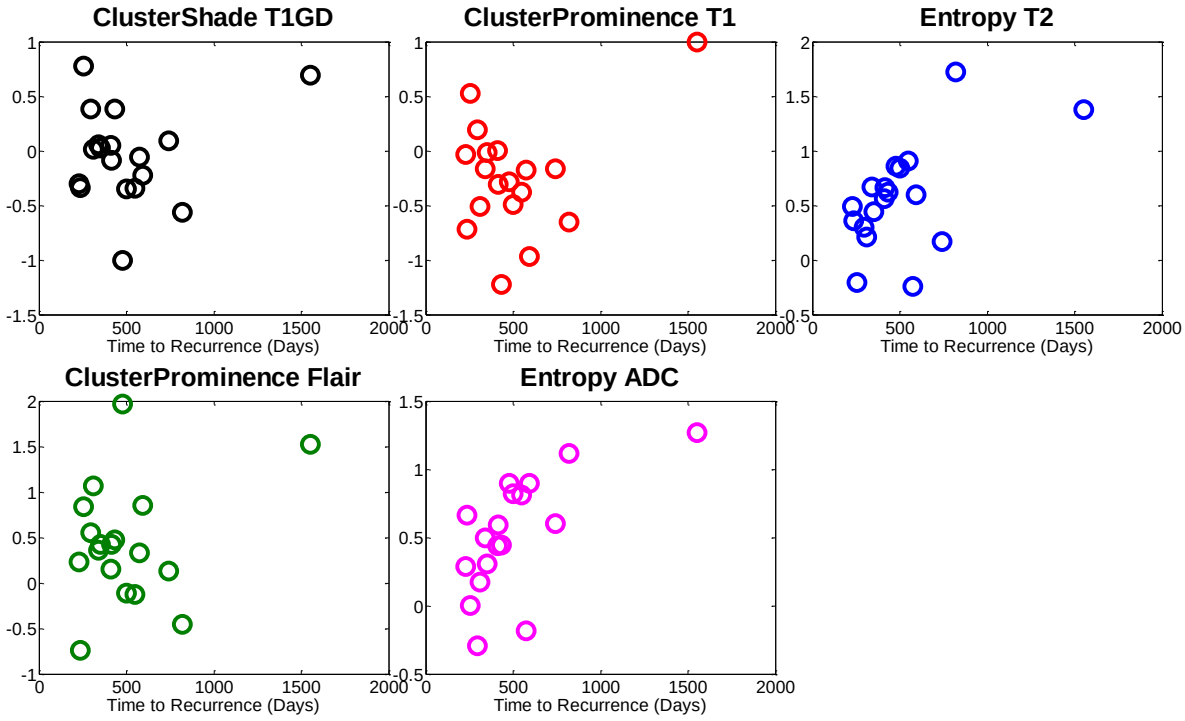

Figure 4-9: Commonly selected features and their individual correlation with time to recurrence.

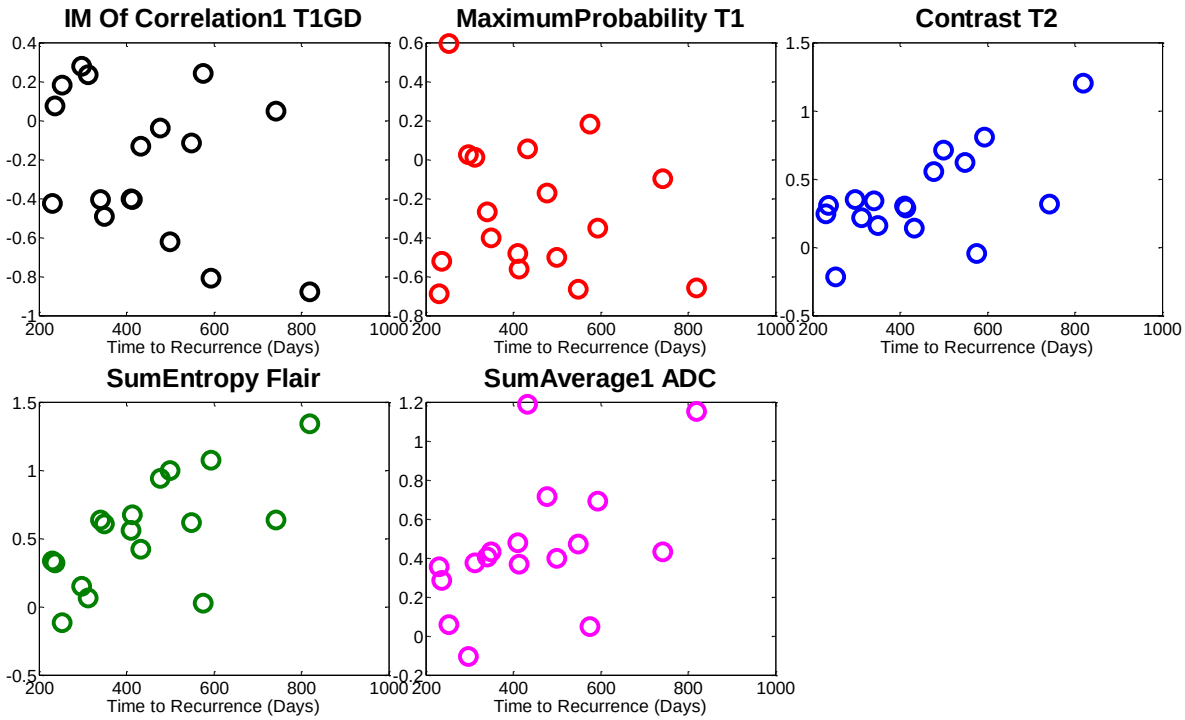

Figure 4-10: Distinct set of features selected when the slowest recurring patient is left out. $R^2 = 0.539$

4.2.4 Discussion and Conclusion

The texture values generated for this study represent the average of texture values from a large volume in comparison with the smaller local neighborhoods utilized in the previous study. The lower sensitivity to noise made the correlation between day to recurrence and texture value clear for some of the features. Even with a lower R^2 that resulted from leaving out the patient with the slowest relapse, correlation between the selected texture values and time to recurrence can still be visually identified. These results suggest texture analysis on a larger region might also aid in identifying recurrent disease that is occurring but not yet visible. With preliminary analysis, the potential in predicting time to first recurrence with post-surgical texture features was demonstrated. Expansion of the patient cohort will be needed for further validation.

5 PERSONALIZED 4Π RADIOTHERAPY, BIOLOGICAL MODELING, AND FRACTIONATION SCHEDULE OPTIMIZATION

5.1 Introduction

In this chapter, we combine the previously introduced methodologies that are potentially capable of further improving GBM disease outcome, including 4π radiotherapy, and dose fractionation optimization with a biological model that reflects the definitive treatment failure of GBM, on identified tumor sub-volumes in which eventual recurrence will occur. With the original plan of identifying such subvolumes through serial MR image texture analysis shown unsuccessful at its current scope, we instead utilized the ground truth eventual recurrence volumes on a patient-specific basis as regions with higher tumor proliferation/aggressiveness and studied the compound effect in outcome improvement with 4π radiotherapy simultaneous integrated boost (SIB) on these volumes in conjunction with dose fractionation optimization. Aside from achieving the optimal spatial dose distribution with 4π radiotherapy, the problem is further expanded to identify a maximum deliverable dose to the SIB volume through a novel convex optimization formulation. With

the developed biological model, known disease characteristics, and patient anatomy, a personalized framework is established to study the benefit of integrating the aforementioned methods across different patients.

5.2 Methods

5.2.1 Patient characteristics and boost volume generation

Seven GBM patients with data available from the first radiotherapy plan for the primary disease up to the MRI imaging acquired at the clinically diagnosed first recurrence time point were selected for this study. The patient characteristics, time to first disease recurrence, information on the delivered clinical plan such as fractionation scheme, mean dose to the normal brain outside of the PTV (D_{mean}), and the PTV size, are tabulated in Table 5-1.

To realistically simulate patient-specific hypothetical volumes with higher tumor proliferation and aggressiveness, the locations at which the eventual disease recurrence occur were utilized. Recurrence volumes were contoured on the MR images obtained on the clinically diagnosed first recurrence date, and transferred to the initial treatment planning CT image through rigid image registration in MIM 6.6.5 (MIM Software Inc., Cleveland, OH). The boost volume was then generated by performing a 3 mm isotropic expansion around the propagated recurrence contour. The volume of the generated boost regions, the non-boost region (original PTV that does not overlap with the generated boost volume), are shown in Table 5-1. All recurrences were in proximity with the originally irradiated PTV. The status of whether the boost region was completely within the original PTV, or residing on the edge of

the original PTV with a partial overlap, is also denoted in the "Overlap Status" column in Table 5-1.

Pt #	Time to 1st recurrence (Days)	Age	Sex	Original clinical plan information			Volumes (cm^3)			Overlap Status
				Fx scheme	Prescription (Gy)	D_{mean}	Original PTV	Boost	Non-Boost	
1	256	50	M	2 Gy x 30	60	32.19	319.06	17.78	309.33	Partial
2	818	39	M	2 Gy x 30	60	29.42	343.55	2.39	341.16	Complete
3	457	52	M	1.8 Gy x 33	59.4	19.02	252.34	2.80	249.54	Complete
4	292	35	M	2 Gy x 30	60	40.30	632.59	7.49	625.10	Complete
5	189	59	M	1.8 Gy x 33	59.4	20.63	430.07	12.23	424.50	Partial
6	713	66	M	2 Gy x 30	60	18.25	119.91	5.52	114.39	Complete
7	1516	54	F	1.8 Gy x 33	59.4	31.92	281.35	6.45	275.99	Partial

Table 5-1: Patient characteristics, original clinical plan information, size of generated boost volume, and whether the generated SIB volume partially or completely overlaps with the original PTV volume.

5.2.2 4π radiotherapy plan generation

With the patient-specific contours of the non-boost PTV, SIB volume, and OARs, our in-house 4π radiotherapy inverse optimization platform[44] was utilized to select the optimal 20 beam orientations that can achieve the original prescription dose (59.4 or 60 Gy) to the non-boost PTV volume, and 110 Gy to the assigned SIB volume for each case. Selected boost dosage of 110 Gy was selected based on a previously tested dose escalation clinical trial[3]. Prior to 4π inverse optimization, dose matrices with 2.5 x 2.5 x 2.5 mm^3 resolution corresponding to each 5 × 5 mm^2 intensity-modulating beamlet for all non-colliding candidate beam orientations were calculated using convolution/superposition of 6 MV poly-energetic X-ray kernels. A column generation algorithm[45] was utilized to iteratively select and optimize beam fluence until the desired 20 beam angles were selected.

The designated boost dosage of 110 Gy is substantially higher than the original prescription dose and is known to be achievable with 4π radiotherapy based on a previous

study[46]. However, we have no knowledge of whether that is indeed the highest achievable boost dose. Therefore, in the following section, we seek to identify the maximum viable boost dose on a patient-specific basis through inverse optimization.

5.2.3 Simultaneous integrated boost (SIB) optimization formulation

The main objective of this optimization problem is to obtain the maximum achievable boost dosage to the SIB volume based on personalized anatomy, while maintaining mean and maximum dose to the normal brain, coverage to the PTV, and minimize dose to surrounding organs-at-risk. The problem formulation is shown in Equation 5-1 below.

$$\underset{x}{argmax} \quad d_{SIB} - \frac{1}{2} w_H \|(A_{SIB}x - d_{SIB})\|_2^2$$

subject to

$$\frac{1}{2}\|(A_{NB}x - d)\|_2^2 + \frac{1}{2} w_{OAR}\|(A_{OAR}x)\|_2^2 \leq \gamma$$
$$1^T A_{\mathrm{Brn}} x \leq n \cdot D_{mean}$$
$$A_{PTV_{95\%}} x \geq d$$
$$A_{\mathrm{Brn_M}} x \leq d \cdot p$$
$$d_{SIB} = \frac{1^T A_{SIB} x}{n_{SIB}}$$
$$x \geq 0$$

Equation 5-1

The optimization variable, x, is a vectorized representation of all beamlet intensities from the 20 beam angles selected from 4π column generation. All variables denoted in the format of A_V represent fluence-to-dose transformation matrices corresponding to the specified volume V. The volume definitions are described in Table 1-1. d represents the original prescription dose.

Volumes	Description
SIB	Defined volume to receive simultaneous integrated boost
PTV_U	The union of the original PTV and the SIB volume
NB	Non-boost PTV volume that does not contain the SIB region
OAR	Union of all organs-at-risk that do not overlap with PTV
Brn	Normal brain volume outside of PTV
Brn_M	Brn $-$ (PTV_U + margin M)
$PTV_{95\%}$	Central 95% of the PTV

Table 5-2: Volume definitions

The first objective function maximizes d_{SIB}, the mean dose received by the SIB volume, which is also defined within the problem constraint. The dose homogeneity within the SIB volume is maintained by the second objective term, with a relative weighting of w_H.

The problem is constrained by six conditions. The first condition maintains the dose of all voxels within NB to be close to the prescription dose d while penalizing the dose received by all organs-at-risk. The summation of the two terms are constrained by γ, defined as the equivalent metric obtained from the 4π plan with fixed SIB prescription dose of 110 Gy. The second condition maintains the mean dose of the normal brain to be below the mean normal brain dose of the clinically delivered plan, where variable n represents the number of voxels within the normal brain volume, and D_{mean} corresponds to the normal brain mean dose of the original clinical plan. The third constraint further ensure PTV coverage within the non-boost PTV volume. The fourth keeps the dose within volume Brn_M under a cut off percentage p of the prescription dose ($0 < p \leq 1$). The fifth constraint defines d_{SIB}, with n_{SIB} representing the number of voxels within the SIB volume. The beamlet intensities, x, are maintained as non-negative with sixth and final constraint. The problem was solved with the Chambolle-Pock algorithm[169] with a linesearch procedure, as detailed in the Appendix.

The resultant mean dose to the SIB volume from the optimization, SIB_{op}, was utilized as a patient-specific boost prescription dose and re-optimized within the original 4π framework with identical OAR dose constraints and weighting parameters as that of the original 4π plans with 110 Gy boost. This additional polishing step enabled OAR-specific constraints to be kept and improved dose homogeneity within the SIB volume. OAR dose statistics of the 4π SIB 110 Gy boost, 4π SIB_{op} boost, and the original clinical plans were calculated and compared.

The customized SIB_{op} values were then utilized to perform patient-specific dose fractionation optimization, as described in the following section.

5.2.4 Patient-specific biological modeling

The previously developed cancer stem cell dynamics ODE model, as described in detail in section 2.2.2.3 and shown in Equation 2-6 was used to model the dynamic interaction between cancer stem cells (CSC) and differentiated cancer cells (DCC) for both the boost and non-boost volumes.

$$\begin{array}{l} \qquad\qquad \text{Self-renewal} \\ \dot{U}(t) = (2P-1)m_U k\big(W(t)\big)U(t) \\ \dot{V}(t) = 2(1-P)m_U k\big(W(t)\big)U(t) + \; m_V k\big(W(t)\big)V(t) - a_V V(t) \\ \qquad\qquad \text{Differentiation from CSC} \qquad \text{DCC growth} \qquad \text{DCC natural cell death} \\ W(t) = U(t) + V(t) \\ k(W) = \max(1 - W^4, 0) \end{array}$$

Equation 5-2

In short, U(t), V(t), and W(t) represent the volume fractions of CSCs, DCCs, and total tumor with respect to a specified volume of interest in which the tumor can grow. P is the probability that one CSC gives rise to two CSC, instead of two DCCs. The growth rates of CSC and DCC are m_U and m_V, and a_V is the natural cell death rate of DCCs. Following previous

publications[40,43], all three parameters were set to $\ln(2)/T_{pot}$ day^{-1}, where T_{pot} represents the tumor potential doubling time of malignant brain tumors[95]. $k(W)$ keeps the total tumor volume fraction in between 0 and 1 while simulating the slowdown in growth rate as new born cells compete for resources within the available growth volume[69]. All simulations in this study were set to have the specified volume of interest to be 10^{11} cells. As patients typically receive radiation thirty days after surgery (range, 3-6 weeks)[109], the ODE was utilized to simulate 30 days of tumor growth with no treatment intervention from the specified initial conditions prior to starting radiation therapy. The recurrence time is defined as the time point at which the total tumor cell number exceeds 2.8×10^9 cells, 1 ml larger than the postoperative mean T1 post-gadolinium enhancement volume of 1.8 ml from 721 patients[108].

Radiation therapy was modeled by halting the ODE prior to each dose fraction and applying LQ killing to each compartment using radiosensitivity parameters obtained from fitting of GBM clonogenic survival data[43]. In addition, based on the evidence of radiation-induced cell reprogramming where DCCs convert back to CSCs after radiation exposure at a rate proportional to the dose received[103,110], a reprogramming term was also incorporated into the cell killing model. The linear quadratic radiation therapy cell killing and reprogramming to both compartments within the boost and non-boost volumes are applied as follows in Equation 2-8:

$$U(t) = U_0 \exp\left\{-\alpha_{CSC}(D)_i - \beta_{CSC}(D)_i{}^2\right\} + cV_0(D)_i \exp\left\{-\alpha_{DCC}(D)_i - \beta_{DCC}(D)_i{}^2\right\}$$
$$V(t) = (1 - c(D)_i)V_0 \exp\left\{-\alpha_{DCC}(D)_i - \beta_{DCC}(D)_i{}^2\right\},$$

Equation 5-3

where U_0 and V_0 are the compartmental cell fractions after halting the ODE at dosing time points, $(D)_i$ represents the radiation delivered to the volume of interest (boost or non-boost) on the ith fraction. c is the reprogramming coefficient that induces a dose dependent

reprogramming on the DCCs that remain after LQ killing. The ODE parameters that remained universal for all patients are shown in Table 5-3.

P	F	α_{CSC}	β_{CSC}	α_{DCC}	β_{DCC}	c
0.51	0.016	0.01	1.77E-07	0.125	0.028	5.196E-03

Table 5-3: Universal parameters for biological modeling**.**

With knowledge of the time to recurrence for each patient, the initial number of viable tumor cells (N_V), and the potential doubling time (T_{pot}) were tuned to achieve the same model prediction in recurrence time after applying the same radiotherapy dose fractionation scheme that the patient had received. During the tuning step, the CSC and DCC populations are assumed to be uniformly distributed throughout the entire PTV_U volume and receiving uniform dose. The model is therefore initialized as follows:

$$U_0 = N_V F, V_0 = (1 - F)N_V,$$

Equation 5-4

where F represents the fraction of CSC out of the all viable tumor cells. The obtained patient-specific models were then utilized to perform dose fractionation optimization.

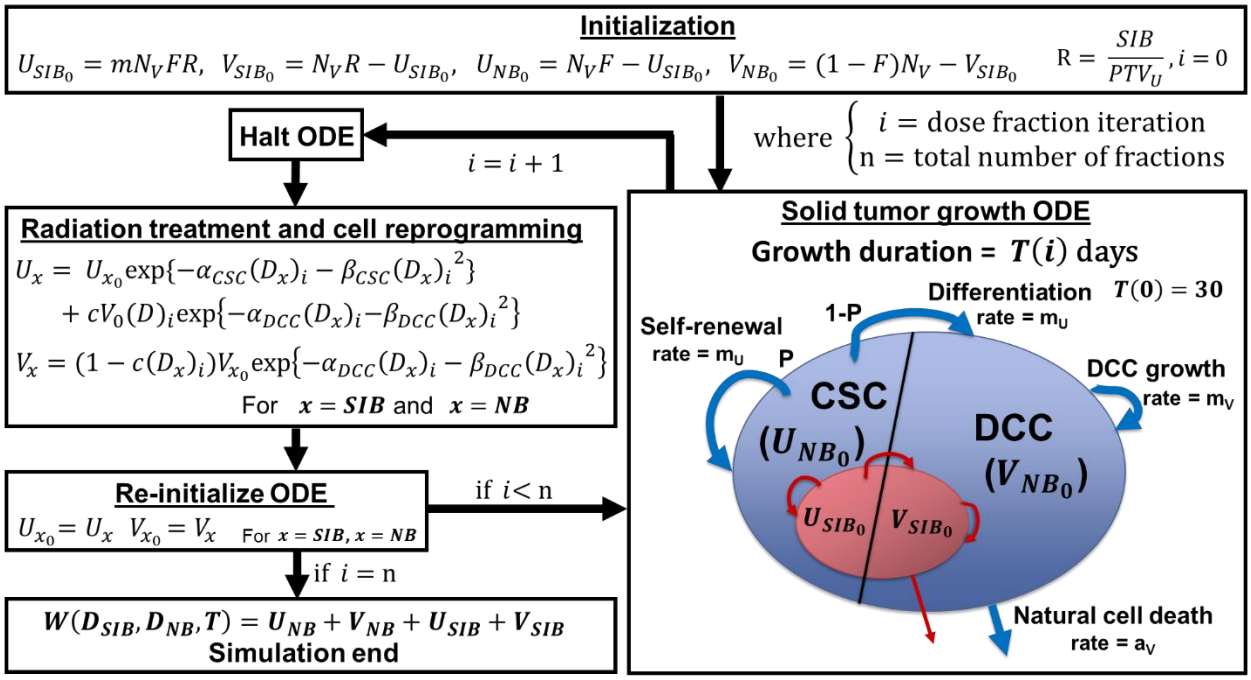

Figure 5-1: Tumor growth ODE and radiation therapy simulation schematic with consideration of boost and non-boost volumes

5.2.5 Dose fractionation optimization with SIB

5.2.5.1 Volume initialization

The goal of this study is to assess the potential benefit in delivering boost dose to regions with higher tumor activity, which in theory could have an enhanced concentration of CSCs. Despite recent breakthroughs in in-vivo imaging of CSC, there is no fixed answer of how high the concentration enhancement would be for each patient. Therefore, a wide range of CSC concentration enhancements within the SIB volume were utilized to demonstrate the potential range of improvement that 4π SIB in conjunction with dose fractionation optimization could provide. The volumes are initialized with definitions shown in Equation 5-5 below.

$$U_{SIB_0} = mN_V FR \qquad U_{NB_0} = N_V F - U_{SIB_0}$$
$$V_{SIB_0} = N_V R - U_{SIB_0} \qquad V_{NB_0} = (1-F)N_V - V_{SIB_0}$$
$$R = \frac{SIB}{PTV_U}$$

Equation 5-5

U_{SIB_0}, V_{SIB_0}, U_{NB_0}, and V_{NB_0} represent the starting number of CSCs and DCCs in the boost and non-boost volumes. F is the fraction of CSC out of the entire viable tumor volume, N_V. m is a CSC concentration enhancement multiplier that increases the CSC concentration within the SIB volume. R represents the volume fraction of boost region out of the PTV_U. This initialization method assumes that the density of N_V is uniform throughout PTV_U. The number of CSCs required to achieve the assigned concentration boost of m within the boost volume is first obtained, the remaining is then filled in with DCCs. The remaining CSC and DCC then populates non-boost region. $m = 1$ is equivalent to initializing with uniform concentrations throughout PTV_U. Dose fractionation optimizations with m of 1, 2, 5, 10, 50, and 100 were calculated in this study. A full schematic of the tumor growth and radiotherapy simulation is shown in Figure 5-1.

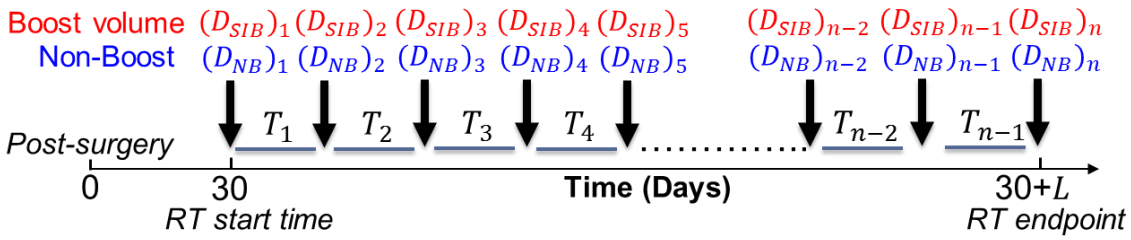

Figure 5-2: Schematic of optimization variables with respect to treatment time

5.2.5.2 Problem formulation

The formulated optimization problem is shown in Equation 5-6 below:

$$\underset{D_{SIB},D_{NB},T}{\text{argmax}} \quad \text{Recurrence Time}(D_{SIB}, D_{NB}, T)$$

$$\text{subject to} \quad \sum_{i=1}^{n} (D_{SIB})_i + \frac{(D_{SIB})_i^{\,2}}{\alpha/\beta} \leq \text{BED}_{SIB}, \quad \sum_{i=1}^{n} (D_{NB})_i + \frac{(D_{NB})_i^{\,2}}{\alpha/\beta} \leq \text{BED}_{NB},$$

$$D_{min} \leq D_{SIB}, D_{NB} \leq D_{max}, \quad \sum_{i=1}^{n-1} T_i = L, \quad L_s \leq \text{T} \leq L, \quad \frac{1}{r} \leq \frac{(D_{SIB})_i}{(D_{NB})_i} \leq r, \quad for\ i = 1..n$$

Equation 5-6

The objective of the optimization is to maximize the recurrence time with optimization variables of interest D_{SIB}, D_{NB}, and T. D_{SIB} and D_{NB} are vectors of length n, with each element $(D_{SIB})_i$ and $(D_{NB})_i$ representing the dose applied to the SIB and non-boost volumes during the ith dose fraction. T is a vector of length n-1, with each element T_i as the time interval between fractions i and i+1.The total treatment duration is specified as L. A schematic of the optimization variables with respect to treatment time is shown in Figure 5-2.

Optimization constraints include total normal tissue biological effective dose (BED) to both volumes (BED_{SIB} and BED_{NB}), fractional dose limits (D_{min} and D_{max}), time interval limits, and ratio constraint (r) between dose delivered to SIB and non-boost to ensure plan deliverability ($r > 1$). The ratio constraint is set to be 10% larger than the case-specific ratio between optimized SIB dose (SIB_{op}) and the original prescription dose obtained. L_s indicates the lower bound of the time intervals, which was set to 1 to ensure at least one full day between all fractions. n and L were set to equal that of the originally delivered dose fractionation schedule. For example, for a conventional once per weekday 2 Gy × 30 scheme, n and L were 30 and 39, respectively. α/β represents the ratio between the linear and quadratic terms within the classic LQ model for surrounding normal brain tissue, which was

set to 3 for all calculations. BED_{NB} was set to be equivalent to the BED that the patient had received from the original dose fractionation scheme, as indicated in Table 5-1. BED_{SIB} was set to be equal to the BED of delivering the total optimized SIB dose as equal dose fractions throughout all the whole treatment course, as demonstrated in Equation 5-7.

$$BED_{SIB} = \frac{SIB_{op}^2}{n \cdot \alpha/\beta} + SIB_{op}$$

Equation 5-7

The optimization problem was solved using a paired simulated annealing algorithm[111], as detailed in section 2.2.2.3 and demonstrated in Figure 5-3. The optimization variables D_{SIB} and D_{NB} were initialized as equal dose fractions, and T was set to represent once every weekday treatments. The simulated annealing parameters and additional universal problem constraint parameters are tabulated in Table 5-4.

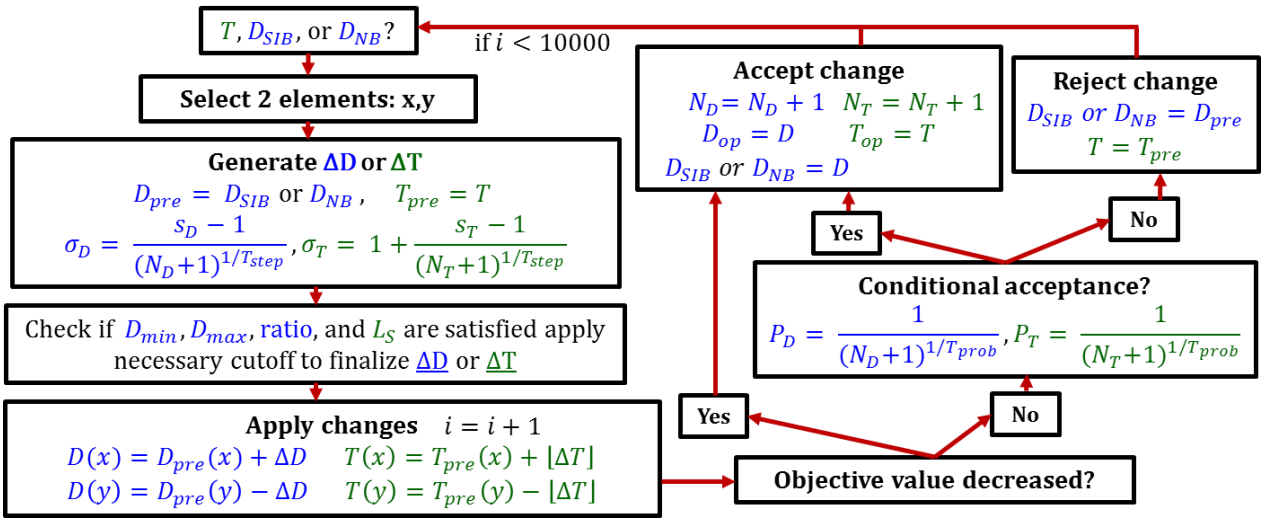

Figure 5-3: Simulated annealing algorithm schematic

Simulated annealing algorithm parameters							Problem constraint parameters			
s_D	s_T	T_{prob}	T_{step}	Decision probabilities			L_s	D_{max}	D_{min}	α/β
				T	D_{SIB}	D_{NB}				
40	15	1	2	0.3	0.35	0.35	1	15	0.5	3

Table 5-4: Optimization parameters

5.3 Results

5.3.1 4π radiotherapy plan generation with fixed boost dose

Global improvement in OAR sparing was observed for all cases even with the substantially higher boost dose prescription of 110 Gy compared with the original clinical plans. The average OAR mean and maximum dose statistics of the boost plans with 110 Gy delivered to the SIB volume are shown in Table 5-5. OARs mean or maximum dose with statistically significant dose reduction based on a one-sided Wilcoxon signed rank test compared with the original clinical plan are indicated with an asterisk (*). All maximum dose values reported are defined as $D_{2\%}$, dose received by at least 2% of the volume. All candidate beamlets within the selected beam angles for each case was used in SIB optimization to identify the maximum achievable boost dose.

Average OAR Dose Statistics (Gy)												
			Brainstem	**Chiasm**	**Cochlea**		**Eye**		**Lens**		**Optic Nerve**	
					L	**R**	**L**	**R**	**L**	**R**	**L**	**R**
4π SIB	**110Gy**	**Mean**	17.96	11.75*	4.46	2.23	1.62*	1.32*	0.87*	0.60*	2.92*	3.72*
		Max	40.84	18.96*	5.97	3.20	3.16*	2.87*	1.09*	0.83*	4.98*	5.45*
	Opt	**Mean**	18.77	12.47*	6.18	1.73	1.59*	1.39*	0.83*	0.72*	3.38*	3.61*
		Max	44.53	19.71*	8.08	2.93	3.09*	2.98*	1.10*	1.06*	5.86*	6.22*
Clinical		**Mean**	27.24	28.71	11.61	5.07	5.11	5.00	3.23	3.17	12.79	10.88
		Max	43.18	37.74	18.54	6.68	9.12	8.53	3.74	3.67	25.35	21.48

Table 5-5: Average OAR dose statistics for the 4π SIB with fixed boost of 110 Gy, patient-specific optimized boost, and original clinical plan. *Statistically significant dose reduction compared with clinical plan, with $p<0.05$ from one-sided Wilcoxon signed rank test.

5.3.2 Simultaneous integrated boost (SIB) optimization

The resultant dose statistics and the utilized optimization parameters for each plan is shown in Table 5-6. The obtained mean dose to the boost volume (SIB_{op}) is used for the dose fractionation optimization. All values are substantially higher than the originally

assigned 110 Gy boost dose, particularly for cases with boost volumes that overlap with the original PTV completely, which all achieved doses greater than 214 Gy. For cases with only partial overlap, the minimum dose to the boost volume was substantially lower as expected due to the need to minimize dose to the immediately abutting normal brain volume. For all generated SIB cases, the normal brain mean dose was maintained significantly lower than or equivalent to that of the original clinical plans (D_{mean}), indicating that the enforced maximum dose constraint to the normal brain volume is the dose limiting factor of this optimization problem instead of the overall mean dose. The resultant average OAR maximum and mean doses are reported in Table 5-5, indicated as "4π SIB Opt". Statistically significant reduction in OAR dose values compared with the original clinical plans was still observed with the optimized boost doses for majority OARs, as indicated by asterisks (*). The only OAR with slightly worsened maximum dose average is the brainstem, which resulted from one case with brainstem partially overlapping with the original PTV volume and abutting the boost volume. As expected, OAR doses from the "4π SIB Opt" plans are higher than that of plans with fixed boost dose of 110 Gy (4π SIB 110 Gy).

Pt #	Normal Brain			Boost volume (SIB)			Non-Boost (NB)		Optimization hyper-parameters				
	Mean dose (Gy)		Max (Gy)	Dose statistics (Gy)			Mean (Gy)	PreD Coverage (%)	Cutoff p	W_{SIB}	W_{OAR}	W_H	Margin M (mm)
	Clinical (D_{mean})	SIB Plan		Mean (SIB_{op})	Max	Min							
1*	32.2	20.8	66.2	124.2	127.6	124.3	70.1	99.9	1	30	1	3	0
2	29.4	26.3	61.1	214.0	219.4	213.4	73.9	99.6	0.7	200	2	3	2.5
3	19.0	15.4	58.5	234.7	239.5	232.8	80.9	99.6	0.7	200	2	10	2.5
4	40.3	32.0	61.8	245.6	250.4	245.3	81.2	98.9	0.9	200	2	20	0
5*	20.6	20.6	65.8	117.3	121.4	117.3	68.6	99.6	1	30	2	2	0
6	18.2	14.9	58.4	228.6	234.4	229.4	101.2	99.9	0.7	200	2	10	2.5
7*	31.9	15.1	55.6	127.0	131.6	127.2	68.5	98.0	1	40	2	3	0

Table 5-6: Case-specific optimization parameters and resultant dose statistics. PreD = prescription dose. Margin M = isotropic expansion radius around PTV_U that was used to generate volume Brn_M utilized as part of the optimization constraint. All maximum dose values are defined as $D_{2\%}$. Patients with SIB only partially overlapping with the original PTV are marked with *.

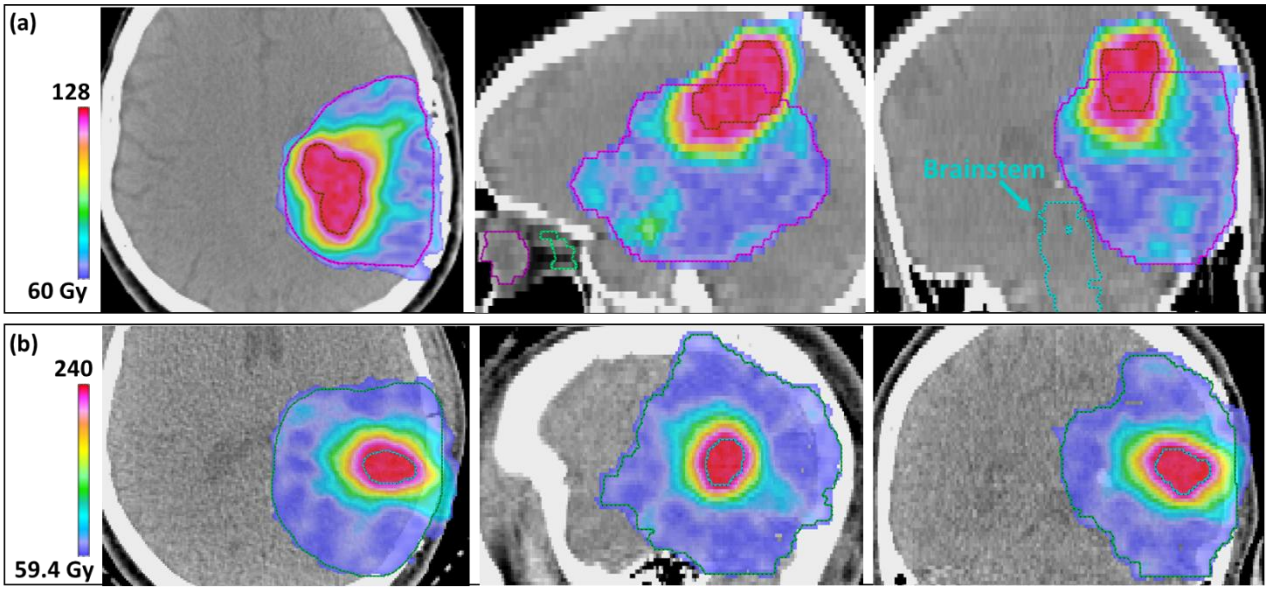

Figure 5-4: SIB example dose wash (a) Case with partial overlap boost (patient 1) (b) Case with complete overlap between boost and original PTV (patient 3)

The resultant dose wash from one case with partial overlap between the boost and original PTV (patient 1) and another with complete overlap (patient 3) are shown in Figure 5-4(a) and Figure 5-4(b). The corresponding DVH comparisons between the generated 4π SIB plans and the original clinical plans of the same two cases are shown in Figure 5-5(a) and Figure 5-5(b). The substantial OAR dose reduction and homogenous dose within the boost volume can be visually seen from both DVHs. For patient 1, the maximum brainstem dose is slightly higher than the original clinical plan due to the partial intersection between the original PTV. For patient 3, substantial reduction for all OARs was achieved even with a boost dose as high as 234.7 Gy. This can be combatted by modifying the problem in the future to have separate weighting values for each OAR instead of a global weighting term, w_{OAR}. The mean values of the non-boost region, as shown in Table 5-6, are maintained close to the original prescription dose despite the substantially larger SIB dose delivered.

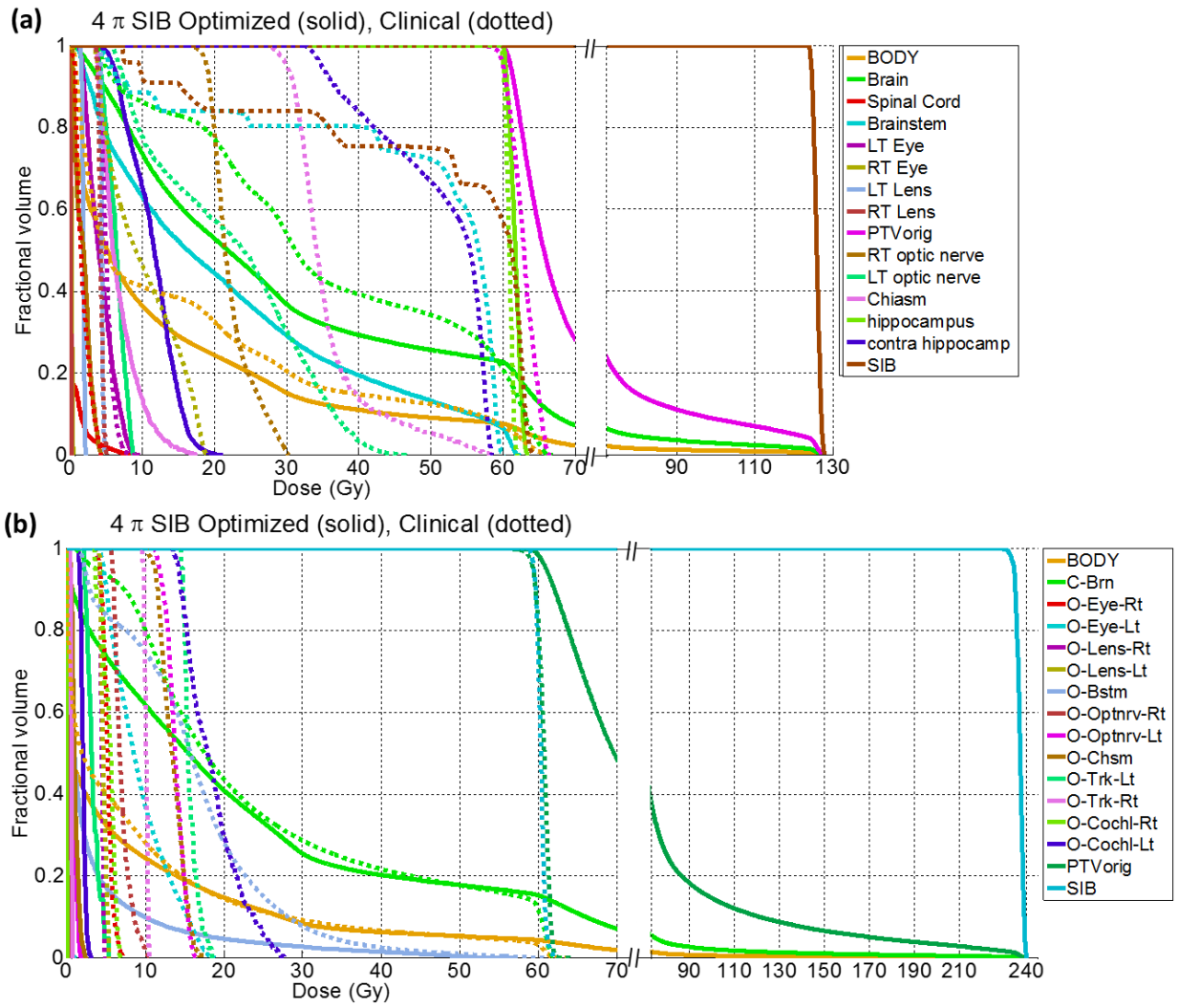

Figure 5-5: DVH comparison between original clinical plan and 4π SIB plans. To better demonstrate the curves for both OARs and the boost volume, two separate scales in dose were utilized for each DVH. (a) Partial boost overlap (patient 1) (b) Complete boost overlap (patient 3)

5.3.3 Patient-specific biological modeling and optimization

The patient-specific number of viable tumor cells (N_V) and potential doubling time (T_{pot}) that were tuned based on the time to recurrence and received dose fractionation scheme for each patient is shown in Table 5-7. The fraction of boost volume within the treated total treated PTV volume (PTV_U), used in the volume initialization demonstrated in

Equation 5-5, and BED_{SIB} and r employed in optimization constraints are also tabulated in Table 5-7. All parameters were used for patient specific dose fractionation optimization.

Pt #	Time to 1st recurrence (Days)	N_V	T_{pot} (Days)	$\frac{SIB}{PTV_U}$ (%)	BED_{SIB} (Gy)	r
1	256	1.79×10^9	3.9	5.44	295.49	2.28
2	818	1.30×10^8	3.9	0.70	722.85	3.92
3	457	5.48×10^8	3.9	1.11	790.94	4.35
4	292	1.41×10^9	3.9	1.18	915.65	4.50
5	189	1.93×10^9	3	2.80	256.39	2.17
6	713	1.96×10^8	3.9	4.60	809.27	4.19
7	1516	6.88×10^7	6	2.28	289.81	2.35

Table 5-7: Patient-specific model and optimization parameters. N_V = number of viable tumor cells at beginning of simulation. T_{pot} = potential doubling time in days. $\frac{SIB}{PTV_U}$ = percentage of boost volume out of the entire treated volume. BED_{SIB} = total dose applied to boost volume. r = utilized ratio constraint between boost and non-boost volumes.

Pt #	TR (Days)	Case specific volume fraction with CSC fraction within boost increased by multiplication factors											
		m = 1		m = 2		m = 5		m = 10		m = 50		m = 100	
		Equal	Opt	Equal	Opt	Equal	Opt	Equal	Opt	Equal	Opt	Equal	Opt
1	256	262.8	367.2	265.4	367.2	273.8	377.1	289.4	403.2	302.8	441.1	302.8	439.0
2	818	820.4	946.0	821.5	944.8	824.7	950.6	830.1	949.3	878.4	1019.8	942.0	1136.3
3	457	460.3	564.7	461.6	564.4	465.7	562.1	472.8	571.2	542.0	690.7	564.9	732.1
4	292	294.3	373.6	295.2	372.6	298.2	373.6	303.2	380.5	353.9	472.1	380.7	534.9
5	189	191.1	262.5	191.9	262.5	194.3	262.1	198.6	266.6	217.4	310.4	217.4	312.5
6	713	728.8	856.0	735.6	855.0	757.4	874.2	799.0	950.2	851.6	1049.0	851.6	1044.6
7	1516	1524.0	1791.7	1527.0	1780.7	1536.0	1771.9	1551.6	1794.0	1625.6	1908.7	1625.6	1905.7

Table 5-8: Forward simulation with equal dose fractions and dose fractionation optimization recurrence time results across various CSC concentrations within boost volume. m = CSC concentration multiplier. TR = time to recurrence. Forward simulation results are labeled as "Equal", optimization results are indicated by "Opt".

Comparisons between recurrence outcome from forward simulations with equal dose fractions treated on conventional per weekday time points (Equal), and optimized dose fractionation with variable time and doses (Opt) across various CSC concentration multipliers (m) are shown in Table 5-8. Dose fractionation optimization resulted in substantial improvements in recurrence for all differing CSC concentration within the boost

region. This benefit is observed even without CSC concentration boost (m=1). The improvement provided by optimization compared with equal dose fractions ranges between 68 - 242 days, and is up to 393 days compared with the original clinical recurrence without boost dose.

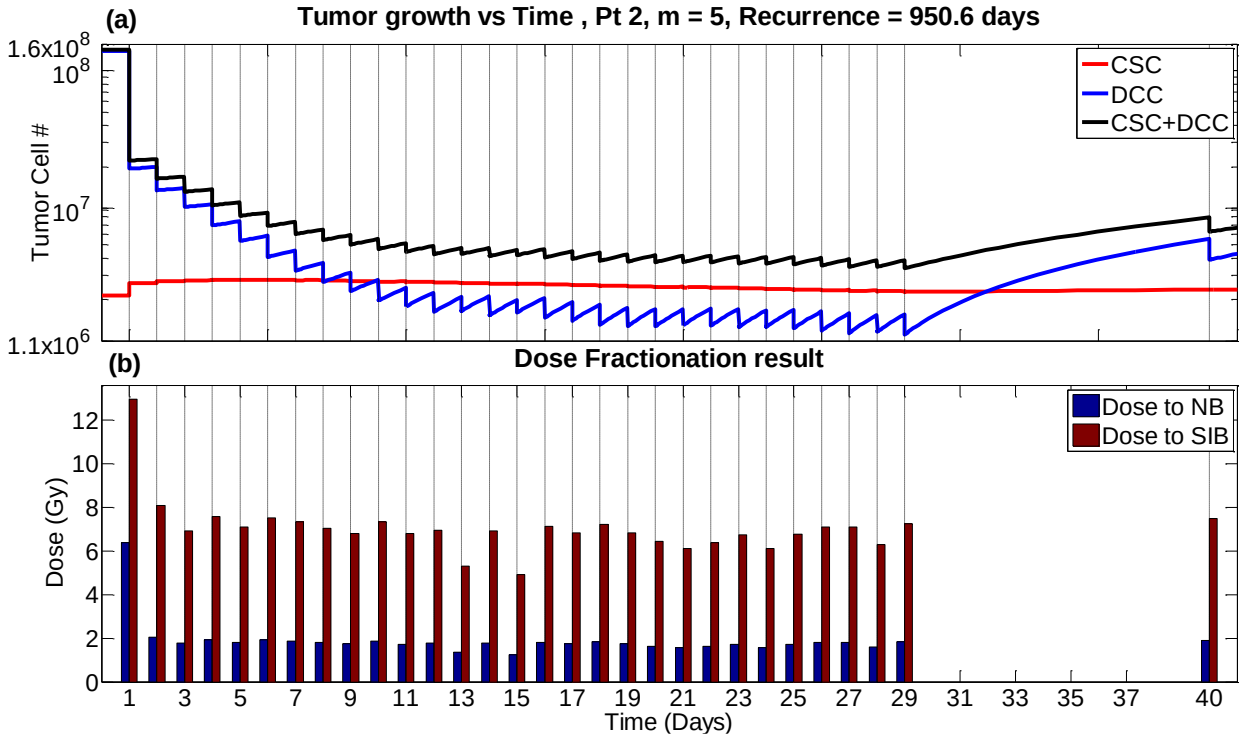

Figure 5-6: Dose fractionation result and corresponding tumor growth vs. time for patient 2 with CSC concentration multiplier m = 5. (a) The breakdown of CSC and DCC, along with the total viable tumor volume. (b) Resultant dose delivered to both the non-boost (blue) and SIB (red) regions at the corresponding time points.

Two major types of dose fractionation outcome was observed across the patient cohort and differing CSC concentrations within boost. For both representative trends, treatment begins with a very large fraction to both the boost and non-boost volumes, followed by remaining fractions with relatively similar dosages. The first type exhibits dense once per day dose fractions in the beginning of the treatment course followed by a long time interval in the end with no treatment, as shown in Figure 5-6. The second type has a long interval with no treatment after the first fraction is delivered, followed by dense once-per-

day deliveries close to the end of the treatment course, as shown in Figure 5-7. For both figures, the two subplots share the same time axes to directly demonstrate how the obtained dose fractionation scheme effects tumor progression during the treatment course, and each set of bars in subplot (b) represents the doses simultaneously delivered to the SIB (red) and non-boost (blue) volumes, and the time correspondence for each fraction to the tumor growth plot is further illustrated by the vertical dashed lines.

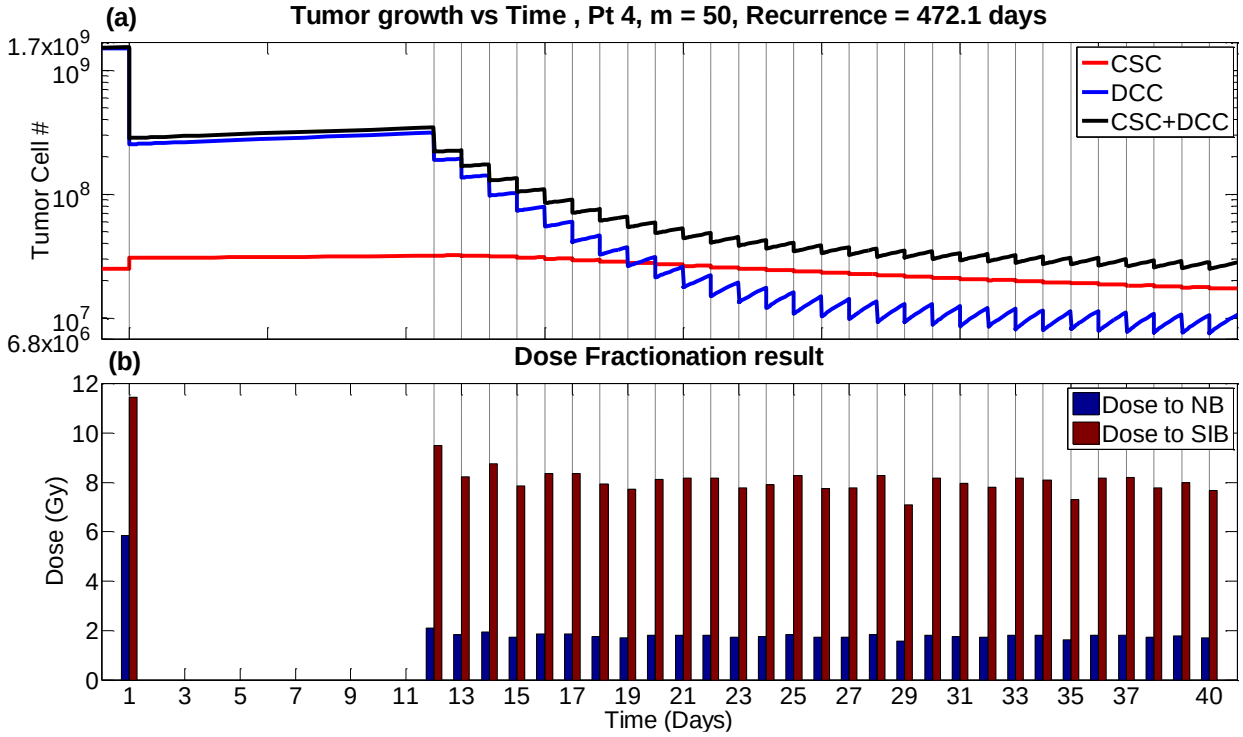

Figure 5-7: Dose fractionation result and corresponding tumor growth vs. time for patient 4 with CSC concentration multiplier m = 50. (a) The breakdown of CSC and DCC, along with the total viable tumor volume. (b) Resultant dose delivered to both the non-boost (blue) and SIB (red) regions at the corresponding time points.

For each patient, type 1 is observed for cases with lower m values and transitions into type 2 as the multiplier increases ($m \geq 10$). The m value at which the type 1 to 2 transition occurs is smaller for cases with quicker original treatment time or smaller BED_{SIB}. For all cases, the extremely radioresistant CSC increases slightly in the beginning due to radiation induced cell reprogramming, and as the DCC compartment quickly reduces in size, the CSC reduction

from radiation killing gradually overtakes the increase due to reprogramming, resulting in steady decrease in CSCs.

5.3.4 Discussion

In this work, we assess the power in improving GBM disease outcome by combining spatial and temporal dose optimization. State-of-the-art spatial dose optimization was performed with 4π radiotherapy on personalized boost volumes where the eventual disease recurrence occurred. Going beyond the current standard of attempting to treat with a manually assigned prescription dose, we explored the maximum achievable prescription dose to patient-specific boost volumes with a novel simultaneous integrated boost optimization formulation. Results from this formulation showed that substantial boost of up to 4 times the original prescription dose can be achieved to a smaller volume residing within the original PTV while still maintaining acceptable dose to the surrounding normal brain volume and critical organs at risk. Application of this discovered method is not merely limited to treatment on GBM. Case-specific maximized boost could be performed to any region with particularly higher PET or disease activity within a treatment volume, regardless of disease site. The dose maximizing concept itself is also not limited to 4π radiotherapy, but rather, could also be applied to many other existing delivery techniques.

With a unique cancer stem cell dynamics mathematical model that reflects the definitive treatment failure of GBM, a dose fractionation optimization framework was developed to examine potential solutions in further delaying disease recurrence. In conjunction with dose boost to a small volume, significant delay of up to 276 days was shown from dose fractionation optimization even without CSC concentration increase within the

simulated SIB volume. Improved recurrence delay is associated with higher boost dose, larger boost volume fraction, higher CSC concentration increase within boost volume, and cases with slower growing tumors, as expected. With CSC concentration increase of up to 100 fold, maximum recurrence delay of 392 days was observed for a patient with the slowest growing disease (patient 7). Increase in CSC concentration within boost volume has resulted in differing optimal treatment strategies where fractions were delayed to close to the end of the treatment course rather than applied in the beginning. The possible reasoning of such behaviour is explained as follows. With the conservation of cell density to both volumes during initialization, higher CSC concentration results in substantially lower DCC volume within the boost volume. Even though CSC governs the eventual fate of the tumor, the CSCs are extremely radioresistant and grow very slowly, the timing of delivering on CSC alone became less essential. Therefore, the optimal solution for delaying eventual overall recurrence is instead to wait until more DCCs are also within the high radiation field. The demonstrated potential in substantial recurrence delay across a patient cohort with differing disease characteristics is exciting.

There are several limitations with the study. Although the model was able to successfully reproduce the aggressive regrowth of GBM after aggressive treatment, it does not take into consideration biological factors such as tumor vasculature, oxygen content, the effect of asymmetric divisions, and spatial heterogeneity. While the current mathematical model is simplistic, its potential in significant disease delay warrants further investigation with rigorously designed preclinical and clinical studies. With the technological and algorithmic abilities to spatially optimize and modulate dose distributions, the long term goal would be to combine these highly complex spatial dose distributions with improved

biological models with spatial heterogeneity considerations to even more realistically predict and understand treatment response in order to further improve radiation therapy outcome in GBM patients.

5.3.5 Conclusion

By combining the spatial dose sparing power of 4π radiotherapy and temporal dose fractionation optimization with a CSC dynamics biological model in a personalized manner, significant potential in GBM disease recurrence delay was demonstrated across a cohort with differing disease characteristics. Further investigation is needed to validate the proposed model and resultant dose fractionation schedules to fully realize and translate these substantial clinical benefits.

6 APPENDIX

THE CHAMBOLLE-POCK ALGORITHM

The Chambolle-Pock algorithm is a first-order primal dual algorithm, utilized to solve the simultaneous integrated boost optimization problem in this dissertation. In this appendix, the format of the optimization problem required for this algorithm, details regarding the algorithm, and utilized line-search procedure, will be described.

6.1 Optimization problem formulation

The Chambolle-Pock algorithm solves problems in the following canonical form

$$minimize\ F(Kx) + G(x)$$

Equation 6-1

,where F and G are functions and K is a matrix. The SIB problem was written to fit this canonical form as follows in Equation 6-2.

$$K = \begin{bmatrix} A_{NB} \\ A_{OAR} \\ 1^T A_{Brn} \\ A_{PTV_{95\%}} \\ A_{Brn_M} \\ A_{SIB} \end{bmatrix}$$

$$F(z) = \frac{1}{2}\|(z_1 - d)\|_2^2 + \frac{1}{2}w_{OAR}\|(z_2)\|_2^2 + I_-(z_3 - nD_{mean}) + I_+(z_4 - d) + I_-(z_5 - d \cdot p) + \frac{1}{2}w_H \left\| (z_6 - \frac{1^T A_{SIB} x}{n_{SIB}}) \right\|_2^2$$

$$G(x) = -1^T A_{SIB} x + I_+(x)$$

Equation 6-2

6.2 The Algorithm

The problem was solved with the overrelaxed version of the Chambolle-Pock algorithm[170], as shown below in Equation 6-3:

$$\bar{x}^{n+1} = prox_{\tau G}(x^n - \tau K^T \mathrm{z}^{\mathrm{n}})$$

$$\bar{\mathrm{z}}^{n+1} = prox_{\sigma \mathrm{F}^*}(\mathrm{z}^n - \sigma \mathrm{K}(\bar{x}^{n+1} + \theta(\bar{x}^{n+1} - x^n))$$

$$x^{n+1} = \rho \bar{x}^{n+1} + (1 - \rho)x^n$$

$$z^{n+1} = \rho \bar{z}^{n+1} + (1 - \rho)z^n,$$

Equation 6-3

with z indicating the variable of the dual problem in Equation 6-4 .

$$minimize \;\; G^*(-K^T z) + F^*(z)$$

Equation 6-4

F^* indicates the convex conjugate of function F, defined as:

$$F^*(z) = \sup_y (z^T y - F(y))$$

Equation 6-5

$prox$ indicates the proximal operator, defined as

$$prox_{th}(x) = \underset{v}{\operatorname{argmin}}(h(v) + \frac{1}{2t}\|v - x\|_2^2),$$

Equation 6-6

where t serves as a step size and h indicates a lower semi-continuous function of which the prox operator tries to minimize. ρ is the overrelaxation parameter, which was set at 1.9. θ was initialized at 1.

6.3 Linesearch procedure

The linesearch algorithm implemented is shown below, adapted from Malitsky and Pock[171].

Initialization: Choose $x^0 \in X$, $y^1 \in Y$, $\tau_0 > 0$, $\mu \in (0,1), \delta \in (0,1)$, and $\beta > 0$.
Set $\theta_0 = 1$.
Main iteration:
1. Compute

$$x^k = \text{prox}_{\tau_{k-1}g}(x^{k-1} - \tau_{k-1}K^*y^k).$$

2. Choose any $\tau_k \in [\tau_{k-1}, \tau_{k-1}\sqrt{1+\theta_{k-1}}]$ and run
Linesearch:
2.a. Compute

$$\theta_k = \frac{\tau_k}{\tau_{k-1}}$$
$$\bar{x}^k = x^k + \theta_k(x^k - x^{k-1})$$
$$y^{k+1} = \text{prox}_{\beta\tau_k f^*}(y^k + \beta\tau_k K\bar{x}^k)$$

2.b. Break linesearch if

$$\sqrt{\beta}\tau_k \left\|K^*y^{k+1} - K^*y^k\right\| \leq \delta \left\|y^{k+1} - y^k\right\|$$

Otherwise, set $\tau_k := \tau_k\mu$ and go to 2.a.
End of linesearch

μ was set to 0.7, δ was initialized at 0.90.

$\beta = \sigma/\tau$, and σ and τ were tuned through exhaustive search with the fixed step size version of Chambolle-Pock, as described in the previous section.

7 REFERENCES

1. Stupp R, Hegi ME, Mason WP, et al. Effects of radiotherapy with concomitant and adjuvant temozolomide versus radiotherapy alone on survival in glioblastoma in a randomised phase III study: 5-year analysis of the EORTC-NCIC trial. *Lancet Oncol.* 2009;10(5):459-466.
2. Adamson C, Kanu OO, Mehta AI, et al. Glioblastoma multiforme: a review of where we have been and where we are going. *Expert Opin Investig Drugs.* 2009;18(8):1061-1083.
3. Dolecek TA, Propp JM, Stroup NE, Kruchko C. CBTRUS statistical report: primary brain and central nervous system tumors diagnosed in the United States in 2005–2009. *Neuro-oncology.* 2012;14(suppl 5):v1-v49.
4. Chan JL, Lee SW, Fraass BA, et al. Survival and failure patterns of high-grade gliomas after three-dimensional conformal radiotherapy. *J Clin Oncol.* 2002;20(6):1635-1642.
5. Wallner KE, Galicich JH, Krol G, Arbit E, Malkin MG. Patterns of failure following treatment for glioblastoma multiforme and anaplastic astrocytoma. *Int J Radiat Oncol Biol Phys.* 1989;16(6):1405-1409.
6. Johnson DR, O'Neill BP. Glioblastoma survival in the United States before and during the temozolomide era [published online ahead of print 2011/11/02]. *J Neurooncol.* 2012;107(2):359-364.
7. Shrieve DC, Wara WM, Edwards MS, et al. Hyperfractionated radiation therapy for gliomas of the brainstem in children and in adults. *Int J Radiat Oncol Biol Phys.* 1992;24(4):599-610.
8. Nieder C, Nestle U, Ketter R, et al. Hyperfractionated and accelerated-hyperfractionated radiotherapy for glioblastoma multiforme. *Radiat Oncol Investig.* 1999;7(1):36-41.
9. Deutsch M, Green SB, Strike TA, et al. Results of a randomized trial comparing BCNU plus radiotherapy, streptozotocin plus radiotherapy, BCNU plus hyperfractionated radiotherapy, and BCNU following misonidazole plus radiotherapy in the postoperative treatment of malignant glioma. *Int J Radiat Oncol Biol Phys.* 1989;16(6):1389-1396.
10. Ludgate CM, Douglas BG, Dixon PF, Steinbok P, Jackson SM, Goodman GB. Superfractionated radiotherapy in grade III, IV intracranial gliomas. *Int J Radiat Oncol Biol Phys.* 1988;15(5):1091-1095.
11. Payne DG, Simpson WJ, Keen C, Platts ME. Malignant astrocytoma: hyperfractionated and standard radiotherapy with chemotherapy in a randomized prospective clinical trial. *Cancer.* 1982;50(11):2301-2306.

12. Brada M, Sharpe G, Rajan B, et al. Modifying radical radiotherapy in high grade gliomas; shortening the treatment time through acceleration. *Int J Radiat Oncol Biol Phys.* 1999;43(2):287-292.

13. Horiot JC, van den Bogaert W, Ang KK, et al. European Organization for Research on Treatment of Cancer trials using radiotherapy with multiple fractions per day. A 1978-1987 survey. *Front Radiat Ther Oncol.* 1988;22:149-161.

14. Keim H, Potthoff PC, Schmidt K, Schiebusch M, Neiss A, Trott KR. Survival and quality of life after continuous accelerated radiotherapy of glioblastomas. *Radiother Oncol.* 1987;9(1):21-26.

15. Floyd NS, Woo SY, Teh BS, et al. Hypofractionated intensity-modulated radiotherapy for primary glioblastoma multiforme. *Int J Radiat Oncol Biol Phys.* 2004;58(3):721-726.

16. Bauman GS, Gaspar LE, Fisher BJ, Halperin EC, Macdonald DR, Cairncross JG. A prospective study of short-course radiotherapy in poor prognosis glioblastoma multiforme. *Int J Radiat Oncol Biol Phys.* 1994;29(4):835-839.

17. Ford JM, Stenning SP, Boote DJ, et al. A short fractionation radiotherapy treatment for poor prognosis patients with high grade glioma. *Clin Oncol (R Coll Radiol).* 1997;9(1):20-24.

18. Gliński B. Postoperative hypofractionated radiotherapy versus conventionally fractionated radiotherapy in malignant gliomas. A preliminary report on a randomized trial. *J Neurooncol.* 1993;16(2):167-172.

19. Gutin PH, Prados MD, Phillips TL, et al. External irradiation followed by an interstitial high activity iodine-125 implant "boost" in the initial treatment of malignant gliomas: NCOG study 6G-82-2. *Int J Radiat Oncol Biol Phys.* 1991;21(3):601-606.

20. Laperriere N, Zuraw L, Cairncross G, Group CCOPGIN-ODS. Radiotherapy for newly diagnosed malignant glioma in adults: a systematic review. *Radiother Oncol.* 2002;64(3):259-273.

21. Nieder C, Astner ST, Mehta MP, Grosu AL, Molls M. Improvement, clinical course, and quality of life after palliative radiotherapy for recurrent glioblastoma. *Am J Clin Oncol.* 2008;31(3):300-305.

22. Combs SE, Widmer V, Thilmann C, Hof H, Debus J, Schulz-Ertner D. Stereotactic radiosurgery (SRS): treatment option for recurrent glioblastoma multiforme (GBM). *Cancer.* 2005;104(10):2168-2173.

23. Amichetti M, Amelio D. A Review of the Role of Re-Irradiation in Recurrent High-Grade Glioma (HGG) [published online ahead of print 2011/10/28]. *Cancers (Basel).* 2011;3(4):4061-4089.

24. Wein LM, Cohen JE, Wu JT. Dynamic optimization of a linear-quadratic model with incomplete repair and volume-dependent sensitivity and repopulation. *Int J Radiat Oncol Biol Phys.* 2000;47(4):1073-1083.

25. Lindblom E, Dasu A, Toma-Dasu I. Optimal fractionation in radiotherapy for non-small cell lung cancer--a modelling approach. *Acta Oncol.* 2015;54(9):1592-1598.

26. Bortfeld T, Ramakrishnan J, Tsitsiklis JN, Unkelbach J. Optimization of radiation therapy fractionation schedules in the presence of tumor repopulation. *INFORMS Journal on Computing.* 2015;27(4):788-803.

27. Kim M, Stewart RD, Phillips MH. A feasibility study: Selection of a personalized radiotherapy fractionation schedule using spatiotemporal optimization. *Medical physics.* 2015;42(11):6671-6678.

28. Taghian A, Budach W, Baumann M, Freeman J, Suit H. In vivo radiation sensitivity of glioblastoma multiforme. *International Journal of Radiation Oncology* Biology* Physics.* 1995;32(1):99-104.

29. Taghian A. In vitro and in vivo radiation sensitivity of glioblastoma multiforme: correction. *International Journal of Radiation Oncology Biology Physics.* 1998;42:464-465.

30. Reya T, Morrison SJ, Clarke MF, Weissman IL. Stem cells, cancer, and cancer stem cells. *Nature.* 2001;414(6859):105-111.

31. Clarke MF, Dick JE, Dirks PB, et al. Cancer stem cells--perspectives on current status and future directions: AACR Workshop on cancer stem cells. *Cancer Res.* 2006;66(19):9339-9344.

32. Bao S, Wu Q, McLendon RE, et al. Glioma stem cells promote radioresistance by preferential activation of the DNA damage response. *Nature.* 2006;444(7120):756-760.

33. Phillips TM, McBride WH, Pajonk F. The response of CD24(-/low)/CD44+ breast cancer-initiating cells to radiation. *J Natl Cancer Inst.* 2006;98(24):1777-1785.

34. Woodward WA, Chen MS, Behbod F, Alfaro MP, Buchholz TA, Rosen JM. WNT/beta-catenin mediates radiation resistance of mouse mammary progenitor cells. *Proc Natl Acad Sci U S A.* 2007;104(2):618-623.

35. Ogawa K, Yoshioka Y, Isohashi F, Seo Y, Yoshida K, Yamazaki H. Radiotherapy targeting cancer stem cells: current views and future perspectives. *Anticancer research.* 2013;33(3):747-754.

36. Kumazawa S, Kajiyama H, Umezu T, et al. Possible association between stem-like hallmark and radioresistance in human cervical carcinoma cells. *Journal of Obstetrics and Gynaecology Research.* 2014;40(5):1389-1398.

37. Desai A, Webb B, Gerson SL. CD133+ cells contribute to radioresistance via altered regulation of DNA repair genes in human lung cancer cells. *Radiotherapy and Oncology.* 2014;110(3):538-545.

38. Xia P, Gou W-f, Wang J-j, et al. Distinct radiosensitivity of lung carcinoma stem-like side population and main population cells. *Cancer Biotherapy and Radiopharmaceuticals.* 2013;28(6):471-478.

39. Youssefpour H, Li X, Lander AD, Lowengrub JS. Multispecies model of cell lineages and feedback control in solid tumors. *J Theor Biol.* 2012;304:39-59.

40. Bachman JW, Hillen T. Mathematical optimization of the combination of radiation and differentiation therapies for cancer. *Front Oncol.* 2013;3:52.

41. Yan H, Romero-Lopez M, Frieboes H, Hughes C, Lowengrub J. Multiscale Modeling of Glioblastoma Suggests that the Partial Disruption of Vessel/Cancer Stem Cell Crosstalk Can Promote Tumor Regression without Increasing Invasiveness. *IEEE Transactions on Biomedical Engineering.* 2016.

42. Leder K, Pitter K, Laplant Q, et al. Mathematical modeling of PDGF-driven glioblastoma reveals optimized radiation dosing schedules [published online ahead of print 2014/02/04]. *Cell.* 2014;156(3):603-616.

43. Yu VY, Nguyen D, Pajonk F, et al. Incorporating cancer stem cells in radiation therapy treatment response modeling and the implication in glioblastoma multiforme treatment resistance. *Int J Radiat Oncol Biol Phys.* 2015;91(4):866-875.

44. Dong P, Lee P, Ruan D, et al. 4pi Non-Coplanar Liver SBRT: A Novel Delivery Technique [published online ahead of print 2012/11/17]. *Int J Radiat Oncol Biol Phys.* 2013;85(5):1360-1366.

45. Romeijn HE, Ahuja RK, Dempsey JF, Kumar A. A column generation approach to radiation therapy treatment planning using aperture modulation. *SIAM Journal on Optimization.* 2005;15(3):838-862.

46. Nguyen D, Rwigema J-CM, Victoria YY, et al. Feasibility of extreme dose escalation for glioblastoma multiforme using 4π radiotherapy. *Radiation Oncology.* 2014;9(1):239.

47. Rwigema J-CM, Nguyen D, Heron DE, et al. 4π Noncoplanar Stereotactic Body Radiation Therapy for Head-and-Neck Cancer: Potential to Improve Tumor Control and Late Toxicity. *International Journal of Radiation Oncology* Biology* Physics.* 2015;91(2):401-409.

48. Woods K, Nguyen D, Tran A, et al. Viability of Non-Coplanar VMAT for Liver SBRT as Compared to Coplanar VMAT and Beam Orientation Optimized 4π IMRT. *Adv Radiat Oncol.* 2016;1(1):67-75.

49. Dong P, Lee P, Ruan D, et al. 4π noncoplanar stereotactic body radiation therapy for centrally located or larger lung tumors. *International Journal of Radiation Oncology* Biology* Physics.* 2013;86(3):407-413.

50. Dong P, Nguyen D, Ruan D, et al. Feasibility of prostate robotic radiation therapy on conventional C-arm linacs. *Pract Radiat Oncol.* 2014;4(4):254-260.

51. Kumar V, Gu Y, Basu S, et al. Radiomics: the process and the challenges. *Magn Reson Imaging.* 2012;30(9):1234-1248.

52. Lambin P, Rios-Velazquez E, Leijenaar R, et al. Radiomics: extracting more information from medical images using advanced feature analysis. *European journal of cancer.* 2012;48(4):441-446.

53. Gillies RJ, Kinahan PE, Hricak H. Radiomics: images are more than pictures, they are data. *Radiology.* 2015;278(2):563-577.

54. Parmar C, Grossmann P, Bussink J, Lambin P, Aerts HJ. Machine learning methods for quantitative radiomic biomarkers. *Scientific reports.* 2015;5.

55. Aerts HJ, Velazquez ER, Leijenaar RT, et al. Decoding tumour phenotype by noninvasive imaging using a quantitative radiomics approach. *Nature communications.* 2014;5.

56. Alic L, Niessen WJ, Veenland JF. Quantification of heterogeneity as a biomarker in tumor imaging: a systematic review. *PloS one.* 2014;9(10):e110300.

57. Kickingereder P, Götz M, Muschelli J, et al. Large-scale radiomic profiling of recurrent glioblastoma identifies an imaging predictor for stratifying anti-angiogenic treatment response. *Clinical Cancer Research.* 2016.

58. Pope WB, Kim HJ, Huo J, et al. Recurrent Glioblastoma Multiforme: ADC Histogram Analysis Predicts Response to Bevacizumab Treatment 1. *Radiology.* 2009;252(1):182-189.

59. Hu LS, Ning S, Eschbacher JM, et al. Multi-parametric MRI and texture analysis to visualize spatial histologic heterogeneity and tumor extent in glioblastoma. *PloS one.* 2015;10(11):e0141506.

60. Jain R, Poisson LM, Gutman D, et al. Outcome prediction in patients with glioblastoma by using imaging, clinical, and genomic biomarkers: focus on the nonenhancing component of the tumor. *Radiology.* 2014;272(2):484-493.

61. Prasanna P, Tiwari P, Madabhushi A. Co-occurrence of Local Anisotropic Gradient Orientations (CoLlAGe): distinguishing tumor confounders and molecular subtypes on MRI. Paper presented at: International Conference on Medical Image Computing and Computer-Assisted Intervention2014.

62. Yu VY, Tran A, Nguyen D, et al. The development and verification of a highly accurate collision prediction model for automated noncoplanar plan delivery. *Med Phys.* 2015;42(11):6457.

63. Pajonk F, Vlashi E, McBride WH. Radiation resistance of cancer stem cells: the 4 R's of radiobiology revisited. *Stem Cells.* 2010;28(4):639-648.

64. Ogawa K, Yoshioka Y, Isohashi F, Seo Y, Yoshida K, Yamazaki H. Radiotherapy targeting cancer stem cells: current views and future perspectives [published online ahead of print 2013/03/14]. *Anticancer Res.* 2013;33(3):747-754.

65. Kumazawa S, Kajiyama H, Umezu T, et al. Possible association between stem-like hallmark and radioresistance in human cervical carcinoma cells [published online ahead of print 2014/04/23]. *J Obstet Gynaecol Res.* 2014;40(5):1389-1398.

66. Desai A, Webb B, Gerson SL. CD133+ cells contribute to radioresistance via altered regulation of DNA repair genes in human lung cancer cells [published online ahead of print 2014/01/21]. *Radiother Oncol.* 2014;110(3):538-545.

67. Kim SY, Rhee JG, Song X, Prochownik EV, Spitz DR, Lee YJ. Breast Cancer Stem Cell-Like Cells Are More Sensitive to Ionizing Radiation than Non-Stem Cells: Role of ATM. *PLoS One.* 2012;7(11).

68. Xia P, Gou WF, Wang JJ, et al. Distinct radiosensitivity of lung carcinoma stem-like side population and main population cells [published online ahead of print 2013/03/22]. *Cancer Biother Radiopharm.* 2013;28(6):471-478.

69. Hillen T, Enderling H, Hahnfeldt P. The tumor growth paradox and immune system-mediated selection for cancer stem cells. *Bull Math Biol.* 2013;75(1):161-184.

70. Enderling H, Anderson AR, Chaplain MA, Beheshti A, Hlatky L, Hahnfeldt P. Paradoxical dependencies of tumor dormancy and progression on basic cell kinetics. *Cancer Res.* 2009;69(22):8814-8821.

71. Lagadec C, Vlashi E, Della Donna L, et al. Survival and self-renewing capacity of breast cancer initiating cells during fractionated radiation treatment [published online ahead of print 2010/02/18]. *Breast Cancer Res.* 2010;12(1):R13.

72. Vlashi E, Kim K, Lagadec C, et al. In vivo imaging, tracking, and targeting of cancer stem cells [published online ahead of print 2009/02/27]. *J Natl Cancer Inst.* 2009;101(5):350-359.

73. Gao X, McDonald JT, Hlatky L, Enderling H. Acute and fractionated irradiation differentially modulate glioma stem cell division kinetics [published online ahead of print 2012/12/28]. *Cancer Res.* 2013;73(5):1481-1490.

74. Park C, Papiez L, Zhang S, Story M, Timmerman RD. Universal survival curve and single fraction equivalent dose: useful tools in understanding potency of ablative radiotherapy [published online ahead of print 2008/02/12]. *Int J Radiat Oncol Biol Phys.* 2008;70(3):847-852.

75. Weichselbaum RR, Epstein J, Little JB, Kornblith PL. In vitro cellular radiosensitivity of human malignant tumors. *Eur J Cancer.* 1976;12(1):47-51.

76. Astrahan M. Some implications of linear-quadratic-linear radiation dose-response with regard to hypofractionation. *Med Phys.* 2008;35(9):4161-4172.

77. Guerrero M, Li XA. Extending the linear-quadratic model for large fraction doses pertinent to stereotactic radiotherapy. *Phys Med Biol.* 2004;49(20):4825-4835.

78. Kavanagh BD, Newman F. Toward a unified survival curve: in regard to Park et al. (IntJ Radiat Oncol Biol Phys 2008;70:847-852) and Krueger et al. (Int J Radiat Oncol Biol Phys 2007;69:1262-1271). *Int J Radiat Oncol Biol Phys.* 2008;71(3):958-959.

79. McKenna F, Ahmad S. Toward a unified survival curve: in regard to Kavanagh and Newman (Int J Radiat Oncol Biol Phys 2008;71:958-959) and Park et al. (IntJ Radiat Oncol Biol Phys 2008;70:847-852). *Int J Radiat Oncol Biol Phys.* 2009;73(2):640; author reply 640-641.

80. Fowler JF. Linear quadratics is alive and well: in regard to Park et al. (Int J Radiat Oncol Biol Phys 2008;70:847-852). *Int J Radiat Oncol Biol Phys.* 2008;72(3):957; author reply 958.

81. Brown JM, Carlson DJ, Brenner DJ. The tumor radiobiology of SRS and SBRT: are more than the 5 Rs involved? [published online ahead of print 2014/01/15]. *Int J Radiat Oncol Biol Phys.* 2014;88(2):254-262.

82. Visvader JE, Lindeman GJ. Cancer stem cells in solid tumours: accumulating evidence and unresolved questions. *Nat Rev Cancer.* 2008;8(10):755-768.

83. Enderling H, Hlatky L, Hahnfeldt P. Cancer Stem Cells: A Minor Cancer Subpopulation that Redefines Global Cancer Features. *Front Oncol.* 2013;3:76.

84. Garcia LM, Wilkins DE, Raaphorst GP. Alpha/beta ratio: A dose range dependence study. *Int J Radiat Oncol Biol Phys.* 2007;67(2):587-593.

85. PUCK TT, MARCUS PI. Action of x-rays on mammalian cells. *J Exp Med.* 1956;103(5):653-666.

86. Lagadec C, Dekmezian C, Bauche L, Pajonk F. Oxygen levels do not determine radiation survival of breast cancer stem cells [published online ahead of print 2012/04/06]. *PLoS One.* 2012;7(3):e34545.

87. Barranco SC, Romsdahl MM, Humphrey RM. The radiation response of human malignant melanoma cells grown in vitro. *Cancer Res.* 1971;31(6):830-833.

88. MacArthur BD, Lemischka IR. Statistical mechanics of pluripotency [published online ahead of print 2013/08/06]. *Cell.* 2013;154(3):484-489.

89. Haustermans KM, Hofland I, Van Poppel H, et al. Cell kinetic measurements in prostate cancer. *Int J Radiat Oncol Biol Phys.* 1997;37(5):1067-1070.

90. Shimomatsuya T, Tanigawa N, Muraoka R. Proliferative activity of human tumors: assessment using bromodeoxyuridine and flow cytometry. *Jpn J Cancer Res.* 1991;82(3):357-362.

91. Trott KR. Experimental results and clinical implications of the four R's in fractionated radiotherapy. *Radiat Environ Biophys.* 1982;20(3):159-170.

92. Rew DA, Campbell ID, Taylor I, Wilson GD. Proliferation indices of invasive breast carcinomas after in vivo 5-bromo-2'-deoxyuridine labelling: a flow cytometric study of 75 tumours. *Br J Surg.* 1992;79(4):335-339.

93. Sasaki T, Sato Y, Sakka M. Cell population kinetics of human solid tumors: a statistical analysis in various histological types. *Gann.* 1980;71(4):520-529.

94. Crnalic S, Panagopoulos I, Boquist L, Mandahl N, Stenling R, Löfvenberg R. Establishment and characterisation of a human clear cell sarcoma model in nude mice. *Int J Cancer.* 2002;101(6):505-511.

95. Struikmans H, Rutgers DH, Jansen GH, Tulleken CA, van der Tweel I, Battermann JJ. S-phase fraction, 5-bromo-2'-deoxy-uridine labelling index, duration of S-phase, potential doubling time, and DNA index in benign and malignant brain tumors. *Radiat Oncol Investig.* 1997;5(4):170-179.

96. Timmerman R, Paulus R, Galvin J, et al. Stereotactic body radiation therapy for inoperable early stage lung cancer [published online ahead of print 2010/03/18]. *JAMA.* 2010;303(11):1070-1076.

97. Lee SW, Fraass BA, Marsh LH, et al. Patterns of failure following high-dose 3-D conformal radiotherapy for high-grade astrocytomas: a quantitative dosimetric study [published online ahead of print 1999/02/16]. *Int J Radiat Oncol Biol Phys.* 1999;43(1):79-88.

98. Pedicini P, Strigari L, Benassi M. Estimation of a self-consistent set of radiobiological parameters from hypofractionated versus standard radiation therapy of prostate cancer [published online ahead of print 2013/01/22]. *Int J Radiat Oncol Biol Phys.* 2013;85(5):e231-237.

99. Fowler JF. 21 years of biologically effective dose [published online ahead of print 2010/07/07]. *Br J Radiol.* 2010;83(991):554-568.

100. Gutin PH, Prados MD, Phillips TL, et al. External irradiation followed by an interstitial high activity iodine-125 implant "boost" in the initial treatment of malignant gliomas: NCOG study 6G-82-2 [published online ahead of print 1991/08/01]. *Int J Radiat Oncol Biol Phys.* 1991;21(3):601-606.

101. Mukherjee B, McEllin B, Camacho CV, et al. EGFRvIII and DNA double-strand break repair: a molecular mechanism for radioresistance in glioblastoma [published online ahead of print 2009/05/14]. *Cancer Res.* 2009;69(10):4252-4259.

102. Jamal M, Rath BH, Williams ES, Camphausen K, Tofilon PJ. Microenvironmental regulation of glioblastoma radioresponse [published online ahead of print 2010/11/03]. *Clin Cancer Res.* 2010;16(24):6049-6059.

103. Lagadec C, Vlashi E, Della Donna L, Dekmezian C, Pajonk F. Radiation-induced reprogramming of breast cancer cells. *Stem Cells.* 2012;30(5):833-844.

104. Lee I, Sandler H. Hormone therapy and radiotherapy for intermediate risk prostate cancer. *Semin Radiat Oncol.* 2008;18(1):7-14.

105. Taghian A. In vitro and in vivo radiation sensitivity of glioblastoma multiforme: correction [published online ahead of print 1998/10/27]. *Int J Radiat Oncol Biol Phys.* 1998;42(2):464.

106. Taghian A, Suit H, Baumann M. In vitro and in vivo radiation sensitivity of glioblastoma multiforme: correction [published online ahead of print 1996/07/15]. *Int J Radiat Oncol Biol Phys.* 1996;35(5):1124-1125.

107. Taghian A, DuBois W, Budach W, Baumann M, Freeman J, Suit H. In vivo radiation sensitivity of glioblastoma multiforme [published online ahead of print 1995/04/30]. *Int J Radiat Oncol Biol Phys.* 1995;32(1):99-104.

108. Marko NF, Weil RJ, Schroeder JL, Lang FF, Suki D, Sawaya RE. Extent of resection of glioblastoma revisited: personalized survival modeling facilitates more accurate survival prediction and supports a maximum-safe-resection approach to surgery. *J Clin Oncol.* 2014;32(8):774-782.

109. De Bonis P, Anile C, Pompucci A, et al. The influence of surgery on recurrence pattern of glioblastoma. *Clin Neurol Neurosurg.* 2013;115(1):37-43.

110. Bleau AM, Hambardzumyan D, Ozawa T, et al. PTEN/PI3K/Akt pathway regulates the side population phenotype and ABCG2 activity in glioma tumor stem-like cells. *Cell Stem Cell.* 2009;4(3):226-235.

111. Kirkpatrick S, Gelatt CD, Vecchi MP. Optimization by simmulated annealing. *science.* 1983;220(4598):671-680.

112. Nieder C, Grosu AL, Molls M. A comparison of treatment results for recurrent malignant gliomas. *Cancer Treat Rev.* 2000;26(6):397-409.

113. Yang Y, Xing L. Optimization of radiotherapy dose-time fractionation with consideration of tumor specific biology. *Med Phys.* 2005;32(12):3666-3677.

114. Stupp R, Hegi ME, Mason WP, et al. Effects of radiotherapy with concomitant and adjuvant temozolomide versus radiotherapy alone on survival in glioblastoma in a randomised phase III study: 5-year analysis of the EORTC-NCIC trial [published online ahead of print 2009/03/10]. *Lancet Oncol.* 2009;10(5):459-466.

115. Breedveld S, Storchi PR, Voet PW, Heijmen BJ. iCycle: Integrated, multicriterial beam angle, and profile optimization for generation of coplanar and noncoplanar IMRT plans. *Med Phys.* 2012;39(2):951-963.

116. Fahimian B, Yu V, Horst K, Xing L, Hristov D. Trajectory modulated prone breast irradiation: a LINAC-based technique combining intensity modulated delivery and motion of the couch [published online ahead of print 2013/11/16]. *Radiother Oncol.* 2013;109(3):475-481.

117. Yang Y, Zhang P, Happersett L, et al. Choreographing couch and collimator in volumetric modulated arc therapy [published online ahead of print 2011/03/08]. *Int J Radiat Oncol Biol Phys.* 2011;80(4):1238-1247.

118. Ma Y, Popple R, Suh T-S, Xing L. Beam's-Eye-View Dosimetrics–Guided Inverse Planning for Aperture-Modulated Arc Therapy. *International Journal of Radiation Oncology* Biology* Physics.* 2009;75(5):1587-1595.

119. MacDonald RL, Thomas CG. Dynamic trajectory-based couch motion for improvement of radiation therapy trajectories in cranial SRT. *Med Phys.* 2015;42(5):2317-2325.

120. Smyth G, Bamber JC, Evans PM, Bedford JL. Trajectory optimization for dynamic couch rotation during volumetric modulated arc radiotherapy. *Phys Med Biol.* 2013;58(22):8163-8177.

121. Tran A, Zhang J, Woods K, et al. Treatment planning comparison of IMPT, VMAT and 4π radiotherapy for prostate cases [published online ahead of print 2017/01/11]. *Radiat Oncol.* 2017;12(1):10.

122. Low DA, Harms WB, Mutic S, Purdy JA. A technique for the quantitative evaluation of dose distributions. *Med Phys.* 1998;25(5):656-661.

123. Burghelea M, Verellen D, Poels K, et al. Initial characterization, dosimetric benchmark and performance validation of Dynamic Wave Arc [published online ahead of print 2016/04/29]. *Radiat Oncol.* 2016;11:63.

124. Liang J, Atwood T, von Eyben R, et al. Trajectory Modulated Arc Therapy: A Fully Dynamic Delivery With Synchronized Couch and Gantry Motion Significantly Improves Dosimetric Indices Correlated With Poor Cosmesis in Accelerated Partial Breast Irradiation. *Int J Radiat Oncol Biol Phys.* 2015;92(5):1148-1156.

125. Wild E, Bangert M, Nill S, Oelfke U. Noncoplanar VMAT for nasopharyngeal tumors: Plan quality versus treatment time [published online ahead of print 2015/05/17]. *Med Phys.* 2015;42(5):2157.

126. Rossi L, Breedveld S, Heijmen BJ, Voet PW, Lanconelli N, Aluwini S. On the beam direction search space in computerized non-coplanar beam angle optimization for IMRT-prostate SBRT. *Phys Med Biol.* 2012;57(17):5441-5458.

127. Humm JL. Collision avoidance in computer optimized treatment planning [published online ahead of print 1994/07/01]. *Med Phys.* 1994;21(7):1053-1064.

128. Humm JL, Pizzuto D, Fleischman E, Mohan R. Collision detection and avoidance during treatment planning [published online ahead of print 1995/12/01]. *Int J Radiat Oncol Biol Phys.* 1995;33(5):1101-1108.

129. Tsiakalos MF, Scherebmann E, Theodorou K, Kappas C. Graphical treatment simulation and automated collision detection for conformal and stereotactic radiotherapy treatment planning [published online ahead of print 2001/08/08]. *Med Phys.* 2001;28(7):1359-1363.

130. Chao MM, Chao LS, Chen YJ, et al. Image display for collision avoidance of radiation therapy: treatment planning [published online ahead of print 2002/03/16]. *J Digit Imaging.* 2001;14(4):186-191.

131. Becker SJ. Collision indicator charts for gantry-couch position combinations for Varian linacs [published online ahead of print 2011/08/17]. *J Appl Clin Med Phys.* 2011;12(3):3405.

132. Nioutsikou E, Bedford JL, Webb S. Patient-specific planning for prevention of mechanical collisions during radiotherapy. *Phys Med Biol.* 2003;48(22):N313-321.

133. Hua C, Chang J, Yenice K, Chan M, Amols H. A practical approach to prevent gantry-couch collision for linac-based radiosurgery [published online ahead of print 2004/08/13]. *Med Phys.* 2004;31(7):2128-2134.

134. Hamza-Lup F, Sopin I, Zeidan O. Online external beam radiation treatment simulator. *International Journal of Computer Assisted Radiology and Surgery.* 2008;3(3-4):275-281.

135. Cannon DM, Mehta MP, Adkison JB, et al. Dose-limiting toxicity after hypofractionated dose-escalated radiotherapy in non-small-cell lung cancer. *J Clin Oncol.* 2013;31(34):4343-4348.

136. Duprez F, Berwouts D, Madani I, et al. High-dose reirradiation with intensity-modulated radiotherapy for recurrent head-and-neck cancer: Disease control, survival and toxicity [published online ahead of print 2014/07/08]. *Radiother Oncol.* 2014;111(3):388-392.

137. Popescu CC, Beckham WA, Patenaude VV, Olivotto IA, Vlachaki MT. Simultaneous couch and gantry dynamic arc rotation (CG-Darc) in the treatment of breast cancer with accelerated partial breast irradiation (APBI): a feasibility study [published online ahead of print 2013/01/16]. *J Appl Clin Med Phys.* 2013;14(1):4035.

138. Yu VY, Fahimian BP, Xing L, Hristov DH. Quality control procedures for dynamic treatment delivery techniques involving couch motion. *Med Phys.* 2014;41(8):081712.

139. Siegel RL, Miller KD, Jemal A. Cancer statistics, 2016. *CA: a cancer journal for clinicians.* 2016;66(1):7-30.

140. Klimo P, Schmidt MH. Surgical management of spinal metastases. *The Oncologist.* 2004;9(2):188-196.

141. Holman PJ, Suki D, McCutcheon I, Wolinsky JP, Rhines LD, Gokaslan ZL. Surgical management of metastatic disease of the lumbar spine: experience with 139 patients. *J Neurosurg Spine.* 2005;2(5):550-563.

142. Bartels RH, van der Linden YM, van der Graaf WT. Spinal extradural metastasis: review of current treatment options [published online ahead of print 2008/03/19]. *CA Cancer J Clin.* 2008;58(4):245-259.

143. Lee YK, Bedford JL, McNair HA, Hawkins MA. Comparison of deliverable IMRT and VMAT for spine metastases using a simultaneous integrated boost. *Br J Radiol.* 2013;86(1022):20120466.

144. Witham TF, Khavkin YA, Gallia GL, Wolinsky JP, Gokaslan ZL. Surgery insight: current management of epidural spinal cord compression from metastatic spine disease. *Nat Clin Pract Neurol.* 2006;2(2):87-94; quiz 116.

145. Manabe J, Kawaguchi N, Matsumoto S, Tanizawa T. Surgical treatment of bone metastasis: indications and outcomes. *Int J Clin Oncol.* 2005;10(2):103-111.

146. Loblaw DA, Perry J, Chambers A, Laperriere NJ. Systematic review of the diagnosis and management of malignant extradural spinal cord compression: the Cancer Care Ontario Practice Guidelines Initiative's Neuro-Oncology Disease Site Group. *J Clin Oncol.* 2005;23(9):2028-2037.

147. van der Linden YM, Lok JJ, Steenland E, et al. Single fraction radiotherapy is efficacious: a further analysis of the Dutch Bone Metastasis Study controlling for the influence of retreatment. *Int J Radiat Oncol Biol Phys.* 2004;59(2):528-537.

148. Sahgal A, Larson DA, Chang EL. Stereotactic body radiosurgery for spinal metastases: a critical review. *Int J Radiat Oncol Biol Phys.* 2008;71(3):652-665.

149. Yamada Y, Lovelock DM, Yenice KM, et al. Multifractionated image-guided and stereotactic intensity-modulated radiotherapy of paraspinal tumors: a preliminary report. *Int J Radiat Oncol Biol Phys.* 2005;62(1):53-61.

150. Yamada Y, Bilsky MH, Lovelock DM, et al. High-dose, single-fraction image-guided intensity-modulated radiotherapy for metastatic spinal lesions. *Int J Radiat Oncol Biol Phys.* 2008;71(2):484-490.

151. Gibbs IC, Kamnerdsupaphon P, Ryu MR, et al. Image-guided robotic radiosurgery for spinal metastases [published online ahead of print 2007/01/24]. *Radiother Oncol.* 2007;82(2):185-190.

152. Ryu S, Jin JY, Jin R, et al. Partial volume tolerance of the spinal cord and complications of single-dose radiosurgery. *Cancer.* 2007;109(3):628-636.

153. Sahgal A, Ma L, Gibbs I, et al. Spinal cord tolerance for stereotactic body radiotherapy [published online ahead of print 2009/09/16]. *Int J Radiat Oncol Biol Phys.* 2010;77(2):548-553.

154. Nieder C, Grosu AL, Andratschke NH, Molls M. Proposal of human spinal cord reirradiation dose based on collection of data from 40 patients. *Int J Radiat Oncol Biol Phys.* 2005;61(3):851-855.

155. Rhu S, Gerszten P, Yin F. Phase II/III study of image-guided radiosurgery/SBRT for localized spine metastasis. Radiation Therapy Oncology Group 0631. In.

156. Nelson JW, Yoo DS, Sampson JH, et al. Stereotactic body radiotherapy for lesions of the spine and paraspinal regions [published online ahead of print 2008/11/10]. *Int J Radiat Oncol Biol Phys.* 2009;73(5):1369-1375.

157. Kaprealian T, Tran A, Yu V, et al. First Prospective Trial in Linear Accelerator-Based 4π Radiation Therapy: Initial Results in Patients With Recurrent Glioblastoma. *International journal of radiation oncology, biology, physics.* 2016;96(2S):E89.

158. Agarawal JP, Swangsilpa T, van der Linden Y, Rades D, Jeremic B, Hoskin PJ. The role of external beam radiotherapy in the management of bone metastases. *Clin Oncol (R Coll Radiol).* 2006;18(10):747-760.

159. Klein S, Staring M, Murphy K, Viergever MA, Pluim JP. elastix: a toolbox for intensity-based medical image registration. *IEEE Trans Med Imaging.* 2010;29(1):196-205.

160. Sun X, Shi L, Luo Y, et al. Histogram-based normalization technique on human brain magnetic resonance images from different acquisitions. *Biomedical engineering online.* 2015;14(1):73.

161. Madabhushi A, Udupa JK. New methods of MR image intensity standardization via generalized scale. *Med Phys.* 2006;33(9):3426-3434.

162. Haralick RM, Shanmugam K, Dinstein IH. Textural Features for Image Classification. *Systems, Man and Cybernetics, IEEE Transactions on.* 1973;SMC-3(6):610-621.

163. Assefa D, Keller H, Ménard C, Laperriere N, Ferrari RJ, Yeung I. Robust texture features for response monitoring of glioblastoma multiforme on T1-weighted and T2-FLAIR MR images: a preliminary investigation in terms of identification and segmentation. *Med Phys.* 2010;37(4):1722-1736.

164. Vallières M, Freeman CR, Skamene SR, El Naqa I. A radiomics model from joint FDG-PET and MRI texture features for the prediction of lung metastases in soft-tissue sarcomas of the extremities [published online ahead of print 2015/06/29]. *Phys Med Biol.* 2015;60(14):5471-5496.

165. Peng H, Long F, Ding C. Feature selection based on mutual information criteria of max-dependency, max-relevance, and min-redundancy. *IEEE Transactions on pattern analysis and machine intelligence.* 2005;27(8):1226-1238.

166. Roffo G, Melzi S, Cristani M. Infinite feature selection. Paper presented at: Proceedings of the IEEE International Conference on Computer Vision2015.

167. Boser BE, Guyon IM, Vapnik VN. A training algorithm for optimal margin classifiers. Paper presented at: Proceedings of the fifth annual workshop on Computational learning theory1992.

168. Chang C-C, Lin C-J. LIBSVM: a library for support vector machines. *ACM Transactions on Intelligent Systems and Technology (TIST).* 2011;2(3):27.

169. Chambolle A, Pock T. A first-order primal-dual algorithm for convex problems with applications to imaging. *Journal of Mathematical Imaging and Vision.* 2011;40(1):120-145.

170. Condat L. A Primal–Dual Splitting Method for Convex Optimization Involving Lipschitzian, Proximable and Linear Composite Terms. *Journal of Optimization Theory and Applications.* 2013;158(2):460-479.

171. Malitsky Y, Pock T. A first-order primal-dual algorithm with linesearch. *arXiv preprint arXiv:160808883.* 2016.